CALIFORNIA INSTITUTE OF TECHNOLOGY

EARTHQUAKE ENGINEERING RESEARCH LABORATORY

ACTIVE INTERACTION CONTROL FOR CIVIL STRUCTURES

BY

LUO-JIA WANG

REPORT NO. EERL 97-04

A REPORT ON RESEARCH SUPPORTED BY KAJIMA CORPORATION AND THE NATIONAL SCIENCE FOUNDATION

PASADENA, CALIFORNIA

1997

THIS INVESTIGATION WAS SPONSORED IN PART BY A GRANT FROM KAJIMA CORPORATION. DR. WANG RECEIVED FINANCIAL SUPPORT FROM THE NATIONAL SCIENCE FOUNDATION (GRANTS BCS-9223680 AND CMS-9509877 UNDER THE DIRECTION OF PROGRAM MANAGER WILLIAM ANDERSON; AND GRANT CMS-9416174 UNDER THE DIRECTION OF PROGRAM MANAGER CLIFFORD ASTILL). THE INVESTIGATION WAS CONDUCTED UNDER THE SUPERVISION OF PROFESSOR WILFRED D. IWAN. ANY OPINIONS, FINDINGS, CONCLUSIONS OR RECOMMENDATIONS EXPRESSED IN THE PUBLICATION ARE THOSE OF THE AUTHOR AND DO NOT NECESSARILY REFLECT THE VIEWS OF KAJIMA CORPORATION OR THE NATIONAL SCIENCE FOUNDATION.

Active Interaction Control for Civil Structures

Thesis by

Luo-Jia Wang

In Partial Fulfillment of the Requirements

for the Degree of

Doctor of Philosophy

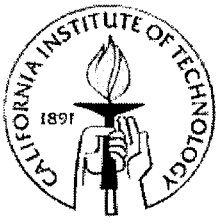

California Institute of Technology

Pasadena, California

1997

(Submitted May 16, 1997)

To my dear motherland - the People's Republic of China.

Acknowledgments

I couldn't have been more fortunate to have Professor Wilfred D. Iwan as my advisor, for whose outstanding guidance and strong support, I would like to express my sincerest gratitude.

I want to thank the entire faculty of Thomas Laboratory for making my graduate study at the California Institute of Technology such a challenging and wonderful experience. In particular, I want to thank the members of my thesis defense committee - Professors James L. Beck, John F. Hall, Thomas H. Heaton, George W. Housner, and Wilfred D. Iwan, for reviewing the thesis. It is my great honor to have Professor Housner's presence on my thesis defense committee.

Technical assistance from Sharon V. Beckenbach, Leslie A. Crockett, Jim O'Donnell, Denise Okamoto, and Connie S. Yehle is much appreciated.

Thanks also go to Professor Leon R.L. Wang, my former advisor at the Old Dominion University, for motivating and assisting me in pursuing doctoral study at the California Institute of Technology.

The generous financial support from the California Institute of Technology, the Charles Lee Powell Foundation, and the Kobori Research Complex of the Kajima Corporation is acknowledged.

Finally, I want to express my deep gratefulness to my family and relatives for their love and support which made this mission possible.

Abstract

This thesis presents a civil engineering approach to active control for civil structures. The proposed control technique, termed Active Interaction Control (AIC), utilizes dynamic interactions between different structures, or components of the same structure, to reduce the resonance response of the controlled or primary structure under earthquake excitations. The primary control objective of AIC is to minimize the maximum story drift of the primary structure. This is accomplished by timing the controlled interactions so as to withdraw the maximum possible vibrational energy from the primary structure to an auxiliary structure, where the energy is stored and eventually dissipated as the external excitation decreases. One of the important advantages of AIC over most conventional active control approaches is the very low external power required.

In this thesis, the AIC concept is introduced and a new AIC algorithm, termed Optimal Connection Strategy (OCS) algorithm, is proposed. The efficiency of the OCS algorithm is demonstrated and compared with two previously existing AIC algorithms, the Active Interface Damping (AID) and Active Variable Stiffness (AVS) algorithms, through idealized examples and numerical simulations of Single- and Multi-Degree-of Freedom systems under earthquake excitations. It is found that the OCS algorithm is capable of significantly reducing the story drift response of the primary structure. The effects of the mass, damping, and stiffness of the auxiliary structure on the system performance are investigated in parametric studies. Practical issues such as the sampling interval and time delay are also examined. A simple but effective predictive time delay compensation scheme is developed.

Table of Contents

Control what we can, manage what we cannot.

Chapter 1

Introduction

1.1 Energy, Energy, and Energy

During an earthquake, the rapid motion of the ground inputs a great deal of vibrational energy into a structure. Part of the energy is dissipated through the internal damping of the structure. The remainder is stored in the form of kinetic energy and strain energy. In a strong earthquake, however, if the amount of the imported energy becomes significantly large over a short period of time, the structure will not be able to absorb it all in elastic energy, for the stresses will reach the elastic limit of certain structural members. Hence, to withstand the seismic environment without failing, the structure must absorb the excessive amount of vibrational energy through plastic deformations of yielded members [Housner, 1956].

Civil structures are conventionally designed to respond to external dynamic loads in a passive fashion. Common seismic design practice permits design for loads lower than those expected on the premise that plastic deformations in an appropriately designed structure will provide that structure with significant energy dissipation potential and enable it to survive a severe earthquake without collapse. Typically, plastic deformations are designated to occur in specially detailed regions of the structure, mostly in beams adjacent to the beam-column joints. While able to dissipate substantial vibrational energy,

the resulting large story drift often causes extensive damage to the structural members and nonstructural architectural elements.

1.2 Current Passive and Active Control Practices

The installation of energy dissipation devices in structures is the most common passive control technique for reducing the energy dissipation demand on primary structural members. Most civil structures possess large mass and high rigidity. To achieve a sufficient amount of damping so as to reduce the seismic response of structures to an admissible level, a considerably large number of damping devices with very high energy dissipation capacity is normally required. Such requirements, however, are often economically impractical. Further, energy dissipation devices are the most effective in absorbing vibrational energy in a steady-state motion, whereas the vibration of civil structures in a seismic environment is usually transient in nature.

Tuned mass damper systems, another type of passive control device, have been installed on the top of many high-rise buildings to counter balance earthquake induced loads. Such systems are mostly designed to control the fundamental mode of buildings, and hence are not necessarily effective for seismically induced vibration. In addition, a larger mass is normally needed for taller buildings. The large stroke produced by the tuned mass damper may raise a significant safety concern.

Active or hybrid mass damper systems may control multiple vibration modes and can relax the requirements for large mass and stroke. However, due to the power limitations of actuators, the capacity of active control systems is generally restricted to ensuring human comfort, and is not used to protect the structure itself under earthquake excitations.

Much of the theoretical basis of active control for civil structures over the last twenty years is rooted in classical and modern control theories which were mainly developed for electrical and mechanical engineering applications. For instance, most prevailing active

control algorithms in civil engineering applications are based on the principle of the Linear Quadratic Regulator (LQR) and the H_∞ formulation. However, it needs to be recognized that active control for civil structures has many distinctive features that radically differ from those in electrical and mechanical engineering. Table 1.2.1 summarizes some key features associated with civil engineering structural control. These features suggest that there is a need to look beyond the conventional techniques of electrical and mechanical engineering and take a fresh look from a civil engineering perspective at techniques that may be more pertinent for civil engineering structural control [Housner, *et al.*, 1994].

Table 1.2.1: Some distinguishing features of civil engineering structural control

Structure	Huge mass, low damping, and high rigidity
Control objective	Reduction of selected maximum response
Control strategy	Simple and perhaps sub-optimal
Energy	Large energy supply required
Actuation	Large control force required

1.3 How Much is Enough

Before proceeding to further detailed discussions on control approaches and algorithms, it is informative at this early stage to answer two most important questions in active control for civil structures: how large a control force does an actuator have to apply and how much external energy is needed to control a civil structure?

To answer this question, consider an *N*-story shear building controlled by a velocity feedback actuator at the roof. The first mode response of the building may be described as

$$\ddot{y}_1(t) + 2\zeta_1\omega_1\dot{y}_1(t) + \omega_1^2 y_1(t) = \eta_1 a(t) - \eta_2 f(t) \tag{1.3.1}$$

where $y_1(t)$ is the first mode response at time t, ω_1 and ζ_1 are respectively the frequency and damping ratio of the first mode, $a(t)$ is the external excitation, and $f(t)$ the linear velocity feedback control force

$$f(t) = p\dot{y}_1(t) \tag{1.3.2}$$

where p is a positive constant to be determined. η_1 and η_2, the modal participation factors, are given by

$$\eta_1 = \frac{\int_0^H \phi_1(z)mdz}{\int_0^H \phi_1^2(z)mdz} = \frac{4}{\pi}, \quad \eta_2 = \frac{\int_0^H \phi_1(z)\delta(z-H)dz}{\int_0^H \phi_1^2(z)mdz} = \frac{2}{Hm} = \frac{2}{M} \tag{1.3.3}$$

where $\phi_1(z)$, the mode shape of the first mode, is taken to be

$$\phi_1(z) = \sin(\frac{\pi z}{2H}) \tag{1.3.4}$$

where H is the height of the building, z is measured from the base of the building, m is the mass of building per unit height, which is assumed to be uniformly distributed along the height, and M is the total mass of the building.

Substituting Equation (1.3.2) into (1.3.1) and rearranging yields

$$\ddot{y}_1(t) + 2\hat{\zeta}_1\omega_1\dot{y}_1(t) + \omega_1^2 y_1(t) = \eta_1 a(t) \tag{1.3.5}$$

where the equivalent damping ratio of the controlled building, $\hat{\zeta}_1$, is given by

$$\hat{\zeta}_1 = \zeta_1\left(1 + \frac{p\eta_2}{2\zeta_1\omega_1}\right). \tag{1.3.6}$$

Therefore for the first mode response, applying a velocity feedback control force to the building is equivalent to increasing the damping of the building.

For simplicity, assume that the external excitation is a harmonic function with a frequency that is very close to that of the first mode of the building. For small $\hat{\zeta}_1$, the dynamic amplification factor (AF) of the controlled first mode at resonance becomes

$$AF(\hat{\zeta}_1) = \frac{1}{2\hat{\zeta}_1\sqrt{1-(\hat{\zeta}_1)^2}} \approx \frac{1}{2\hat{\zeta}_1} = \frac{1}{2\zeta_1\left(1 + \frac{p\eta_2}{2\zeta_1\omega_1}\right)} = \frac{1}{1 + \frac{p\eta_2}{2\zeta_1\omega_1}} AF(\zeta_1). \tag{1.3.7}$$

Therefore, to reduce the AF by 50%, i.e.,

$$AF(\hat{\zeta}_1) = (1.00 - 50\%) = 50\% AF(\zeta_1) \tag{1.3.8}$$

it requires that

$$\frac{p\eta_2}{2\zeta_1\omega_1}=1 \tag{1.3.9}$$

or

$$p=\frac{2\zeta_1\omega_1}{\eta_2}=M\zeta_1\omega_1. \tag{1.3.10}$$

Comparing Equation (1.3.9) with Equation (1.3.6) shows that in order to cut the resonance response of the first mode by 50%, the control effect achieved by the actuator is equivalent to increasing the damping ratio of the first mode by 100%.

Assume that the response of the building is dominated by the first mode and the maximum story drift of the building occurs in the 1st story. Then, the maximum story drift of the building, D_{max}, will be related to the modal displacement as

$$D_{\max}\approx\frac{|x(h,t)|_{\max}}{h}=\frac{\phi_1(h)|y_1(t)|_{\max}}{h}=\frac{\sin(\frac{\pi h}{2H})}{h}|y_1(t)|_{\max}\approx\frac{\pi}{2H}|y_1(t)|_{\max} \tag{1.3.11}$$

where $h = H/N$ is the story height and $x(h,t)$ is the 1st floor response of the building between the 1st floor slab and the ground at time t. From Equation (1.3.11),

$$|y_1(t)|_{\max}\approx\frac{2HD_{\max}}{\pi}. \tag{1.3.12}$$

Assume that

$$h=3.5 \text{ meters},\ D_{max}=1\% \tag{1.3.13}$$

then

$$|y_1(t)|_{max}=0.0223\,N \text{ meters}. \tag{1.3.14}$$

Let the 1st floor response of the building be characterized by D_{max}, then the maximum control force the actuator has to supply is

$$|f(t)|_{\max}=p|\dot{y}_1(t)|_{\max}\approx p\omega_1|y_1(t)|_{\max}=0.0223M\zeta_1\omega_1^2N. \tag{1.3.15}$$

Note that

$$\omega_1=\frac{2\pi}{T_1},\quad M=\frac{NW_0}{g},\quad g=9.81 \text{ m/s/s} \tag{1.3.16}$$

and assume that

$$\zeta_1 = 4\%, \quad T_1 \approx \frac{N}{10}, \tag{1.3.17}$$

where T_1 is the fundamental period of the building and W_0 is the story weight of the building. Equation (1.3.15) becomes

$$|f(t)|_{\max} \approx 0.36 W_0 . \tag{1.3.18}$$

Hence, in order to reduce the resonance response of the first mode by 50%, the maximum control force the actuator has to apply to the building is equivalent to 36% of the story weight of the building.

The work done by the actuator in one cycle of motion is

$$\Delta E = \int_0^{T_1} f_1(t)\dot{y}_1(t)dt \tag{1.3.19}$$

where

$$f_1(t) = p\dot{y}_1(t) \tag{1.3.20}$$

and

$$y_1 \approx |y_1(t)|_{\max} \sin(\omega_1 t + \varphi) \tag{1.3.21}$$

where φ is the phase angle.

Substituting Equations (1.3.20) and (1.3.21) into Equation (1.3.19) and integrating yields

$$\Delta E = \pi p \omega_1 |y_1(t)|^2_{\max} = \pi M \zeta_1 \omega_1^2 (0.023N)^2 . \tag{1.3.22}$$

Substituting Equations (1.3.16) and (1.3.17) into Equation (1.3.20) yields

$$\Delta E = W(0.025 meter) . \tag{1.3.23}$$

Therefore, in order to reduce the resonance response of the first mode by 50%, the energy supplied to the actuator in one cycle of motion is equivalent to lifting the *N*-story building up by 0.025 meter (2.5 cm or 1 inch).

It is important to note that in Equation (1.3.18) the control force required to reduce the resonance response of the first mode by 50% is proportional only to the story weight of the building and does not change with respect to the number of stories of the building. Thus, in a rough sense, the force needed to control a 10-story building will be the same as that needed to control a 20- or 30-story building.

However, Equation (1.3.23) shows that to achieve such control effect, the external energy needed in one cycle of motion is equivalent to lifting the building up by 2.5 cm. Hence, even though a massive actuator could be built to generate a gigantic control force with which to control a high-rise building, the amount of energy required to drive this actuator would eventually become unachievable, as the building is too heavy or the number of cycles of vibration is too large.

1.4 A Dream

To conquer the energy barrier in controlling a civil structure, it is proposed that a future civil structure, into which active control is incorporated, may be built in such a configuration: a primary structure (PS), an auxiliary structure (AS), and an active interaction element (IE) in between. The PS is a regular structure designed to carry ordinary loads. The AS is a special structure, such as a bracing system, designated to withstand extraordinary loads, such as an earthquake or strong wind. The IE is an actively controlled linking device, such as hydraulic valves or friction plate, which may be operated in either a completely free, rigid, or viscous state. The PS and AS can be built as two separate structures or different parts of the same structure.

During an earthquake, the PS and AS are actively attached or detached by the IE to establish a desirable dynamic interaction according to a pre-determined control algorithm. As a result of the attachment and detachment between the PS and AS, the structural configuration (mass and stiffness) of the whole system is actively altered so that the amount of energy flows into the system is minimized. Furthermore, as a result of the controlled interactions between the PS and AS via the IE, excessive vibrational energy in the PS can be transferred to the AS, where the energy can be stored and eventually dissipated as the external excitation decreases.

It is such a thought that originally motivated this research on active control for civil structures, which is now termed Active Interaction Control (AIC) [Iwan, *et al.*, 1996].

Chapter 2

Single-Degree-of-Freedom Systems

The seismic response and characteristics of an AIC system are investigated in this chapter wherein the PS and AS are each modeled by a Single-Degree-of-Freedom (SDOF) system. Underlying assumptions and control objective of the AIC concept are first described. The control efficiencies of the proposed algorithm is then demonstrated and compared with two previously existing AIC algorithms through time history and Response Spectrum analyses of the AIC system in an idealized forced vibration, an idealized free vibration, and earthquake ground motions. The effects of mass, damping, and stiffness of the AS on the response of the PS are investigated in parametric studies. Practical issues such as the sampling interval and time delay on the system performance are also examined. A simple predictive time delay compensation scheme is developed.

2.1 The Active Interaction Control Concept (SDOF)

2.1.1 Underlying Assumptions

Unless otherwise specified in later sections, the following characteristics of the AIC system are assumed throughout this chapter.

1. Only the response of the AIC system in the horizontal direction is considered.
2. The deformations and stresses of the PS and AS are within elastic limits.

3. The mass, damping, and stiffness of the AIC system remain unchanged during each attachment or detachment interval but may vary after each attachment or detachment.
4. The connection between the PS and AS is either completely rigid (at attachment) or completely free (at detachment), i.e., the dynamics of the IE are neglected. The impact between the PS and AS at attachment and the resulting vibrational energy loss are neglected.
5. The attachments and detachments between the PS and AS are realized instantaneously as soon as control decisions are commanded, i.e., no time delay exists in the system.
6. Compared to the PS, the AS has a much smaller mass, a comparable damping ratio, a larger stiffness, and therefore a much higher natural frequency.
7. The displacements and velocities of the PS and AS and the ground accelerations are measured at small sampling intervals.

2.1.2 Problem Formulation

Consider a PS and an AS of an AIC system simultaneously excited by a base acceleration, $a(t)$ (see Figure 2.1.1). The equations of motion of the two structures are given by

$$\left.\begin{aligned} m_1\ddot{x}_1 + c_1\dot{x}_1 + k_1x_1 &= -m_1a(t) + f(x_1, x_2, \dot{x}_1, \dot{x}_2) \\ m_2\ddot{x}_2 + c_2\dot{x}_2 + k_2x_2 &= -m_2a(t) - f(x_1, x_2, \dot{x}_1, \dot{x}_2) \end{aligned}\right\} \tag{2.1.1}$$

where m_1, c_1, k_1 and m_2, c_2, k_2 are respectively the mass, damping, and stiffness of the PS and AS, x_1 and x_2 are respectively the displacements of the PS and AS relative to the ground, and $f = f(x_1, x_2, \dot{x}_1, \dot{x}_2)$ is the interaction or control force between the PS and AS.

When the PS and AS are detached, $f = 0$. The motions of the two structures are independently governed by the detached equations of motion

$$\left.\begin{aligned} m_1\ddot{x}_1 + c_1\dot{x}_1 + k_1x_1 &= -m_1a(t) \\ m_2\ddot{x}_2 + c_2\dot{x}_2 + k_2x_2 &= -m_2a(t) \end{aligned}\right\}. \tag{2.1.2}$$

When the PS and AS are attached, f is determined by the dynamic interaction between the two structures. If the last attachment was realized at time, t_i, and has been maintained thereafter, the displacement of the AS during the course of attachment can be expressed as the sum of the displacement of the PS and the relative displacement between the PS and AS at the initiation of the attachment, i.e.,

$$x_2(t) = x_1(t) + [x_2(t_i) - x_1(t_i)], \quad \dot{x}_2(t) = \dot{x}_1(t), \quad \ddot{x}_2(t) = \ddot{x}_1(t). \tag{2.1.3}$$

Combining Equations (2.1.1) and (2.1.3) yields the attached equation of motion for the PS

$$(m_1 + m_2)\ddot{x}_1 + (c_1 + c_2)\dot{x}_1 + (k_1 + k_2)x_1 = -(m_1 + m_2)a(t) - k_2[x_2(t_i) - x_1(t_i)]. \tag{2.1.4}$$

Several remarks on the AIC concept are now in order.

1. By comparing Equations (2.1.1) with (2.1.2), it is seen that a control force, f, can be generated and applied to the PS simply by attaching and detaching to the AS.
2. The AS acts as an actuator which generates the control force, f, on the PS. The second line in Equations (2.1.1) and (2.1.2) describes the actuator dynamics.
3. There is no need for any additional external energy in order to drive the AS to generate the control force, f.
4. By comparing Equation (2.1.4) with the first line in Equation (2.1.2), it is seen that the structural properties of and the effective loads on the PS are modified by the active interaction between the PS and AS. Hence, a properly controlled PS will be able to react to external loads in a favorable manner just as a 'smart' structure.

2.1.3 Control Objectives

An appropriate control criterion depends on the nature of external loads and the response quantities of interest. Generally speaking, for a near-field earthquake with a pulse-like time history, the main control objective is to minimize the maximum story drift of the PS. For a SDOF system, the story drift is the displacement of the PS relative to the ground.

For a far-field earthquake with its more random-appearing time history, an additional control objective is to reduce the absolute acceleration of the PS so as to protect structural contents and improve the comfort of occupants.

The essence of the AIC algorithms is maximization of the effective hysteretic energy dissipation of the PS. This is accomplished by timing the interactions between the PS and AS. The vibrational energy withdrawn from the PS is transferred to the AS via the IE. Damping devices may be attached to the AS to damp out the stored vibrational energy after the interactions between the PS and AS are terminated and the external excitation decreases.

2.1.4 Control Algorithms

Let the velocity and displacement of the PS and AS be sampled in the time domain with a sampling interval, Δt. Then, the proposed control algorithm may be described as follows:

- An attachment between the PS and AS will be initiated at time t and maintained for the sampling interval, Δt, or maintained from time t to $t+\Delta t$ if the attachment is already in effect, provided the following three conditions are satisfied
  1. $[\dot{x}_1(t)-\dot{x}_2(t)][\dot{x}_1(t-\Delta t)-\dot{x}_2(t-\Delta t)]\le 0$,
  2. $\dot{x}_1(t)\,x_2(t)\ge 0$, and
  3. $\dot{x}_1(t)\,\dot{x}_1(t-\Delta t)\ge 0$.
- In all other cases, the PS and AS will be detached.

Condition 1 assures that the velocities of the PS and AS at attachment are almost equal and there will be minimum dynamic attachment impact on the IE. Condition 2 assures that the interaction force which the AS exerts on the PS will be opposite in direction to the current direction of PS motion. Note that for cases in which the AS yields, condition 2 should be modified as $\dot{x}_1(t)\,f_2(t)\ge 0$, where $f_2(t)$ is the hysteresis force acting on the AS. Condition 3 states that the PS velocity has not yet changed direction and the

displacement of the PS is continuously increasing or continuously decreasing. These three conditions together assure that the effective hysteretic restoring force on the PS will be as large as possible, resulting in maximum vibrational energy loss for the PS.

Two previously existing control algorithms under the class of AIC, namely, the Active Interface Damping (AID) control algorithm [Hayen, *et al.*, 1994; Hayen, 1995] and the Active Variable Stiffness (AVS) control algorithm [Kobori, *et al.*, 1992, 1993; Yamada, *et al.*, 1995], are described in Appendices A.1 and A.2, respectively. Table 2.1.1 summarizes the characteristics of the proposed, AID, and AVS control algorithms.

Table 2.1.1: Characteristics of the proposed, AVS, and AID Control Algorithms

Algo.	Attachment Condition	AS Dynamics	IE Operation State
Prop.	$[\dot{x}_1(t)-\dot{x}_2(t)][\dot{x}_1(t-\Delta t)-\dot{x}_2(t-\Delta t)]\le 0$ $\dot{x}_1(t)\,x_2(t)\ge 0$ $\dot{x}_1(t)\,\dot{x}_1(t-\Delta t)\ge 0$	Utilized	Free/Rigid
AID	$E_A^*(t+\Delta t) < E_D^*(t+\Delta t)$	Neglected	Free/Viscous/Rigid
AVS	$\dot{x}_1(t)\,x_1(t) > 0$	Neglected	Free/Rigid

* $E_A(t+\Delta t)$ and $E_D(t+\Delta t)$ are the total relative vibrational energy in the PS for the cases when the PS is attached to and detached from the AS during the sampling interval, $[t, t+\Delta t]$, respectively.

It should be noted that the dynamics of the AS are fully neglected in the AID and AVS algorithms. Thus, dynamic impact always occurs in the IE as the PS and AS are attached when moving at different velocities. This is an important issue that has not been adequately addressed in the AID and AVS algorithms.

2.1.5 Numerical Algorithm

Both the detached and attached equations of motion of the AIC system, i.e., Equations (2.1.2) and (2.1.4), are in the form

$$M\ddot{X}(t)+C\dot{X}(t)+KX(t)=MLa(t)+F(t) \tag{2.1.5}$$

where M, C, K, and X are the mass, damping, and stiffness matrices and relative displacement vector of the whole AIC system respectively, $a(t)$ symbolizes the external excitation, $F(t)$ represents the control force between the PS and AS, and

$$L=[1 \quad 1 \quad 1\cdots\cdots 1 \quad 1 \quad 1]^T. \tag{2.1.6}$$

The entries in M, C, K, and F usually vary after each attachment or detachment due to the change of structural configurations and locations of the control forces. The response of an AIC system is therefore nonlinear (piece-wise linear) in time.

Rewrite Equation (2.1.5) in state-space representation

$$\dot{Y}(t) = AY(t) + B(t) + H(t) \tag{2.1.7}$$

where

$$Y(t)=\begin{Bmatrix} X(t) \\ \dot{X}(t) \end{Bmatrix}, A=\begin{bmatrix} \Theta & I \\ -M^{-1}K & -M^{-1}C \end{bmatrix}, B(t)=\begin{Bmatrix} \Phi \\ La(t) \end{Bmatrix}, H(t)=\begin{Bmatrix} \Phi \\ M^{-1}F(t) \end{Bmatrix} \tag{2.1.8}$$

and where Θ and I are the null and identity matrices respectively, and Φ is the null vector.

To solve Equation (2.1.7), time domain integration is employed in this study. For a small sampling interval, Δt, the operation of integration may be replaced by computational approximations based on multiplication and addition. Let $Y_{i+1} = Y((i+1)\Delta t)$, then the discrete solution to Equation (2.1.7) at time $(i+1)\Delta t$ is

$$Y_{i+1} = P_i Y_i + Q_i + R_i \tag{2.1.9}$$

where

$$P_i = e^{A_i \Delta t}, \quad Q_i = A_i^{-1}(P_i - I)B_i, \quad R_i = A_i^{-1}(P_i - I)H_i. \tag{2.1.10}$$

In later analyses when the AS is allowed to yield after reaching its elastic limit, the matrix A becomes singular and does not have an inverse. In this case, Q_i and R_i may be written in an alternative form

$$Q_i = \frac{\Delta t}{2}(P_i + I)B_i, \quad R_i = \frac{\Delta t}{2}(P_i + I)H_i. \tag{2.1.11}$$

Equation (2.1.9) is solved using Matlab, which is especially suited for conducting matrix operations.

2.2 Two Idealized Cases

This section demonstrates the AIC concept in two idealized examples, a harmonically forced vibration and a undamped free vibration. Both numerical and analytical results of the response of an AIC system are presented. Comparisons between uncontrolled and controlled response of the PS are made.

2.2.1 Harmonically Forced Vibration

Consider an AIC system in a harmonically forced vibration with fixed displacement limits, $\pm x_0$. Figures 2.2.1 to 2.2.3 plot the first full cycle motion of the PS and AS and the control force-displacement curve (f-x_1) of the PS obtained from the proposed, AID, and AVS algorithms.

In Figure 2.2.1, it is seen that for the proposed algorithm, the initially attached PS and AS move from A along a straight control force-displacement line which has a slope k_2. From B, the displacement of the PS begins to reverse direction, the PS and AS are detached, and the control force on the PS drops to zero at C. Since the fundamental frequency of the AS is much larger than that of the PS, the PS and AS will be reattached at D when the velocity of the AS again catches up with that of the PS. A change of control force from D to E, which is approximately the same magnitude as the previous control force drop from B to C, will act upon the PS at attachment. Such detaching and attaching cycles are repeated at later times.

Because the stiffness of the PS acts as an elastic spring and does not dissipate energy, the area within the closed control force-displacement loop is the same as the area in a conventional hysteresis loop (restoring force-displacement curve), which represents the vibrational energy withdrawn from the PS to the AS. It is seen from Figure 2.2.1 that the magnitude of the effective control force increases after each half cycle, for example, from

B to C and from F to G, creating larger and larger hysteresis loops. This indicates that more vibrational energy is withdrawn from the PS to the AS in each subsequent cycle.

The AID control algorithm employs an energy removal concept similar to the proposed algorithm. However, the AS is assumed to relax back to its zero position instantaneously after a detachment. A new attachment between the PS and AS is made as soon as the AS returns to its zero position. Such kind of motion results in a 'parallelogram' type control force-displacement loop with a constant area enclosed, as displayed in Figure 2.2.2.

The AVS control algorithm allows interaction between the PS and AS only when the PS is 'unloading' every other quarter cycle of motion. The PS and AS are left unattached during the rest part of the motion when the PS is 'loading.' Hence, the control force-displacement loop becomes a 'butterfly' type curve with a constant area enclosed, as shown in Figure 2.2.3.

It is clearly seen from Figures 2.2.1 to 2.2.3 that the area enclosed by the control force-displacement curve corresponding to the proposed algorithm gives the largest area in contrast to the AID and AVS algorithms. This is because the two latter algorithms have not made full use of the dynamics of the AS.

Let the mass, damping, and stiffness of the AS be related to those of the PS as

$$m_2 = \alpha m_1, \quad \zeta_2 = \beta \zeta_1, \quad k_2 = \gamma k_1 \tag{2.2.1}$$

where ζ_1 and ζ_2, the damping ratios of the PS and AS respectively, are defined as

$$\zeta_1 = \frac{c_1}{2\sqrt{m_1 k_1}}, \quad \zeta_2 = \frac{c_2}{2\sqrt{m_2 k_2}}. \tag{2.2.2}$$

Then from Assumption 6 in Section 2.1.1,

$$\alpha << 1, \quad \gamma > 1, \quad \sqrt{\frac{\gamma}{\alpha}} >> 1. \tag{2.2.3}$$

Since in this idealized case the system is undamped, $c_1 = c_2 = \zeta_1 = \zeta_2 = 0$.

The peak displacement of the AS in the first cycle of motion for the case of the proposed algorithm can be found from Figure 2.2.1

$$\begin{aligned} x_{2,1} &= \max_{t=[0,T]} |x_2(t)| = AC + DG + HA = AC + (CG - CD) + (GA - GH) \\ &= (AC + GA) + CG - (CD + GH) = 2CG - (CD - GH) \\ &= 2PP_1 - (CD + GH) \end{aligned} \tag{2.2.4}$$

where $x_{2,i}$ denotes the peak displacement of the AS in the ith cycle of motion, PP_i represents the peak-to-peak displacement of the PS in the ith of cycle motion, T is the period of the attached PS and AS, i.e.,

$$T = \frac{2\pi}{\omega} = \frac{2\pi}{\sqrt{\frac{k_1 + k_2}{m_1 + m_2}}} = \frac{2\pi}{\sqrt{\frac{1+\gamma}{1+\alpha}}\omega_1} = \sqrt{\frac{1+\alpha}{1+\gamma}}T_1 \tag{2.2.5}$$

and

$$\begin{aligned} CD + GH &= PP_1\left[1 - \cos\left(\frac{\omega T_2}{2}\right)\right] = PP_1\left[1 - \cos\left(\sqrt{\frac{1+\gamma}{1+\alpha}}\frac{\omega_1}{\omega_2}\pi\right)\right] \\ &= PP_1\left[1 - \cos\left(\sqrt{\frac{1+\gamma}{1+\alpha}}\sqrt{\frac{\alpha}{\gamma}}\pi\right)\right] = PP_1 2\sin^2\left[\sqrt{\frac{\alpha(1+\gamma)}{\gamma(1+\alpha)}}\frac{\pi}{2}\right] \\ &\approx 2PP_1\left[\sqrt{\frac{\alpha(1+\gamma)}{\gamma(1+\alpha)}}\frac{\pi}{2}\right]^2 \approx \frac{5\alpha(1+\gamma)}{\gamma(1+\alpha)}PP_1 \end{aligned} \tag{2.2.6}$$

where T_1, ω_1 and T_2, ω_2 are the natural periods and frequencies of the PS and AS, respectively. For the α and γ assumed in Equation (2.2.3),

$$\frac{5\alpha(1+\gamma)}{\gamma(1+\alpha)} \approx \frac{5\alpha(1+\gamma)}{\gamma} = 5\alpha\left(\frac{1}{\gamma} + 1\right) << 1. \tag{2.2.7}$$

Substituting Equation (2.2.6) into (2.2.4) yields

$$x_{2,1} = \left[2 - \frac{5\alpha(1+\gamma)}{\gamma(1+\alpha)}\right]PP_1 \tag{2.2.8}$$

from which the peak displacement of the AS in the nth cycle of motion can be inferred

$$x_{2,n} = \max_{t=[0,nT]} |x_2(t)| = \left[2 - \frac{5\alpha(1+\gamma)}{\gamma(1+\alpha)}\right]\sum_{i=1}^{n} PP_i . \tag{2.2.9}$$

Note that in Figure 2.2.1, lines AB, EF, and IJ all have a slope, k_2. Therefore, we can extrapolate trapezoids DEFG and HIJA side by side on the x_1 axis to the right of triangle ABC to make up a big triangle AJK. The area of the triangle AJK is apparently identical to the area of polygon ABCDEFGHIJA. Hence, the total vibrational energy withdrawn from the PS to the AS in the first cycle of motion (the area of triangle AJK) is simply

$$E_1 = (\Delta E)_1 = \frac{1}{2} AK \cdot KJ = \frac{1}{2}(x_{2,n})(k_2 x_{2,n}) = \frac{1}{2} k_2 x_{2,n}^2 = \frac{1}{2} k_2 \left[2 - \frac{5\alpha(1+\gamma)}{\gamma(1+\alpha)} \right]^2 PP_1^2 \quad (2.2.10)$$

from which the total vibrational energy withdrawn from the PS to the AS in the first n cycles of motion can be inferred

$$E_n = \sum_{i=1}^{n} (\Delta E)_i = \frac{1}{2}(x_{2,n})(k_2 x_{2,n}) = \frac{1}{2} k_2 x_{2,n}^2 = \frac{1}{2} k_2 \left[2 - \frac{5\alpha(1+\gamma)}{\gamma(1+\alpha)} \right]^2 \left(\sum_{i=1}^{n} PP_i \right)^2 . \quad (2.2.11)$$

In particular, the vibrational energy withdrawn from the PS to the AS in the single nth cycle of motion is

$$(\Delta E)_n = E_n - E_{n-1} . \quad (2.2.12)$$

Likewise, the peak displacement of the AS in the nth cycle of motion and the total vibrational energy withdrawn from the PS to the AS in the first n cycles of motion for the AID and AVS algorithms can be obtained

$$\text{AID:} \quad x_{2,n} = PP_n, \quad E_n = \sum_{i=1}^{n} (\Delta E)_i = \sum_{i=1}^{n} 2\left(\frac{1}{2} k_2 x_{2,i}^2\right) = k_2 \sum_{i=1}^{n} (PP_i)^2 \quad (2.2.13)$$

$$\text{AVS:} \quad x_{2,n} = P_n, \quad E_n = \sum_{i=1}^{n} (\Delta E)_i = \sum_{i=1}^{n} 2\left(\frac{1}{2} k_2 x_{2,i}^2\right) = k_2 \sum_{i=1}^{n} (P_i)^2 \quad (2.2.14)$$

where P_i denotes the peak displacement of the PS in the ith cycle of motion.

The efficiencies of proposed, AID, and AVS control algorithms may be evaluated from another angle, that is to examine the effective equivalent damping ratio of the system, which is defined as the damping ratio for an uncontrolled system that would yield the same amount of vibrational energy dissipation per cycle as is obtained for the controlled system.

The vibrational energy dissipated through the damping in the nth cycle of motion is

$$(\Delta E)_n = \int_0^T c_1 \dot{x}_1^2(t)dt \tag{2.2.15}$$

where

$$T = \frac{2\pi}{\omega}, \quad c_1 = 2m_1\omega(\zeta_{eq})_n \tag{2.2.16}$$

and

$$x_1(t) = x_0 \sin(\omega t + \varphi) \tag{2.2.17}$$

where φ is the phase angle.

Substituting Equations (2.1.16) and (2.1.17) into Equation (2.1.15) yields

$$(\Delta E)_n = 2\pi m_1 \omega^2 (\zeta_{eq})_n x_0^2 \tag{2.2.18}$$

from which

$$(\zeta_{eq})_n = \frac{(\Delta E)_n}{4\pi E_0} \tag{2.2.19}$$

where

$$E_0 = \frac{1}{2} m_1 \omega^2 x_0^2 . \tag{2.2.20}$$

Tables 2.2.1 to 2.2.3 summarize the numerical values of the total vibrational energy withdrawn from the PS to the AS in the first n cycles of motion, the vibrational energy withdrawn from the PS to the AS in the nth cycle of motion, and the equivalent damping ratio for the proposed, AID, and AVS algorithms. In these cases, $\alpha = 1\%$, $\gamma = 1$, $x_0 = 1$, $P_i = 1$ and $PP_i = 2$. The term $\frac{5\alpha(1+\gamma)}{\gamma(1+\alpha)}$ is neglected for the small α used.

Table 2.2.1: Total vibrational energy withdrawn from the PS to the AS in the first n cycles of a harmonically forced vibration with fixed displacement limits

Algorithm	E_1/E_0	E_2/E_0	E_3/E_0	E_n/E_0
Proposed	16	64	144	$16n^2\gamma$
AID	8	16	24	$8n\gamma$
AVS	2	4	6	$2n\gamma$

Table 2.2.2: Vibrational energy withdrawn from the PS to the AS in the nth cycle of a harmonically forced vibration with fixed displacement limits

Algorithm	$(\Delta E/E_0)_1$	$(\Delta E/E_0)_2$	$(\Delta E/E_0)_3$	$(\Delta E/E_0)_n$
Proposed	16	48	80	$16(2n\text{-}1)\gamma$
AID	8	8	8	8γ
AVS	2	2	2	2γ

Table 2.2.3: Equivalent damping ratio in the nth cycle of a harmonically forced vibration with fixed displacement limits

Algorithm	$(\zeta_{eq})_1$	$(\zeta_{eq})_2$	$(\zeta_{eq})_3$	$(\zeta_{eq})_n$
Proposed	127%	382%	637%	$4(2n\text{-}1)\gamma/\pi$
AID	64%	64%	64%	$2\gamma/\pi$
AVS	16%	16%	16%	$\gamma/2\pi$

It is important to note that for the proposed algorithm, $(\Delta E)_n$ and $(\zeta_{eq})_n$ increase linearly with the number of cycle, n, and E_n increases with the square of the number of cycle, n^2, whereas for the cases of the AID and AVS algorithms, $(\Delta E)_n$ and $(\zeta_{eq})_n$ remain constants and E_n is a linear function of n. Hence, the vibrational energy withdrawn from the PS to the AS for the proposed algorithm is one order higher than for the AID and AVS algorithms, which explains why the proposed algorithm is superior in reducing the response of the PS compared with the AID and AVS algorithms.

It is also important to note that the amount of vibrational energy withdrawn from the PS to the AS and the equivalent damping ratio are both proportional to the stiffness of the AS, γ. Therefore, increasing the stiffness of the AS is one of the simplest ways to reduce the response of the PS.

In light of the above findings, the proposed control algorithm is capable of withdrawing the maximum possible amount of vibrational energy from the PS to the AS while keeping the dynamic impact between the PS and AS to minimum. Hence, the proposed algorithm is referred to as the Optimal Connection Strategy (OCS) algorithm in the rest of this thesis.

2.2.2 Undamped Free Vibration

Consider a PS at rest, released from its initial position $x_1 = x_0$, and an attached AS at rest at its zero position. It will be shown that in order to generate a control force-displacement curve in all four quadrants in the OCS algorithm, the range of the stiffness ratio between the AS and the AS, γ, is

$$0 < \gamma < 3 - 2\sqrt{2} = 0.183. \tag{2.2.18}$$

In the following numerical and analytical analyses, γ is taken as 0.1.

Using the OCS, AID, and AVS algorithms, the first two cycles of motion of the PS and AS and the control force-displacement curve (f-x_1) of the PS in an undamped free vibration are numerically simulated and plotted in Figure 2.2.4.

The displacements of the PS and AS at the end of the first half and full cycles of motion may also be calculated analytically by the energy method

$$\begin{aligned} E(0) &= \frac{1}{2}k_1 x_0^2 = \\ E(T/2) &= \frac{1}{2}k_1 x_1^2(T/2) + \frac{1}{2}k_2[x_0 + x_1(T/2)]^2 = \\ E(T) &= \frac{1}{2}k_1 x_1^2(T) + \frac{1}{2}k_2[x_0 + 2x_1(T/2) + x_1(T)]^2 \end{aligned} \tag{2.2.19}$$

where T is the period of the attached PS and AS, which is set to 1 second in this example. From Equation (2.2.19), the displacements of the PS at the ends of the first half and full cycles of motion are

$$\left.\begin{aligned} x_{1,1/2} &= |x_1(T/2)| = \frac{2}{1+\gamma}x_0 \\ x_{1,1} &= |x_1(T)| = \frac{\gamma^2 - 6\gamma + 1}{(1+\gamma)^2}x_0 \end{aligned}\right\}, \tag{2.2.20}$$

and the displacements of the AS at the ends of the first half and full cycles of motion are

$$\left.\begin{aligned} x_{2,1/2} &= \left|x_2(T/2)\right| = x_0 + x_{1,1/2} = \frac{3+\gamma}{1+\gamma}x_0 \\ x_{2,1} &= \left|x_2(T)\right| = x_0 + 2x_{1,1/2} + x_{1,1} = \frac{4(1-\gamma)}{(1+\gamma)^2}x_0 \end{aligned}\right\}. \tag{2.2.21}$$

Now the upper limit in Equation (2.2.18) can be verified by putting $x_{1,1} = 0$ in Equation (2.2.20) and solving for γ.

From Equation (2.2.10), the vibrational energy withdrawn from the PS to the AS in the first cycle of motion for the OCS algorithm is

$$E_1 = (\Delta E)_1 = \frac{1}{2}k_2 x_{2,1}^2 = \frac{8k_2(1-\gamma)^2 x_0^2}{(1+\gamma)^4}. \tag{2.2.22}$$

To find the equivalent damping ratio of the system, we first write the peak displacement of the PS in the nth cycle of vibration

$$x_{1,n} = x_0 \exp\left[-\omega_1(\zeta_{eq})_n t_n\right]. \tag{2.2.23}$$

But

$$\frac{(\Delta x_1)_n}{x_{1,n}} = \frac{x_{1,n+1} - x_{1,n}}{x_{1,n}} = \exp\left[-\frac{2\pi(\zeta_{eq})_n}{\sqrt{1-(\zeta_{eq})_n^2}}\right] - 1, \tag{2.2.24}$$

therefore

$$\left(\frac{\Delta E}{E}\right)_n = \frac{\frac{1}{2}k_1 x_{1,n+1}^2 - \frac{1}{2}k_1 x_{1,n}^2}{\frac{1}{2}k_1 x_{1,n}^2} = 2\left[\frac{(\Delta x_1)_n}{x_{1,n}}\right] + \left[\frac{(\Delta x_1)_n}{x_{1,n}}\right]^2 = \exp\left[-\frac{4\pi(\zeta_{eq})_n}{\sqrt{1-(\zeta_{eq})_n^2}}\right] - 1. \tag{2.2.25}$$

From which

$$(\zeta_{eq})_n = \left\{1 + 16\pi^2\left\{\ln\left[(1-\left(\frac{\Delta E}{E}\right)_n\right]\right\}^{-2}\right\}^{-1/2}. \tag{2.2.26}$$

Likewise, the displacement of the PS at the end of the first cycle, the vibrational energy withdrawn from the PS to the AS in the first cycle, and the equivalent damping ratio for the AID and AVS control algorithms can be calculated. Table 2.2.4 summarizes these quantities for the case of $\gamma = 0.1$.

As shown in Figure 2.2.4 and Table 2.2.4, the response of the PS for the OCS algorithm is reduced much faster as compared with those in the AID and AVS algorithms. By the end of the first cycle, the peak displacement of the PS drops to 34% of its initial value for the OCS algorithm, 67% for the AID, and 91% for AVS. Such control effects produced by the OCS, AID, and AVS algorithms are equivalent to attaching a dashpot with damping ratios of 17.3%, 6.3%, and 1.5% to the PS, respectively.

Table 2.2.4: Displacement of the PS at the end of the first cycle, the vibrational energy withdrawn from the PS to the AS in the first cycle, and equivalent damping ratio for the OCS, AID, and AVS algorithms in a undamped free vibration

Algorithm	$x_1(T)/x_0$		$(\Delta E/E_0)_1$		$(\zeta_{eq})_1$
OCS	$\frac{\gamma^2-6\gamma+1}{(1+\gamma)^2}$	34%	$\frac{16\gamma(1-\gamma)^2}{(1+\gamma)^4}$	89%	17.3%
AID	$\frac{(1-\gamma)^2}{(1+\gamma)^2}$	67%	$\frac{8\gamma(1+\gamma^2)}{(1+\gamma)^4}$	55%	6.3%
AVS	$\frac{1}{1+\gamma}$	91%	$\frac{\gamma(2+\gamma)}{(1+\gamma)^2}$	17%	1.5%

* $E_0 = k_1 x_0^2 / 2$

Deeper insights may be found in Figures 2.2.5 to 2.2.7, which plot the control force-displacement curves for the OCS, AID, and AVS algorithms. As pointed out earlier, the area enclosed by the control force-displacement curve, i.e., the hysteresis loop, symbolizes the vibrational energy withdrawn from the PS to the AS.

In Figure 2.2.5, the control force-displacement curve for the OCS algorithm possesses a larger enclosed area as compared to the curves for the AID and AVS algorithms in Figures 2.2.6 and 2.2.7. Similar to Figure 2.2.1 for the case of the forced vibration, the control force jump at the end of every half cycle increases the height of the control force-displacement curve in Figure 2.2.5, resulting in a greater enclosed area and thus larger vibrational energy withdrawn from the PS to the AS. As shown in Figure 2.2.6, the control force-displacement curve for the AID algorithm forms a series of shrinking parallelo-

grams, which differ from the curves in Figure 2.2.5 only because of the lack of control force jumps at the ends of every half cycle. With the restriction of attaching the PS and AS only when the PS is 'loading,' the AVS algorithm misses almost half of the opportunities as in the OCS algorithm to transfer energy from the PS to the AS, which yields a butterfly type of curve enclosing a smaller area as in Figure 2.2.7.

2.3 Seismic Responses of SDOF Systems

This section examines the seismic response of AIC systems. Two earthquake accelerograms are employed as the input ground motions at the bases of the PS and AS. They are: the El Centro Station North (ELC) in the 1940 Imperial Valley earthquake and the Rinaldi Station North (RRS) in the 1994 Northridge earthquake. Details of these records are contained in Appendix A.3.

In the following numerical studies, instead of specifying the mass, damping, and stiffness of the PS, the fundamental period and the damping ratio of the PS are prescribed, which are 1 second and 2% respectively. The mass, damping, and stiffness of the AS are related to the PS by taking $\alpha = 4\%$, $\beta = 1$, and $\gamma = 2$, respectively. These parameters are intended to model the period and damping of the first mode of an 8-story (steel frame) shear building which will be revisited in the next chapter. Thus, the response of the SDOF system presented in the subsequent sections of this chapter may also be viewed as the first mode response of an 8-story shear building.

Figures 2.3.1 to 2.3.6 compare the displacement, velocity, and acceleration response time histories of the PS uncontrolled and controlled by the OCS, AID, and AVS algorithms. Tables 2.3.1 to 2.3.2 list the peak and Root-Mean-Square (RMS) values of the quantities plotted in these figures.

As to the displacement response of the PS, a series of gradually increasing harmonic waves of 1 Hz frequency are clearly seen in the uncontrolled case, whereas these reso-

nance buildups are all significantly suppressed in the controlled cases. In fact, the peak displacement in the entire time history of the controlled PS occurs immediately after the first S-wave arrival. The peak displacements at later time are successively diminished. Quantitatively, for the ELC ground motion, the peak displacement of the PS is suppressed from 17 cm for the uncontrolled case to 4 cm for the OCS case, 3 cm for the AID, and 6 cm for the AVS; and for the RRS ground motion, the peak displacement of the PS is suppressed from 52 cm for the uncontrolled case to 7 cm for the OCS case, 13 cm for the AID, and 17 cm for the AVS. In terms of the RMS values of the displacement of the PS, a larger percentage of reduction is observed in all controlled cases. Overall in order, the best control efficiency is achieved in the OCS, AID, and AVS algorithms.

Table 2.3.1: Peak and RMS values of the acceleration, velocity, and displacement of the PS excited by the ELC ground motion uncontrolled and controlled by the OCS, AID, and AVS algorithms

Algorithm	Displacement (cm)		Velocity (cm/s)		Acceleration (cm/s/s)	
	Peak	RMS	Peak	RMS	Peak	RMS
Uncontrolled	17	5.97	118	38.3	677	235
OCS	4	0.75	36	5.8	501	116
AID	3	0.87	30	7.4	517	95
AVS	6	1.71	58	14.0	656	133

Table 2.3.2: Peak and RMS values of the acceleration, velocity, and displacement of the PS excited by the RRS ground motion uncontrolled and controlled by the OCS, AID, and AVS algorithms

Algorithm	Displacement (cm)		Velocity (cm/s)		Acceleration (cm/s/s)	
	Peak	RMS	Peak	RMS	Peak	RMS
Uncontrolled	52	19.4	334	121.7	2069	766
OCS	7	1.6	54	10.3	1089	231
AID	13	2.1	81	21.0	1457	260
AVS	17	3.5	117	25.6	1904	273

As to the velocity and absolute acceleration responses of the PS, significant reduction of both peak and RMS values is achieved in all controlled cases, as compared with the uncontrolled cases. Such simultaneous reduction of displacement, velocity, and accelera-

tion is a major benefit of AIC which can not be achieved in traditional seismic design. To reduce the maximum displacement of a structure in an earthquake, increasing stiffness is probably the only choice in the traditional seismic design practice. In return, however, a stiffer structure attracts larger seismic force and thus large acceleration, which may severely damage the nonstructural architectural elements.

Because of the frequent attachment between the PS and AS, a large amount of high frequency components are introduced in the responses of the controlled PS, especially in the velocity and absolute acceleration responses. After careful examination, it can be seen that the response spikes in the velocity and acceleration responses occur when the PS and AS are attached or detached.

Table 2.3.3 summarizes the number of attachments (or detachments) between the PS and AS in the first four seconds of the ELC and RRS excitations for the OCS, AID, and AVS algorithms. The attachment time histories for these algorithms are plotted in Figures 2.3.7 and 2.3.8. One can see that the numbers of attachments involved in the OCS algorithm are approximately twice as many as those in either the AID or AVS algorithm. This corresponds to more high frequency components in the response of the PS for the OCS algorithm. It is also seen that the number of attachments in each of the AIC algorithms remains almost unchanged from the ELC to the RRS ground motion.

Table 2.3.3: Number of attachments between the PS and AS under the first four second of ELC and RRS excitations for the OCS, AID, and AVS algorithms

	OCS	AID	AVS
ELC	25	14	17
RRS	26	16	15

Figures 2.3.9 and 2.3.10 plot the response of the AS for the OCS algorithm. The plots for the AID and AVS algorithms are omitted as the dynamics of the AS are neglected in these two control algorithms. Table 2.3.4 gives data on the peak values of the quantities in these figures.

It is seen that the displacement, velocity, and acceleration responses of the AS are mostly comprised of high frequency harmonic motions with an identifiable envelope. A few relatively longer period motions are found at each subsequent strong S-wave arrival, signaling the motion of the attached PS and AS. The rest of the high frequency motion describes the vibration of the detached AS. The peak response of the AS also occurs during the first S-wave arrival. Quantitatively, the peak displacement of the AS does not exceed twice that of the PS. However, the peak velocity and acceleration of the AS are much larger than those of the PS. For instance, the peak velocity and acceleration of the AS for the RRS case reach 534 cm/s and 25 g respectively. Apparently, to attach the PS and AS in such a rapid motion requires very small sampling interval and quick reaction of the linking device.

Table 2.3.4: Peak values of the acceleration, velocity, and displacement of the AS excited by the ELC and RRS ground motions for the OCS, AID, and AVS algorithms

Algorithm	Peak Displacement (cm)		Peak Velocity (cm/s)		Peak Acceleration (g)	
	ELC	RRS	ELC	RRS	ELC	RRS
OCS	5	13	226	534	10	25
AID	5	22	30	81	0.58	1.49
AVS	6	17	58	117	0.67	1.94

Special attention should be paid to the AID control algorithm for the cases when the stiffness of the AS becomes large. Figures 2.3.11 and 2.3.12 plot the time history responses of the PS controlled by the AID algorithm when the stiffness of the AS is four times of the PS, i.e., $\gamma = 4$. Although the velocity and acceleration responses of the PS are normally suppressed, a gradually drifting oscillation in small amplitude is observed in the displacement response of the PS. This is because the stiffness of AS is so high that, during 'unloading,' all vibrational energy in the PS has been transferred to the AS before the PS is able to return to its zero position. Such a phenomenon will not happen to the OCS and AVS algorithms, because the OCS algorithm forbids attachments before the AS

vibrates back to its zero position and the AVS algorithm prohibits attachments when the PS is 'unloading.' To prevent the occurrence of the drifting phenomenon in the AID algorithm, a smaller stiffness of the AS ($\gamma < 2$) should be employed.

Figure 2.3.13 depicts the frequency domain response of the displacement of the PS uncontrolled and controlled by the OCS, AID, and AVS algorithms. In the uncontrolled case, an appreciable peak rises at 1 Hz, indicating the resonance of the PS with the ground motion. This resonance peak is significantly suppressed in all controlled cases, especially in the OCS and AID cases. Slightly increased controlled response in the low frequency range is observed in the OCS and AID cases, and a slightly decreased controlled response in the high frequency range is found in all controlled cases. The controlled response oscillates rapidly in the high frequency range as compared to the uncontrolled counterpart, reflecting frequent attachment between the PS and AS.

The efficacy of the AIC algorithms may also be evaluated from the energy point of view. Figure 2.3.14 displays the time histories of the energy flowing into the uncontrolled PS and the energy transferred out of the controlled PS. The doted line symbolizes the energy flowing into the PS for the uncontrolled case, and all other lines represent the energy withdrawn from the PS to the AS for the controlled cases. All plots are normalized by the total energy flowing into the uncontrolled PS by the end of the ground motion.

It is seen that the energy flowing into the uncontrolled PS has the shape of a ramp function. Very little energy enters the PS in the first 2 seconds, but a great amount of energy suddenly rushes into the PS at an extremely fast pace following the first S-wave arrival. Quantitatively, approximately 80% of the total energy flows into the uncontrolled PS within the four-second period after the first S-wave arrival and approximately 90% of the input energy is steadily transferred out of the controlled PS to the AS.

2.4 Parametric Studies

2.4.1 Story Drift Spectrum

In the preceding section, the effectiveness of the AIC algorithms is shown by comparing the controlled seismic response of a prescribed SDOF system with its uncontrolled counterpart. The response of the SDOF system may also be viewed as the first mode response of an 8-story shear building with a 1 second fundamental period and 2% modal damping.

The purpose of this subsection is to investigate if the AIC algorithms are also effective in controlling the seismic motion over a wide range of structures. Such a study is conducted by computing and plotting the Story Drift Spectrum (SDS) of the PS.

As a surrogate of the Displacement Response Spectrum (DRS), the SDS gives a simple and direct measure of the maximum story drift demand of an earthquake ground motion. The SDS for the N-story shear building is defined as

$$D(T_1,\zeta_1) = \eta_1\phi_1\left(\frac{H}{N}\right)SD(T_1,\zeta_1) \tag{2.4.1}$$

where T_1 is the fundamental period of the building, ζ_1 is the damping ratio of the first mode which is taken as 2%, η_1 is the modal participation factor given by Equation (1.3.3), ϕ_1 is the mode shape of the first mode given by Equation (1.3.4), H is the height of the building, and SD(T_1, ζ_1) is the DRS for period T_1 and damping ratio ζ_1.

It is assumed in Equation (2.4.1) that the response of the N-story shear building is dominated by the first mode and the maximum story drift occurs in the 1st story of the building between the 1st floor slab and the ground. Substituting Equation (1.3.3), (1.3.4), and (1.3.17) into Equation (2.4.1) yields

$$D(T_1,\zeta_1) = \frac{4}{\pi}\sin\left(\frac{\pi}{20T_1}\right)SD(T_1,\zeta_1). \tag{2.4.2}$$

The computation of the SDS involves two steps: (1) computing the DRS for a given earthquake ground motion and (2) converting the DRS to SDS according to Equation (2.4.2).

Figure 2.4.1 plots the SDS of the PS uncontrolled and controlled by the OCS, AID, and AVS algorithms. One can see that in the uncontrolled cases, two resonance peaks rise at 1 second and 2 seconds in the ELC case, and a resonance peak occurs at 1.5 seconds in the RRS case. In all controlled cases, these resonance peaks are significantly suppressed. In particular, a flat and smooth trend is observed over a wide period range in the OCS case. Gentle resonance peaks are found in the AID and AVS cases, but far less spiky as in the uncontrolled case. The maximum story drifts are all below 1 cm and 4 cm in the ELC and RRS cases, respectively.

Figure 2.4.2 presents the SDS of the AS for the OCS algorithm. The plots for the AID and AVS algorithms are omitted as the dynamics of the AS are neglected in these algorithms. It is seen that the SDS of the AS are in similar shape as those of the PS, but are relatively smaller at both the short and long period ranges. The maximum story drifts of the AS, 1.4 cm and 5 cm in the ELC and RRS cases respectively, occur around 2 seconds.

2.4.2 Dynamics of the AS

This subsection studies how the dynamics of the AS affects the response of the PS for the OCS algorithm from the SDS of the PS for various mass, damping, and stiffness values of the AS. No results are carried out for the AID and AVS algorithms because in these algorithms the dynamics of the AS are neglected.

Table 2.4.1 groups the range of parameters under investigation. In each set of the parametric analyses, only the effect of one parameter, denoted by x, is examined while the rest retain their nominal values. The nominal values for the mass, damping, and stiffness of the AS are related to those of the PS by

$$\alpha = 4\%, \ \beta = 1, \ \text{and} \ \gamma = 2. \tag{2.4.3}$$

Table 2.4.1: Sequence of analyses and nominal values of related parameters

Analysis	α	β	γ
1	x	1	2
2	4%	x	2
3	4%	1	x

Analysis 1: Effect of mass ratio of the AS: α = 1%, 2%, 4%, and 10%.
Analysis 2: Effect of damping ratio of the AS: β = 1, 5, 10, and 20.
Analysis 3: Effect of stiffness ratio of the AS: γ = 1, 2, 4, and 10.

Response of the PS

Figures 2.4.3 and 2.4.4 illustrate the effects of the mass, damping and stiffness of the AS on the PS. A decreasing trend is generally observed in the response of the PS as the mass of the AS decreases. Physically, a smaller mass corresponds to a higher frequency and hence provides the AS more opportunities to withdraw vibrational energy from the PS. This result agrees with Equation (2.2.11) which is obtained from an idealized harmonically forced vibration. Equation (2.2.11) asserts that a smaller mass ratio, α, leads to a larger E_n, i.e., the vibrational energy withdrawn from the PS to the AS in the first n cycles of motion, and thus yields a smaller response of the PS. A pronounced peak at 2 seconds is seen in Figure 2.4.4 (a), indicating the resonance of the PS with the RRS excitation. This is because for the parameters chosen in this case, the motion of the AS is not fast enough to catch up with the rapid movement of the PS. In the long period range, the mass of the AS does not seem to have an obvious effect on the response of the PS.

As seen in Equation (2.1.4), the motion of the AS directly affects the amount of the control force that the AS applies to the PS at attachments: the larger the displacement of the AS, the larger the control force, and the better the control effect. Therefore, adding damping to the AS in general is not favorable in AIC because a large amount of damping attenuates the motion of the AS. This is exactly what happens in Figures 2.4.3 (b) and 2.4.4 (b), where the response of the PS ascends as a result of the increasing damping ratio of the AS. This is also because the highly damped AS is no longer able to oscillate back to its opposite position quickly enough to initiate an attachment to the PS when needed.

Equation (2.2.11) states that the amount of vibrational energy withdrawn from the PS to the AS increases linearly with the increase of the stiffness of the AS, k_2. Thus, larger stiffness of the AS will reduce the response of the PS. As might then be expected, Figures 2.4.3 (c) and 2.4.4 (c) show a dramatic decrease of the response of the PS for larger stiffness of the AS, especially in the period range from 0.5 to 5 seconds. It is also seen from these figures that the response of the PS is less sensitive to the stiffness of the AS in both the short and long period ranges.

Response of the AS

Figures 2.4.5 and 2.4.6 show the SDS of the AS for different mass, damping and stiffness ratios of the AS. As seen in the previous section, the response of the AS resembles that of the PS due to the frequent attachment between the PS and the AS. Therefore, the change of the mass and stiffness of the AS should have comparable effects on the response of the AS. Confirmed in Figures 2.4.5 (a), (c) and 2.4.6 (a), (c), a smaller mass and a larger stiffness of the AS correspond to a smaller response of the AS. However, a large damping in the AS reduces the response of the AS, as shown in Figures 2.4.5 (b) and 2.4.6 (b).

Summary

Table 2.4.2 summarizes the influences of mass, damping, and stiffness of the AS on the responses of the PS and AS.

Table 2.4.2: Effects of the mass, damping, and stiffness of the AS on the PS and AS responses (⇑ - increasing, ⇓ - decreasing)

	⇑α	⇑β	⇑γ
PS Response	⇑	⇑	⇓
AS Response	⇑	⇓	⇓

2.4.3 Elasto-Plastic Behavior of the AS

In the previous sections, the deformation and stress of the AS are assumed to be within elastic limits. However, as the external excitation becomes stronger and the number of attachments between the PS and AS increases, the vibrational energy transferred from the PS to the AS may become sufficiently large that the displacement of the AS reaches its elastic limit and the AS begins to yield.

How the effect of elasto-plastic response of the AS affects the response of the AIC system is the topic of this subsection. This is examined by computing and plotting the displacement response of the PS and AS for different elastic limits of the AS, which are set at approximately one half (case I) and one quarter (case II) of the peak displacements of the purely elastic AS excited by the ELC and RRS ground motions (see Table 2.4.3). The material property of the AS is assumed to be elasto-plastic (bilinear). Figures 2.4.7 and 2.4.8 display the displacement responses of the PS and AS for the cases that the AS is purely elastic and elasto-plastic. Table 2.4.4 lists the peak displacements of the PS in Figures 2.4.7 and 2.4.8.

Table 2.4.3: Peak displacement of the purely elastic AS excited by the ELC and RRS ground motion, and elastic limits of the elasto-plastic AS chosen in the two case studies

	Peak Displacement (Elastic)	Elastic Limit (case I)	Elastic Limit (case II)
ELC	5.36 cm	2 cm	1 cm
RRS	12.78 cm	6 cm	3 cm

Table 2.4.4: Peak displacements of the PS corresponding to the cases in Table 2.4.3

	Peak Displacement (Elastic)	Peak Displacement (case I)	Peak Displacement (case II)
ELC	3.66 cm	2.01 cm	3.22 cm
RRS	7.15 cm	9.89 cm	9.24 cm

It is seen that in both cases I and II, the responses of the PS are only slightly degraded. The response of the AS is mostly within the response envelop of the purely elastic AS. Hence, an elasto-plastic AS can provide approximately the same control efficiency as a purely elastic AS does as long as the yielded AS can still provide sufficient control force on the PS. This feature greatly relaxes the requirement on the stiffness of AS and enhances the applicability of the AIC system in practice.

2.5 Practical Issues

2.5.1 Sampling Interval

The length of the sampling interval in a control system directly affects the system performance. On one hand, too large a sampling interval introduces excessive error in data acquisition and deteriorates the system performance. On the other hand, an overly fine sampling interval places extraordinary requirements on costly data acquisition systems and computer equipment. Hence, a proper sampling interval should be an appropriate balance between these two extremes.

In an AIC system, all 'control actions' happen at the instants when the PS and AS are attached or detached. In the OCS algorithm, the attachment occurs as soon as the detached PS and AS reach the same velocity, and the detachment occurs as soon as the velocity of the attached PS and AS drops to zero, i.e., the displacement peak is reached. Because the motion of the detached AS is much more rapid than that of the PS or the attached PS and AS, the velocity difference between the PS and AS at attachment, or the impact velocity, should be the major focus in examining the effect of the sampling interval.

In the AID and AVS algorithms, the dynamics of the AS are neglected and the velocity (relative to the ground) of the AS is assumed to be zero when it is attached to the PS. The impact velocity is therefore the velocity of the PS, which is much smaller in com-

parison to that of the AS at attachment in the OCS algorithm. Therefore, only the OCS algorithm is considered in the following discussion on impact velocity.

Impact Velocity

Consider the PS and AS immediately after a detachment, where the detached PS and AS begin to separate from the displacement peaks they just reached. With the appropriate choice of time origin, the displacement and velocity of the PS and AS may be approximated by two harmonic functions

$$x_1(t) = A\cos(\omega_1 t), \quad v_1(t) = \dot{x}_1(t) = -A\omega_1 \sin(\omega_1 t) \tag{2.5.1}$$

$$x_2(t) = B\cos(\omega_2 t), \quad v_2(t) = \dot{x}_2(t) = -B\omega_2 \sin(\omega_2 t) \tag{2.5.2}$$

where A and B denote the peak displacements of the PS and AS of the current cycle of motion, respectively.

Since the frequency of the AS is much higher than the predominant frequency of the external excitations, the detached AS will vibrate in a somewhat harmonic motion in its own natural frequency, as seen in Figures 2.3.5 and 2.3.6. Thus, Equation (2.5.1) reasonably describes the motion of the detached AS. Equation (2.5.2) is only an approximation of the slower motion of the detached PS. However, such an approximation is justifiable by the fact that our main focus now is on the much more rapid motion of detached AS.

In the OCS algorithm, an attachment between the PS and AS will be initiated when the detached PS and AS reach the same velocity, say at time t_1, i.e.,

$$v_1(t_1) = -A\omega_1 \sin(\omega_1 t_1) = v_2(t_1) = -B\omega_2 \sin(\omega_2 t_1)\,. \tag{2.5.3}$$

In an AIC system where the state variables of the PS and AS are measured at each discrete sampling interval, the velocities of the PS and AS are considered the same as soon as the following condition is satisfied:

$$[\dot{x}_1(t) - \dot{x}_2(t)][\dot{x}_1(t-\Delta t) - \dot{x}_2(t-\Delta t)] \le 0. \tag{2.5.4}$$

Therefore, the attachment between the PS and AS will be realized at time t_2, the beginning of the first sampling interval after t_1. Obviously, the velocities of the PS and AS at

time t_2 will no longer be the same. In the worst-case scenario, the impact would occur when $t_2 = t_1 + \Delta t$. Therefore, the maximum impact velocity can be written as

$$\begin{aligned}\Delta v &= \left|v_1(t_2) - v_2(t_2)\right| = \left|v_1(t_1+\Delta t) - v_2(t_1+\Delta t)\right| \\ &= \left|-A\omega_1 \sin[\omega_1(t_1+\Delta t)] + B\omega_2 \sin[\omega_2(t_1+\Delta t)]\right| \\ &= \left|\begin{array}{l} -A\omega_1 \sin(\omega_1 t_1)\cos(\omega_1\Delta t) - A\omega_1 \cos(\omega_1 t_1)\sin(\omega_1\Delta t) + \\ +B\omega_2 \sin(\omega_2 t_1)\cos(\omega_2\Delta t) + B\omega_2 \cos(\omega_2 t_1)\sin(\omega_2\Delta t) \end{array}\right| \\ &= \left|\begin{array}{l} -v_1(t_1)\cos(\omega_1\Delta t) - A\omega_1 \cos(\omega_1 t_1)\sin(\omega_1\Delta t) + \\ +v_2(t_1)\cos(\omega_2\Delta t) + B\omega_2 \cos(\omega_2 t_1)\sin(\omega_2\Delta t) \end{array}\right|\end{aligned} \tag{2.5.5}$$

Since for small Δt

$$\cos(\omega_1\Delta t) \approx 1, \quad \cos(\omega_1\Delta t) \approx 1, \quad \sin(\omega_1\Delta t) \approx \omega_1\Delta t, \quad \sin(\omega_2\Delta t) \approx \omega_2\Delta t, \tag{2.5.6}$$

and $v_1(t_1) = v_2(t_1)$, Equation (2.5.5) can be simplified to

$$\Delta v = \left|-A\omega_1^2 \cos(\omega_1 t_1) + B\omega_1^2 \cos(\omega_2 t_1)\right|\Delta t\,. \tag{2.5.7}$$

Note that

$$\omega_1^2 << \omega_2^2. \tag{2.5.8}$$

Thus, Equation (2.5.8) is further reduced to

$$\Delta v \approx B\omega_1^2 \cos(\omega_2 t_1)\Delta t\,. \tag{2.5.9}$$

Now, it is clearly seen that the impact velocity, Δv, is proportional to the sampling interval, Δt, and the square of the natural frequency of the PS, ω_1^2.

Equation (2.5.9) may also be written as

$$\Delta v = \Delta v_2 \cos(\omega_2 t_1) \tag{2.5.10}$$

where

$$\Delta v_2 = B\omega_1^2 \Delta t\,. \tag{2.5.11}$$

Therefore, the impact velocity, Δv, is also proportional to the velocity change of the AS, Δv_2, during the sampling period between times t_1 and $t_1+\Delta t$.

Numerical Studies

The validity of Equation (2.5.9) is verified in Figure 2.5.1, which shows the impact velocity between the PS and AS verses the sampling interval for various period values of

the PS. One can see that the impact velocity does increase nearly linearly with sampling interval. Also, a smaller period of the PS, i.e., a larger frequency, corresponds to a larger impact velocity.

The basis of AIC concept is to reduce the response of the PS by actively transferring vibrational energy from the PS to the AS through continuously controlled interactions. Dynamic impact between the PS and AS is not the original motivation for AIC, although the response of the PS can be reduced to some degree due to the energy loss during the impact. In contrast to this minor benefit, however, a bigger concern arises on whether such dynamic impact will damage the IE during the control process. The direct consequence of this issue is beyond the scope of this study. Nevertheless, Equation (2.5.9) and Figure 2.5.1 qualitatively reveal the connection between the sampling interval and the maximum impact velocity between the PS and AS.

The effect of sampling interval on system performance is further examined in Figures 2.5.2 and 2.5.3 where the SDS of the PS corresponding to different sampling intervals are computed and plotted for the OCS, AID, and AVS algorithms.

In the OCS algorithm, the effect of the sampling interval on the response of the PS is actually related to the period of the AS. As above mentioned, this is because the motion of the AS becomes more rapid when the period of the AS becomes smaller. Rapid motion in general needs finer sampling. One can see from Figures 2.5.2 and 2.5.3 that the response of the PS is sensitive to the sampling interval particularly in the short period range of the PS where the period of the AS is short. Better agreement in the response of the PS corresponding to different sampling intervals is found in the long period range of the PS where the period of the AS is longer. Recall that for fixed mass and stiffness ratios between the AS and PS, the periods of the PS and AS are proportional. The effect of sampling interval on the response of the PS correlates to the frequency components of the ground motion as well. For example, the response of the PS shows greater sensitivity to the sampling interval under the ELC ground motion than under the RRS ground motion.

In the AID and AVS algorithms, the difference between the responses of the PS corresponding to different sampling intervals is barely noticeable for sampling intervals less than 0.01 second. Such insensitivity to the sampling interval is mainly attributed to the fact that the dynamics of the AS are neglected in these two algorithms.

The sensitivity of an AIC algorithm to the sampling interval may be evaluated from the maximum allowable sampling interval for which story drift responses begin to converge. The smaller the maximum sampling interval is, the more sensitive the AIC algorithm is. Table 2.5.1 lists the maximum sampling intervals for the OCS, AID, and AVS algorithms. The responses for the cases examined in this subsection show little divergence for sampling intervals less than these maximum values.

Table 2.5.1: The maximum sampling intervals (in seconds) for the OCS, AID, and AVS algorithms under ELC and RRS excitations

Algorithm	OCS	AID	AVS
ELC	0.005	0.01	0.02
RRS	0.02	0.02	0.02

2.5.2 Time Delay

Time delay is one of the intrinsic problems in real-time active control. In the time domain, control forces are applied to the structure at a later moment after the control decision is made. In the frequency domain, control forces are applied to the different direction as the commanded one due to the time delay induced phase shift.

In an AIC system, time delays can arise from: 1) data acquisition, processing, and transmission, and 2) the time taken to close and open the valve in the IE for attachment and detachment. As technology advances, the time required for data acquisition, processing, and transmission will be shortened. But the mechanical reaction of the valve is unlikely to be reduced significantly.

Because AIC requires only simple attachment and detachment between the PS and AS instead of applying a control force of varying amplitude as in conventional active control techniques, the duration of the time delay in an AIC system remains almost constant throughout the control process. Hence, only the effect of time delays of constant duration is investigated in this study. It is further assumed that the length of time delay is a multiple of the sampling interval.

The effect of time delay on the AIC system is examined by computing the displacement response and the SDS of the PS corresponding to different lengths of time delay. These results are compared with the uncontrolled counterpart in Figures 2.5.4 to 2.5.7.

For the OCS case, it is seen that the system performance gradually deteriorates as the length of the time delay increases. But instability has not yet been observed in the AIC system for the range of parameters considered.

In contrast to the OCS algorithm, the performance of the PS for the AID case is far less sensitive to the time delay. The system remains stable in all cases with only minor degradation in the short period range. The deterioration of the system response in the long period range is barely noticeable.

However, time delay has tremendous impact on the response of the PS in the AVS case. Instability occurs as the length of the time delay exceeds a certain critical value. As shown in Figures 2.5.6 (c) and 2.5.7 (c), instability begins to take place at the periods of 0.3, 0.6, and 1 seconds when the time delays are 0.02, 0.04, and 0.08 seconds, respectively.

In the AVS algorithm, regardless of the motion of the AS, the attachment between the PS and AS are supposed to be initiated as the PS starts 'loading,' i.e., the absolute value of the displacement of the PS begins to get larger. However, due to time delay, the attachment between the PS and AS may be delayed until the PS starts 'unloading.' As a result, energy is added instead of subtracted from the PS by the AS at attachment. Resonance is therefore gradually built up in the system and eventually leads to instability.

The robustness of an AIC algorithm with respect to time delay may be evaluated from the critical time delay - the shortest time delay for which the system starts to become unstable. Table 2.5.2 summaries the critical time delays in the OCS, AID, and AVS algorithms for the SDOF system with a 1 second period. Table 2.5.3 gives the general qualitative performance assessments for these control algorithms in the presence of time delays.

Table 2.5.2: Critical time delays (in seconds) in the OCS, AID, and AVS algorithms

Algorithm	OCS	AID	AVS
ELC	0.08	> 0.08	0.08
RRS	0.08	> 0.08	0.08

Table 2.5.3: Qualitative assessments of the robustness of the OCS, AID, and AVS algorithms in the presence of time delays

Algorithm	OCS	AID	AVS
ELC	Deteriorated	Robust	Severely Deteriorated
RRS	Deteriorated	Robust	Severely Deteriorated

2.5.3 Time Delay Compensation

Time Delay Compensation Scheme

Appropriate time delay compensation schemes rely on the nature of the time delay in the system. In general, the governing equation of a time delayed control system changes to a differential-difference equation from an ordinary differential equation. In the time domain, a Taylor expansion gives the most direct approximation of the differential-difference equation and the control decision can be made based on the response of the approximated system. However, this approach requires that the time delay is sufficiently small. Otherwise the approximation error could cause dynamic instability. Time delay

induced phase shift may also be compensated in the frequency domain. This approach is most effective when the system response is dominated by only a few participating modes.

The discrete system equation (2.1.9) has been idealized for the case where the attachment between the PS and AS can be made instantaneously as state variables are measured and control decisions are made. In the presence of a time delay, denoted by $j\Delta t$, the control decision made at time $i\Delta t$ is instead implemented at a later time $(i+j)\Delta t$.

With the above in view, a simple predictive time delay compensation scheme is proposed in this study. The essence of this scheme is to make the control decision for time $(i+j)\Delta t$ in advance at time $i\Delta t$. The system response from time $(i+1)\Delta t$ to time $(i+j)\Delta t$ are predicted step by step based on the measured system response at time $i\Delta t$. The detailed operations of this scheme at time $i\Delta t$ are described as follows:

1. Assemble the system matrix A_i and control force vector H_i.
2. Estimate the system response at time $(i+1)\Delta t$ according to Equation (2.1.9), i.e.,

$$Y_{i+1} = P_i Y_i + Q_i + R_i$$

where

$$P_i = e^{A_i \Delta t}, \quad Q_i = A_i^{-1}(P_i - I)B_i, \quad R_i = A_i^{-1}(P_i - I)H_i.$$

3. Make control decision for time $(i+1)\Delta t$. Note that this control decision is used for prediction only and will not be physically executed.
4. Repeat step 1 for $i = i+1$ until the control decision for time $(i+j)\Delta t$ is reached.
5. Command the control decision for time $(i+j)\Delta t$.

It should be noted that the external excitation $B(t)$ from time $(i+1)\Delta t$ to time $(i+j)\Delta t$ is not known at time $i\Delta t$ beforehand, it is therefore assumed that

$$B_{i+l} = \begin{Bmatrix} \Phi \\ La_{i+l} \end{Bmatrix} = B_i = \begin{Bmatrix} \Phi \\ La_i \end{Bmatrix}, \quad l \in [1, j] \tag{2.5.12}$$

where B_i is the external excitation at time $i\Delta t$.

Numerical Results

Figures 2.5.8 (a) and 2.5.9 (a) plot the compensated time history responses of the PS for the OCS algorithm. It is seen that the compensated responses of the PS are much improved from those with the presence of time delay. However, deterioration can still be seen in the compensated response as compared to those with the absence of time delay. In particular, the predictive scheme is very effective in compensating the time delays of 0.02 and 0.04 seconds, as shown in Figure 2.5.9 (a).

Figures 2.5.10 (a) and 2.5.11 (a) display the compensated SDS for the OCS algorithm. In the long period range, apparent enhancement of the compensated response is generally observed. However, in the short period range, instability arises in Figure 2.5.10 (a) as the length of time delay exceeds 0.08 second. Overall, the proposed predictive scheme is very effective in compensating time delays below 0.04 second for the OCS algorithm.

As shown in the preceding section, the AID algorithm is insensitive to the time delay and there is no real need of time delay compensation in such case. Nevertheless, Figures 2.5.8 (b) to 2.5.11 (b) show the compensated time history response and SDS of the PS for the AID algorithm. It is seen that the compensated response exhibit no prominent improvement over those with the presence of time delay. Degradation and instability are instead observed in most of the compensated cases.

Finally, Figures 2.5.8 (c) to 2.5.11 (c) demonstrate the efficiency of the proposed time compensation scheme in overcoming the time delay effect for the AVS algorithm. The compensated responses almost match those without time delay, indicating that the time delays in the AVS algorithm have been fully compensated.

Summary

The effectiveness of the predictive scheme on an AIC algorithm may be evaluated from the longest time delay that the predictive scheme effectively compensates. Table 2.5.4 summaries the longest time delays effectively compensated by the predictive scheme in the OCS, AID, and AVS algorithms for the SDOF system with a 1 second

period. Table 2.5.5 gives the general qualitative performance assessments of the compensation effectiveness of the predictive scheme on the AIC algorithms in the presence of time delays.

Table 2.5.4: Longest time delays (in seconds) compensated by the predictive scheme in the OCS, AID, and AVS algorithms

Algorithm	OCS	AID	AVS
ELC	0.04	0.04	> 0.08
RRS	0.04	0.04	> 0.08

Table 2.5.5: Qualitative assessments of the compensation effectiveness of the predictive scheme on the OCS, AID, and AVS algorithms

Algorithm	OCS	AID	AVS
ELC	Good	Good	Excellent
RRS	Good	Good	Excellent

2.6 Conclusions

This chapter carries out a comprehensive study on the response of SDOF AIC systems under earthquake ground motions. Based on the analytical and numerical results obtained in the preceding sections, the following conclusions are drawn:

1. All AIC algorithms lead to significantly reduced displacement, velocity, and acceleration responses of the PS as compared to the uncontrolled counterpart. Of the three algorithms employed in this study, the OCS algorithm produces the most efficient energy withdrawal from the PS to the AS and gives the best overall control results.
2. Aiming at withdrawing vibrational energy from the PS to the AS during the control process, all AIC algorithms are inherently stable.
3. The mass, damping, and stiffness in the AS have a pronounced effect on the response of the PS. An AS with a smaller mass, a smaller damping, and a larger stiffness in

general is more effective in controlling the response of the PS. However, in the AID algorithm, drifting occurs in the response of the PS when the stiffness of the AS is more than twice that of the PS (see Figures 2.3.11 and 2.3.12).

4. An elasto-plastic AS can provide approximately the same control efficiency as a purely elastic AS does as long as the yielded AS can still provide sufficient control force on the PS. This feature greatly relaxes the requirement on the stiffness of AS and enhances the applicability of AIC system in practice.

5. In an AIC system, the proper length of the sampling interval depends on the frequency of the AS. In the OCS algorithm, a finer sampling interval is generally needed when the period of the AS is shorter and the motion of the AS becomes more rapid. However, the AID and AVS algorithms are much less sensitive to the sampling interval because the dynamics of the AS are neglected. The impact velocity between the PS and AS is proportional to the length of the sampling interval and the square of the frequency of the PS.

6. Deteriorated but stable response of the PS is generally observed as the time delay gets longer in the OCS algorithm. The AID algorithm is robust with respect to the time delay. Instability often occurs in the AVS algorithm.

7. The predictive time delay compensation scheme presented is effective for compensating short time delays in the OCS algorithm, and very effective in compensating for long time delays in the AVS algorithm. It is, however, not effective in compensating the time delay in the AID algorithm but there is no need for compensation in this case.

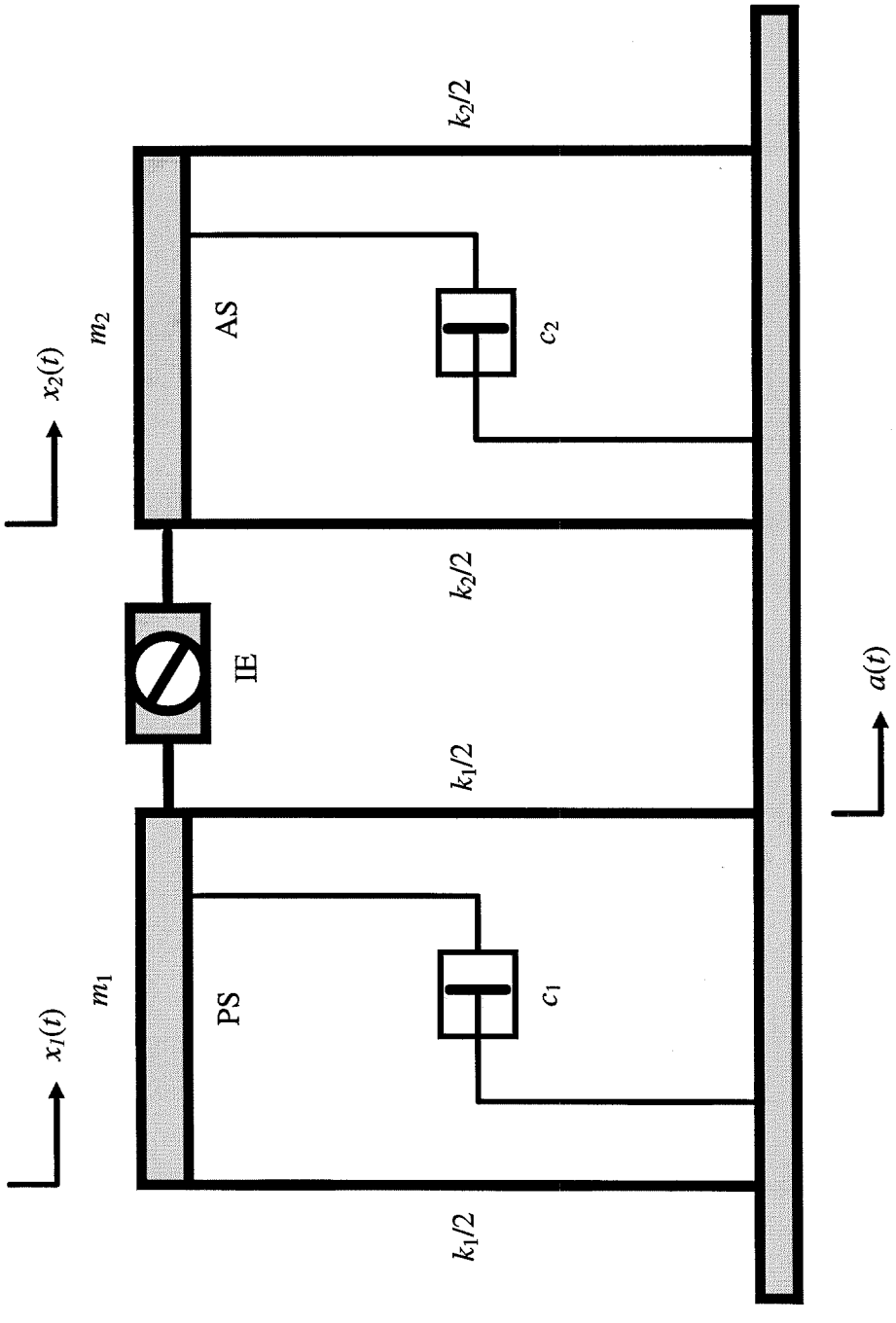

Figure 2.1.1: Schematic representation of a SDOF AIC system

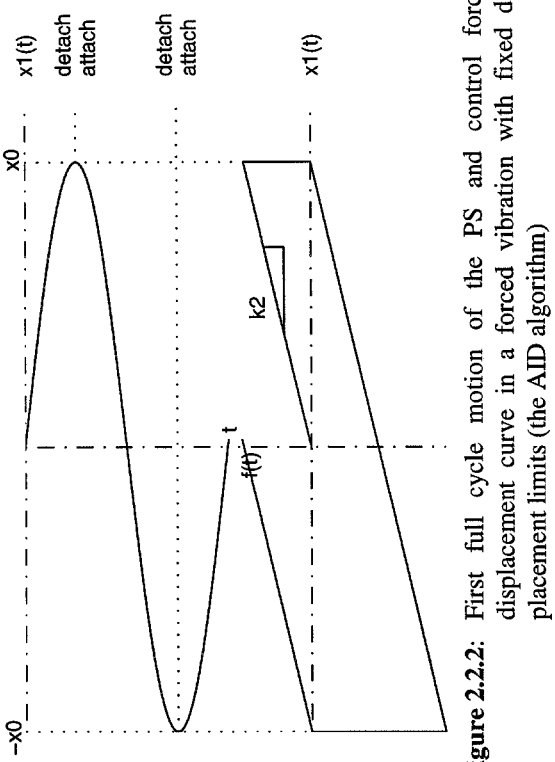

Figure 2.2.2: First full cycle motion of the PS and control force-displacement curve in a forced vibration with fixed displacement limits (the AID algorithm)

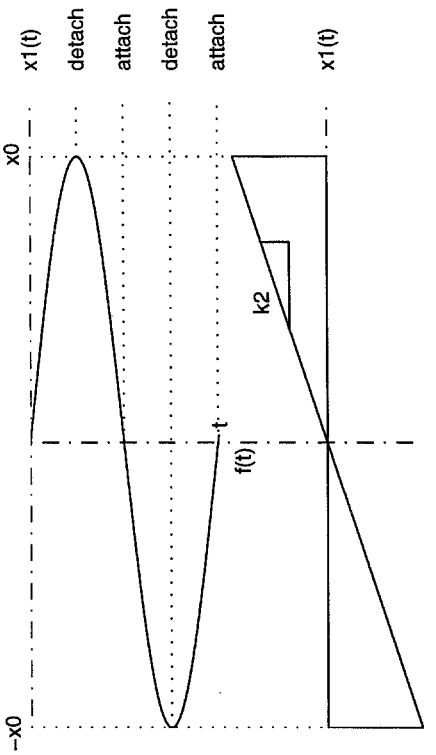

Figure 2.2.3: First full cycle motion of the PS and control force-displacement curve in a forced vibration with fixed displacement limits (the AVS algorithm)

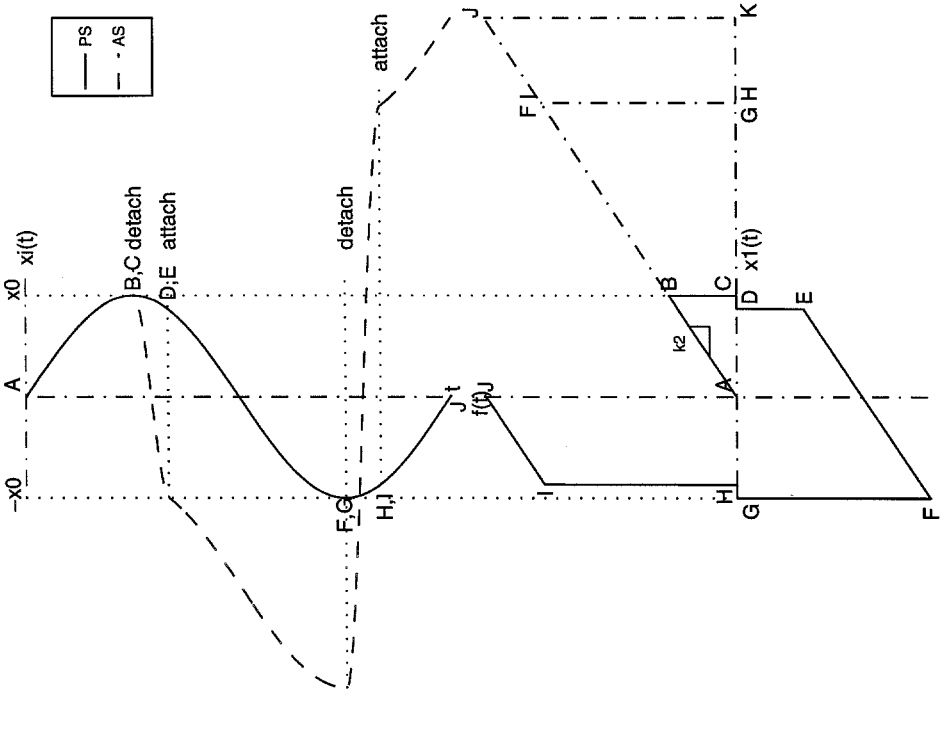

Figure 2.2.1: First full cycle motion of the PS and AS and control force-displacement curve in a forced vibration with fixed displacement limits (the proposed algorithm)

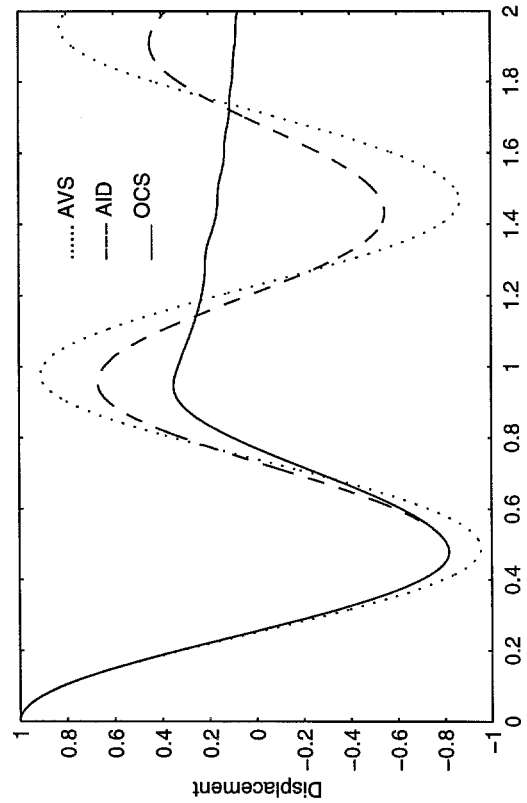

Figure 2.2.4: Response of the PS in a free vibration (OCS)

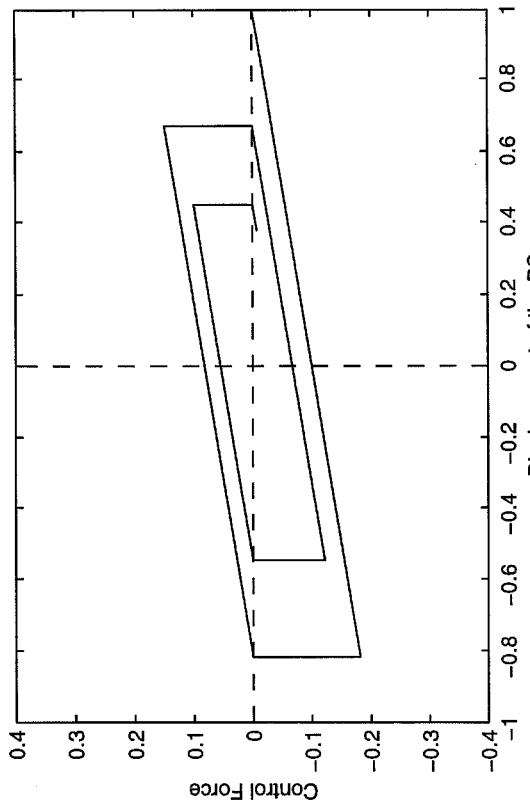

Figure 2.2.5: Control force-displacement curve in a free vibration (OCS)

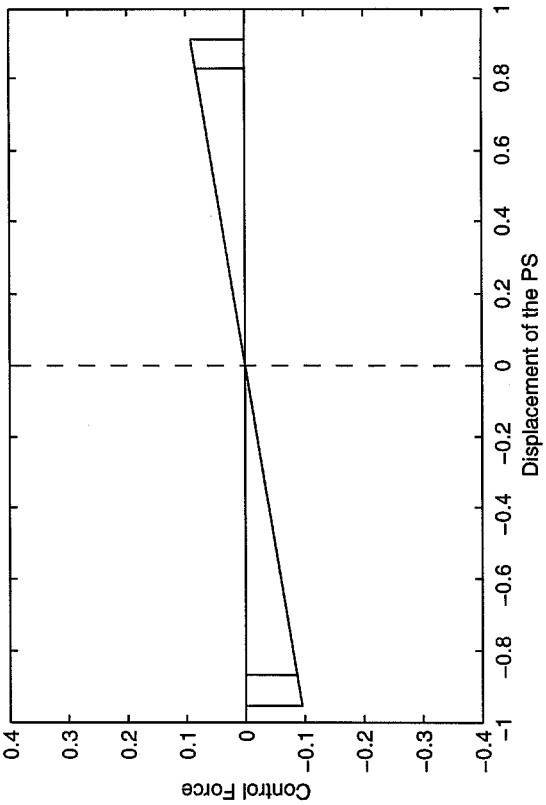

Figure 2.2.6: Control force-displacement curve in a free vibration (AID)

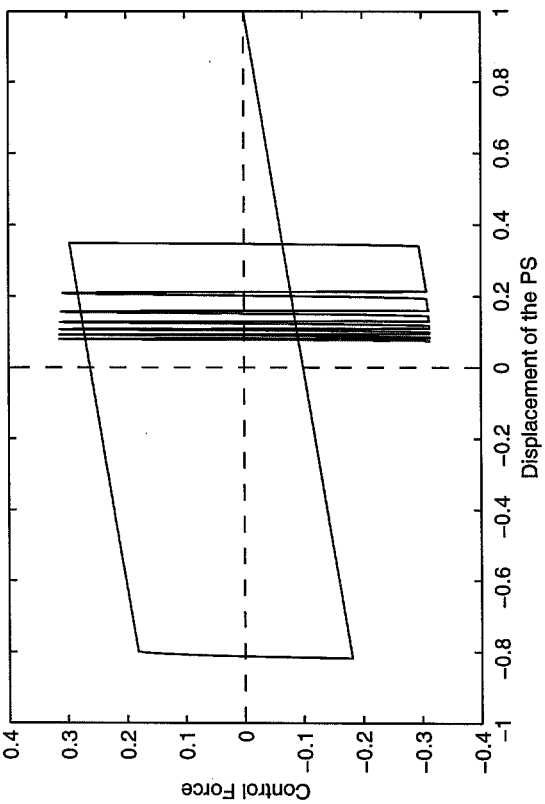

Figure 2.2.7: Control force-displacement curve in a free vibration (AVS)

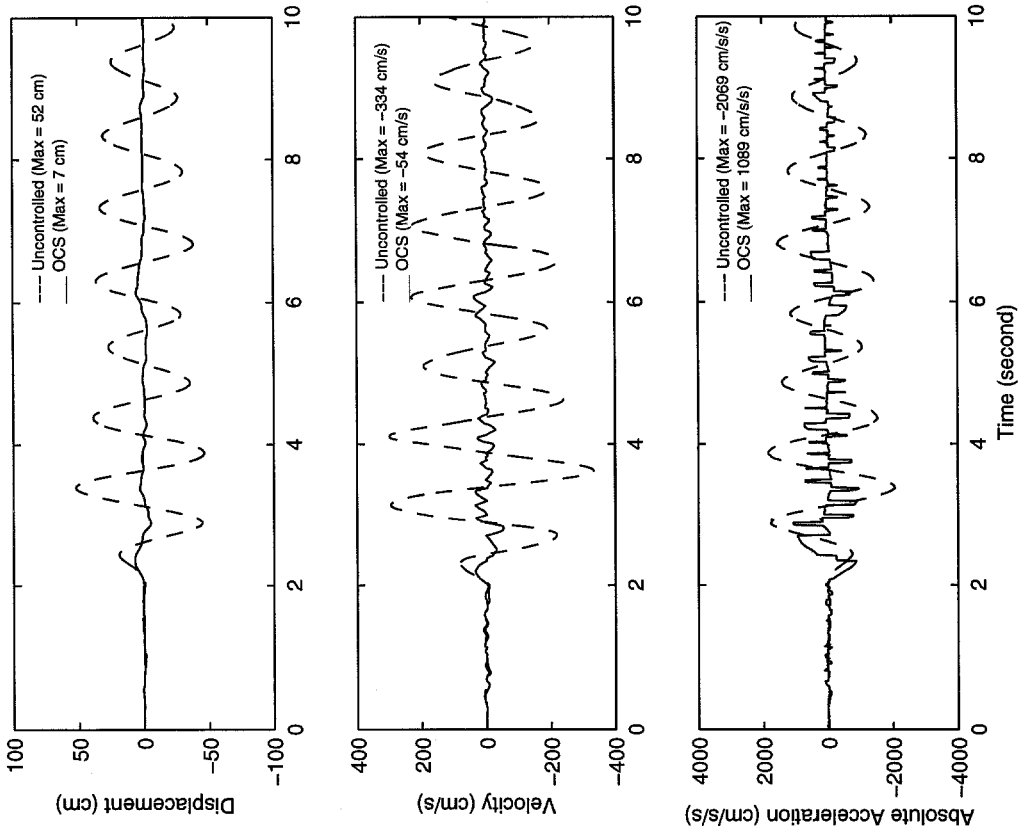

Figure 2.3.2: Displacement, velocity, and acceleration time history responses of the PS controlled by the OCS algorithm and excited by the RRS ground motion

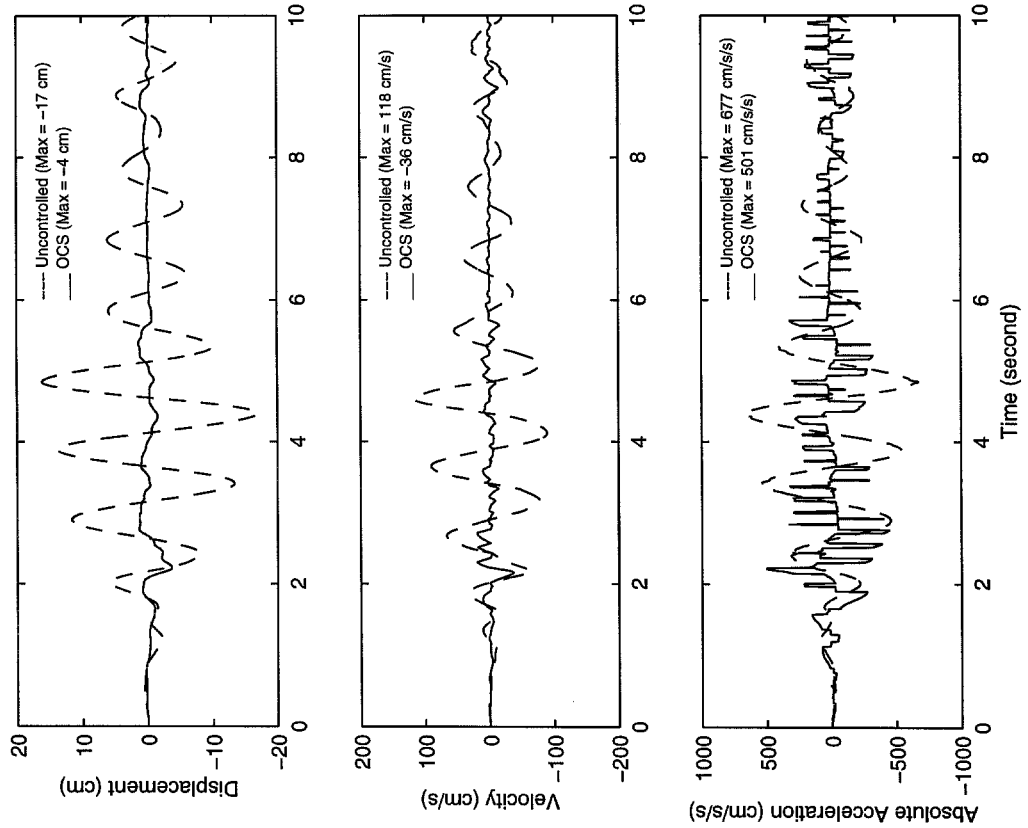

Figure 2.3.1: Displacement, velocity, and acceleration time history responses of the PS controlled by the OCS algorithm and excited by the ELC ground motion

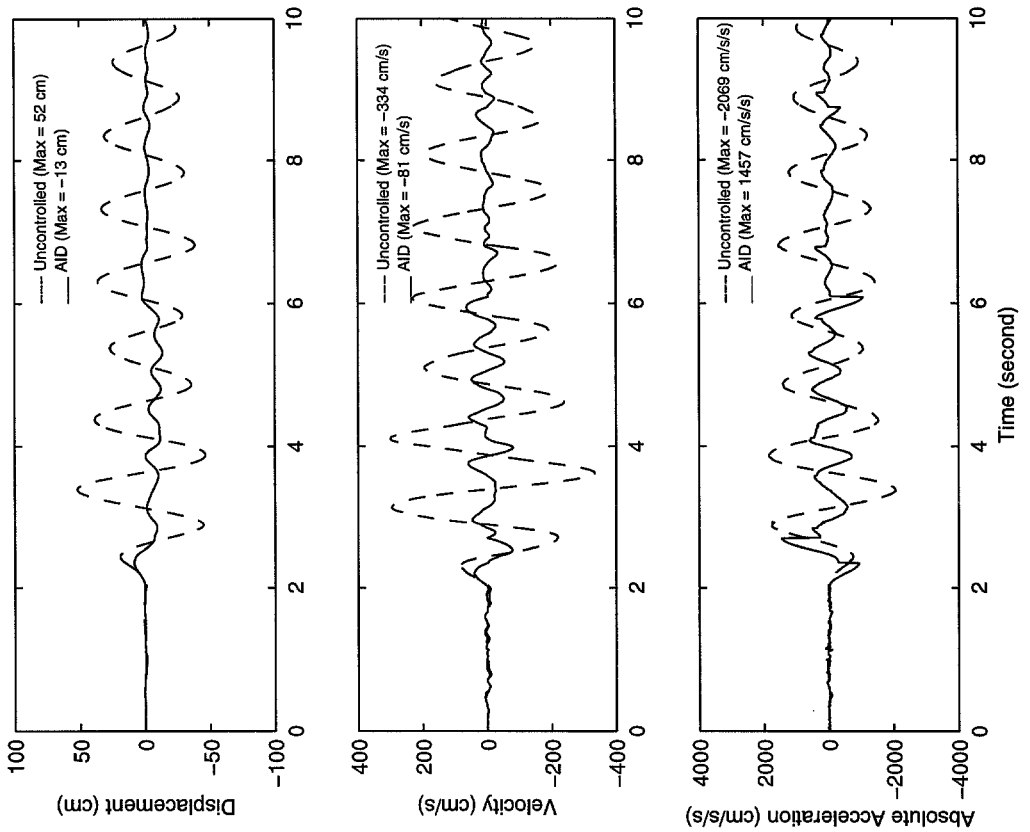

Figure 2.3.4: Displacement, velocity, and acceleration time history responses of the PS controlled by the AID algorithm and excited by the RRS ground motion

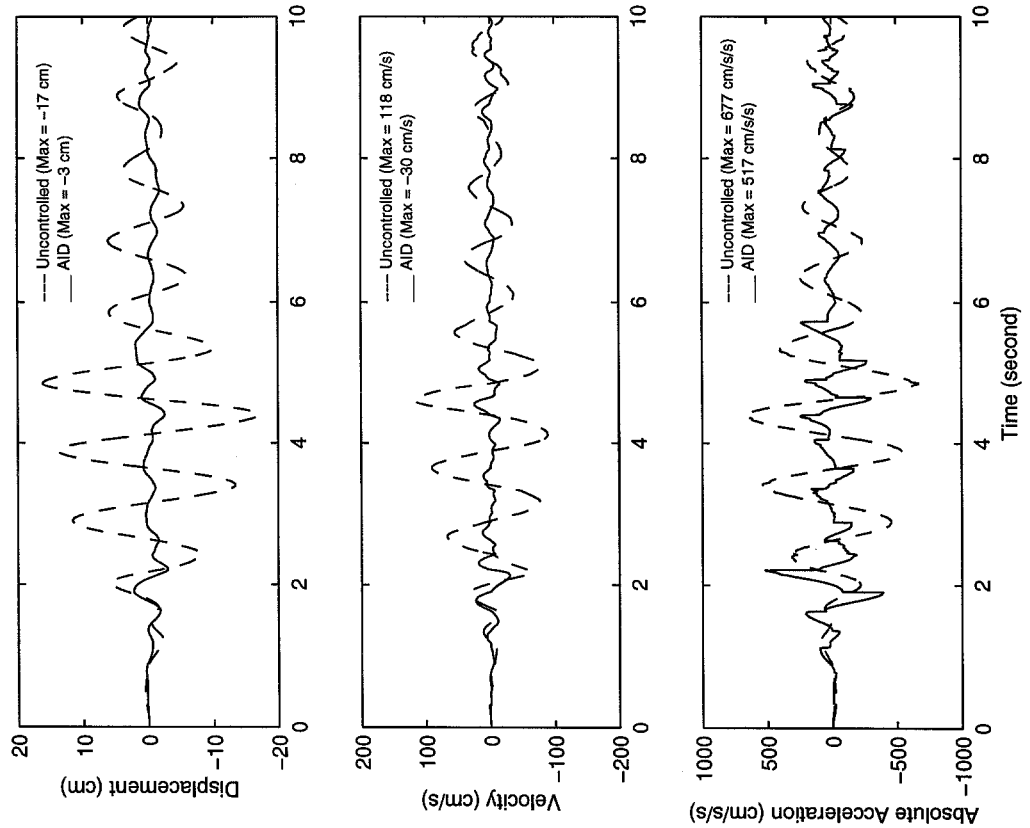

Figure 2.3.3: Displacement, velocity, and acceleration time history responses of the PS controlled by the AID algorithm and excited by the ELC ground motion

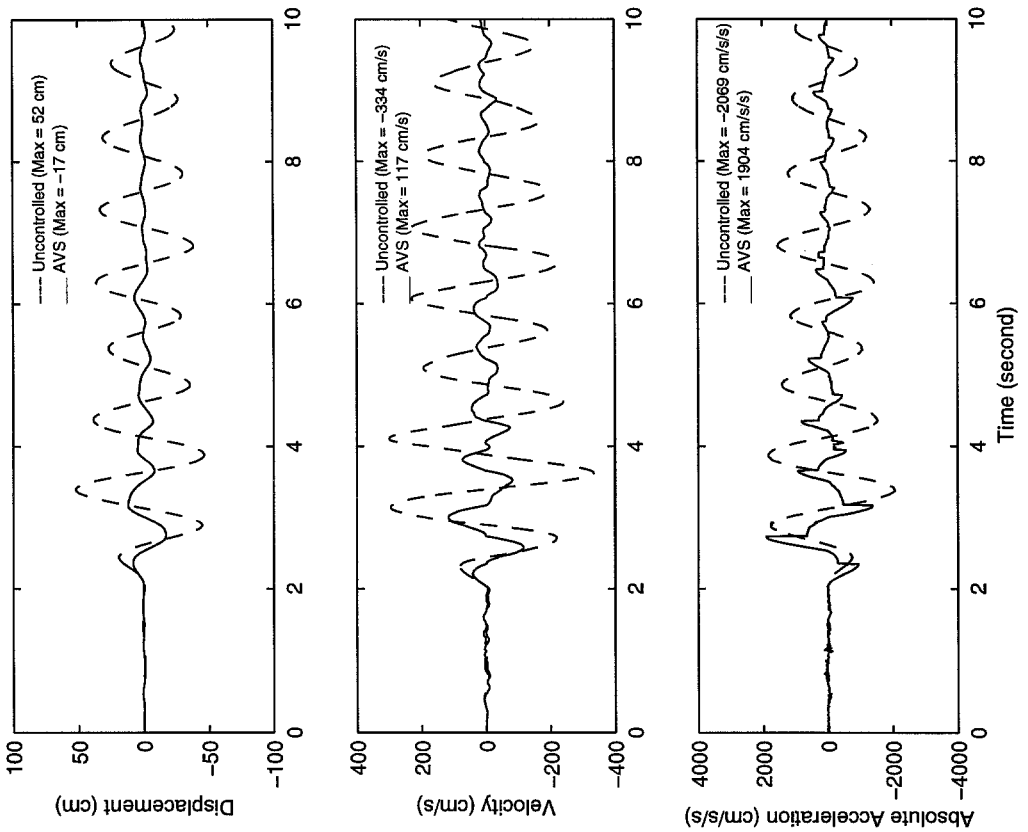

Figure 2.3.6: Displacement, velocity, and acceleration time history responses of the PS controlled by the AVS algorithm and excited by the RRS ground motion

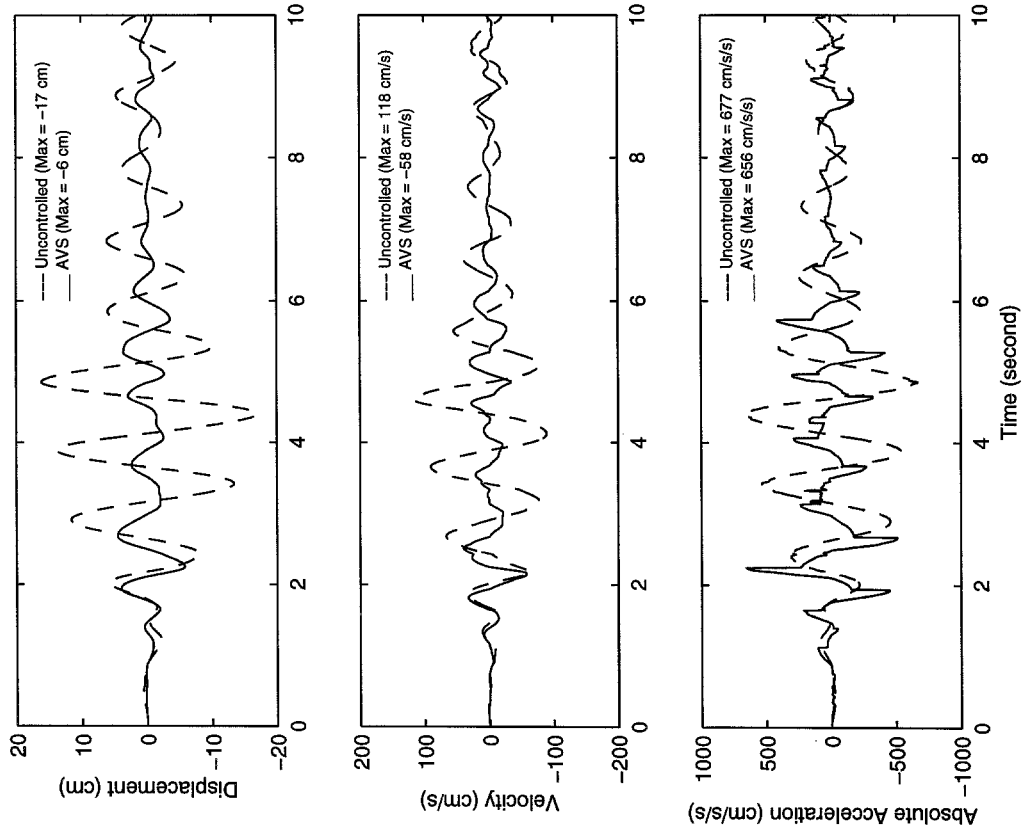

Figure 2.3.5: Displacement, velocity, and acceleration time history responses of the PS controlled by the AVS algorithm and excited by the ELC ground motion

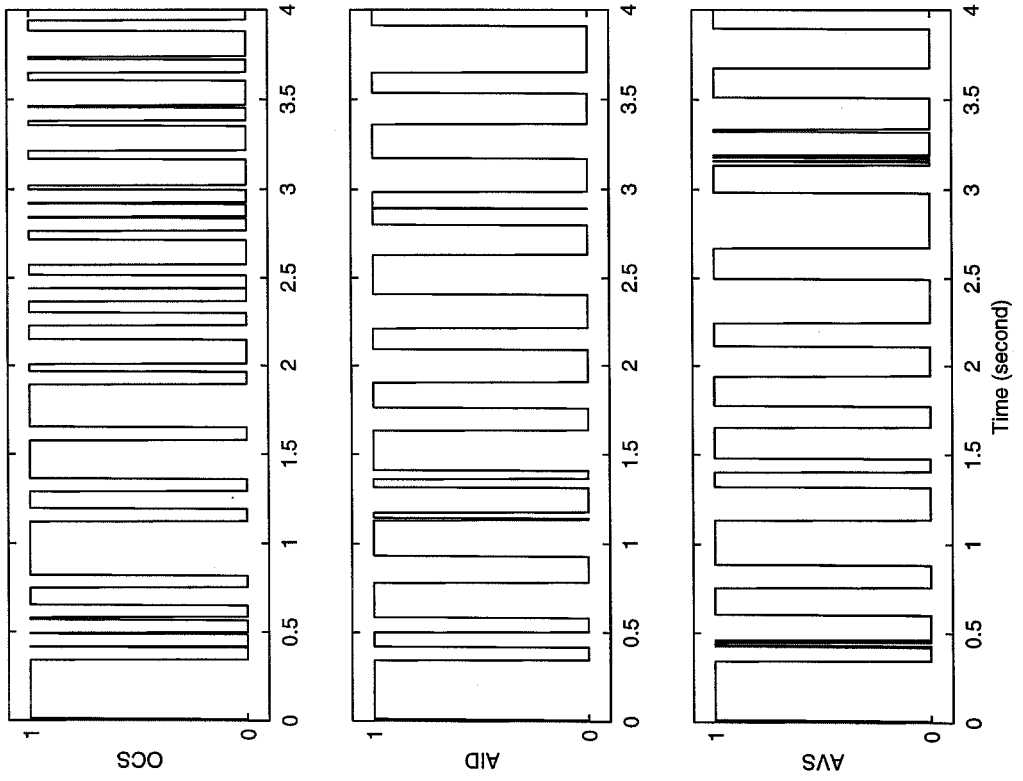

Figure 2.3.7: Attachment time histories controlled by the OCS, AID and AVS algorithms and excited by the ELC ground motion (1 - attachment and 0 - detachment)

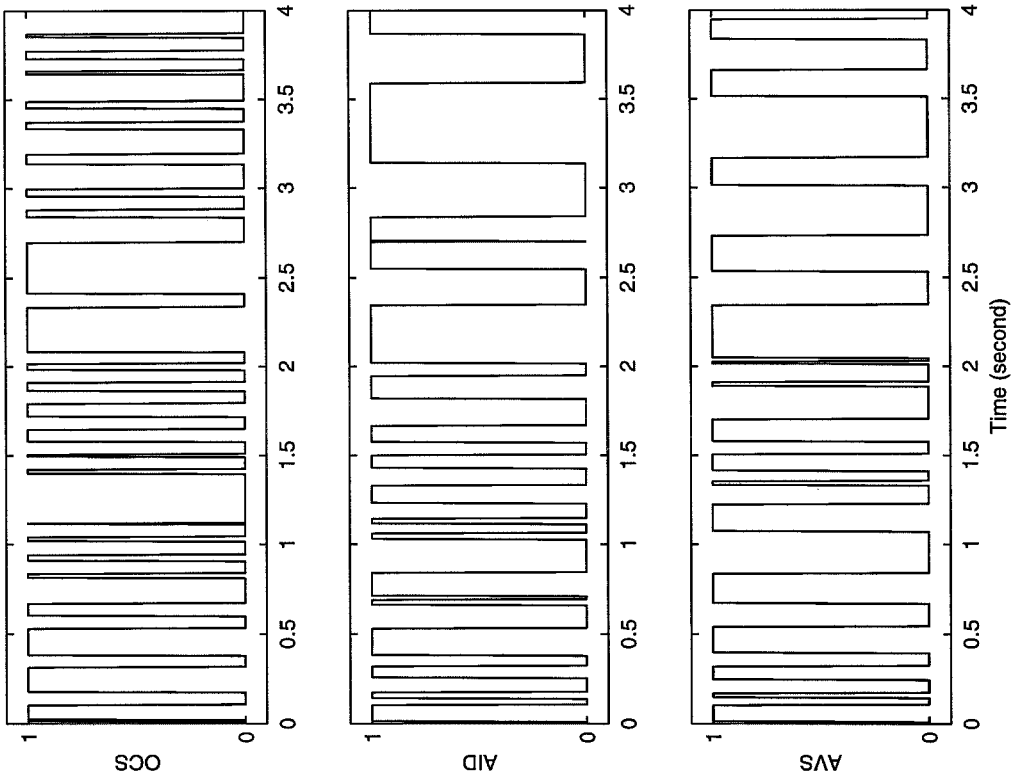

Figure 2.3.8: Attachment time histories controlled by the OCS, AID and AVS algorithms and excited by the RRS ground motion (1 - attachment and 0 - detachment)

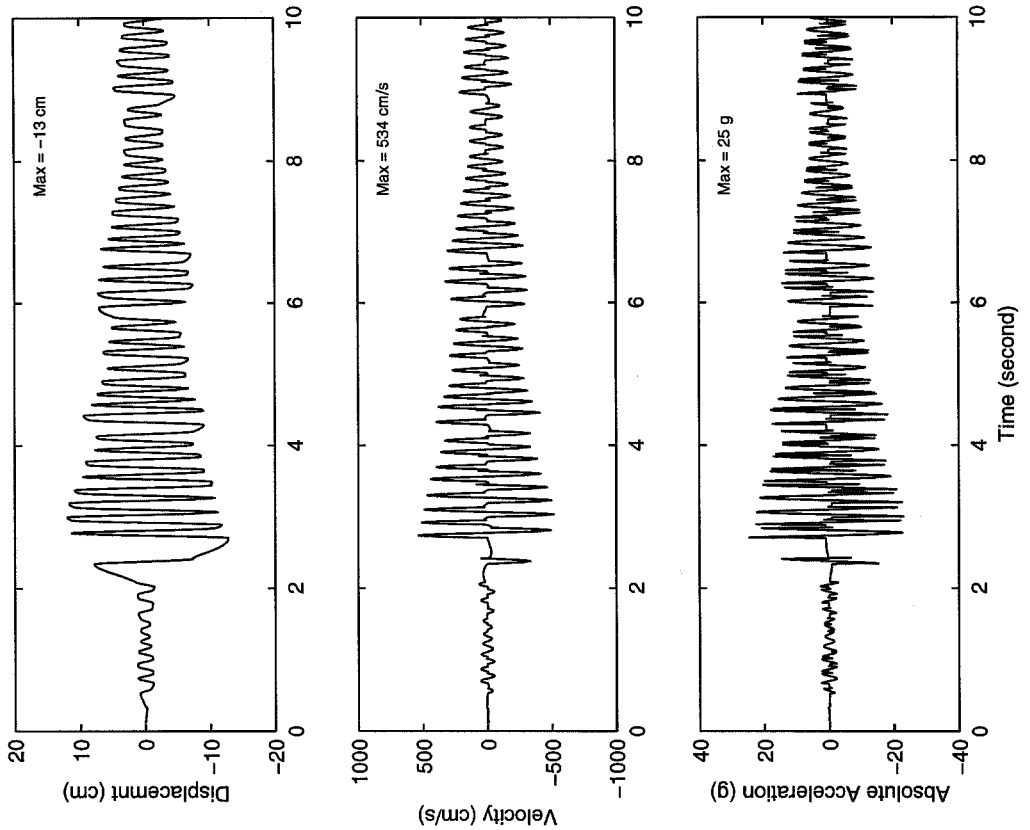

Figure 2.3.10: Displacement, velocity, and acceleration time history responses of the AS controlled by the OCS algorithm and excited by the RRS ground motion

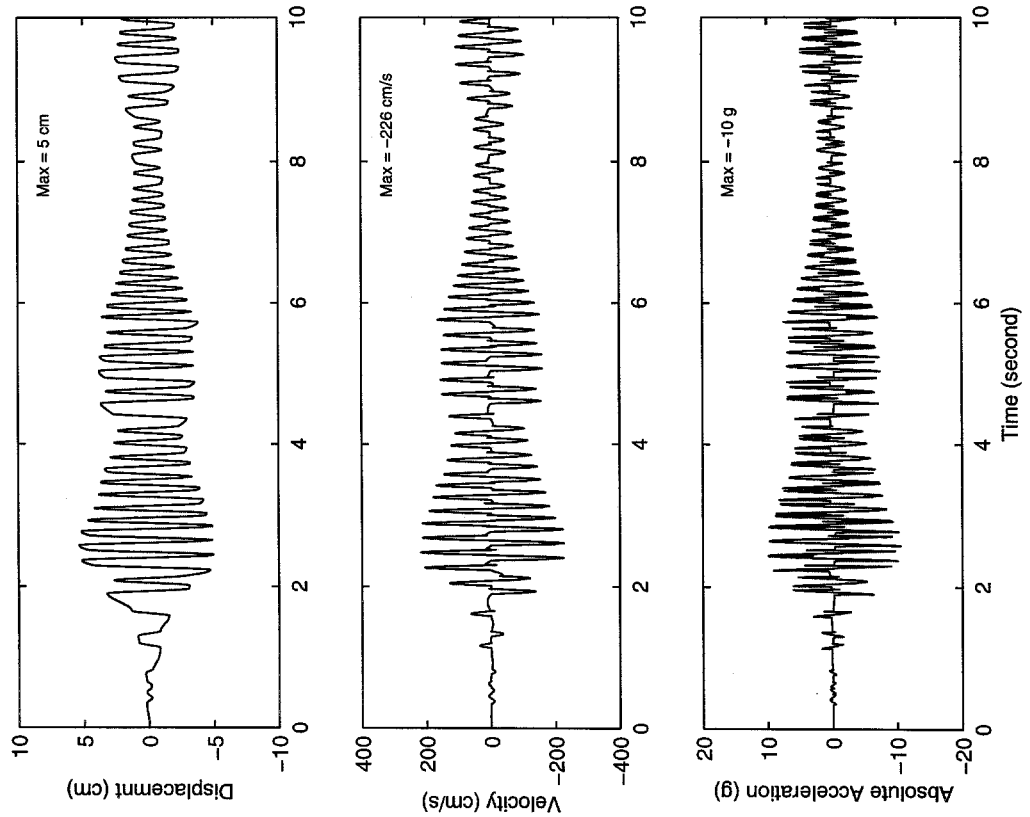

Figure 2.3.9: Displacement, velocity, and acceleration time history responses of the AS controlled by the OCS algorithm and excited by the ELC ground motion

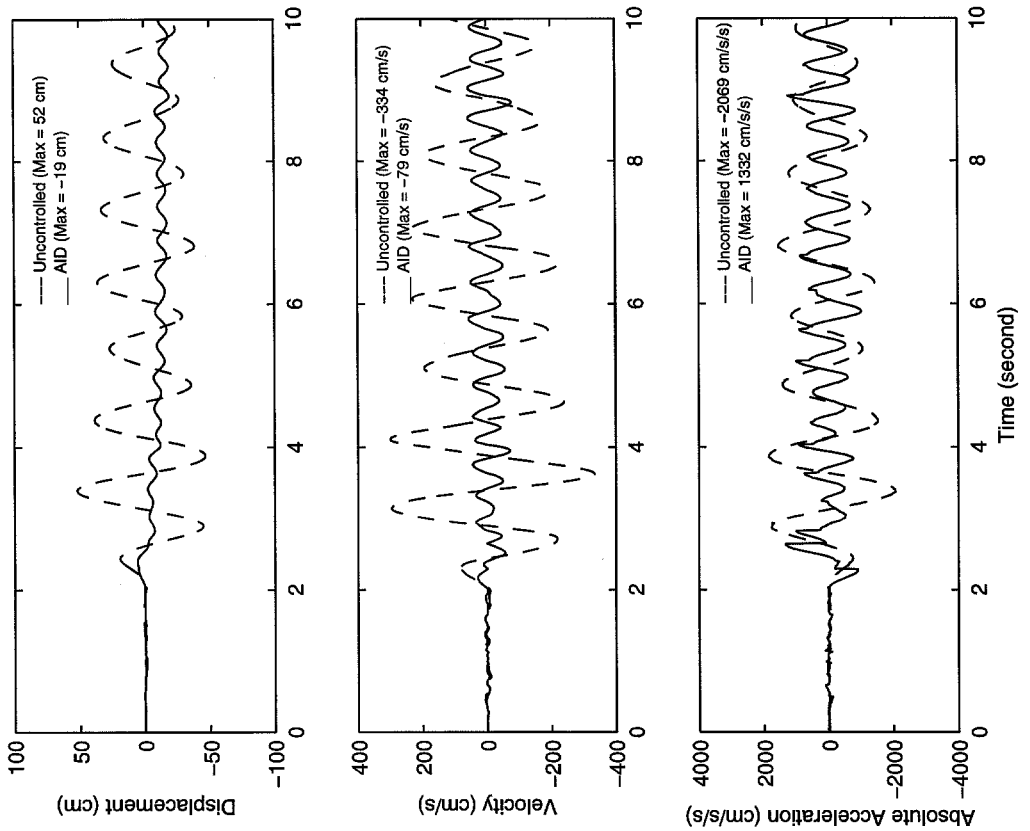

Figure 2.3.12: Displacement, velocity, and acceleration time history responses of the AS controlled by the AID algorithm and excited by the RRS ground motion ($\gamma = 4$)

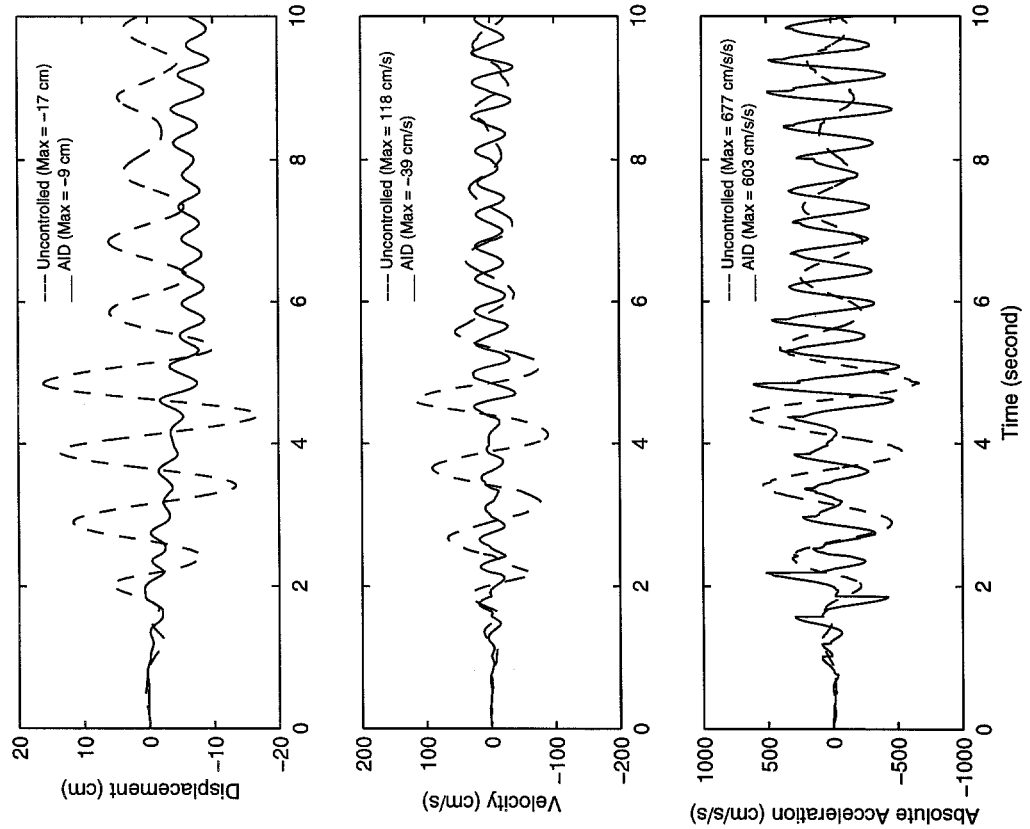

Figure 2.3.11: Displacement, velocity, and acceleration time history responses of the PS controlled by the AID algorithm and excited by the ELC ground motion ($\gamma = 4$)

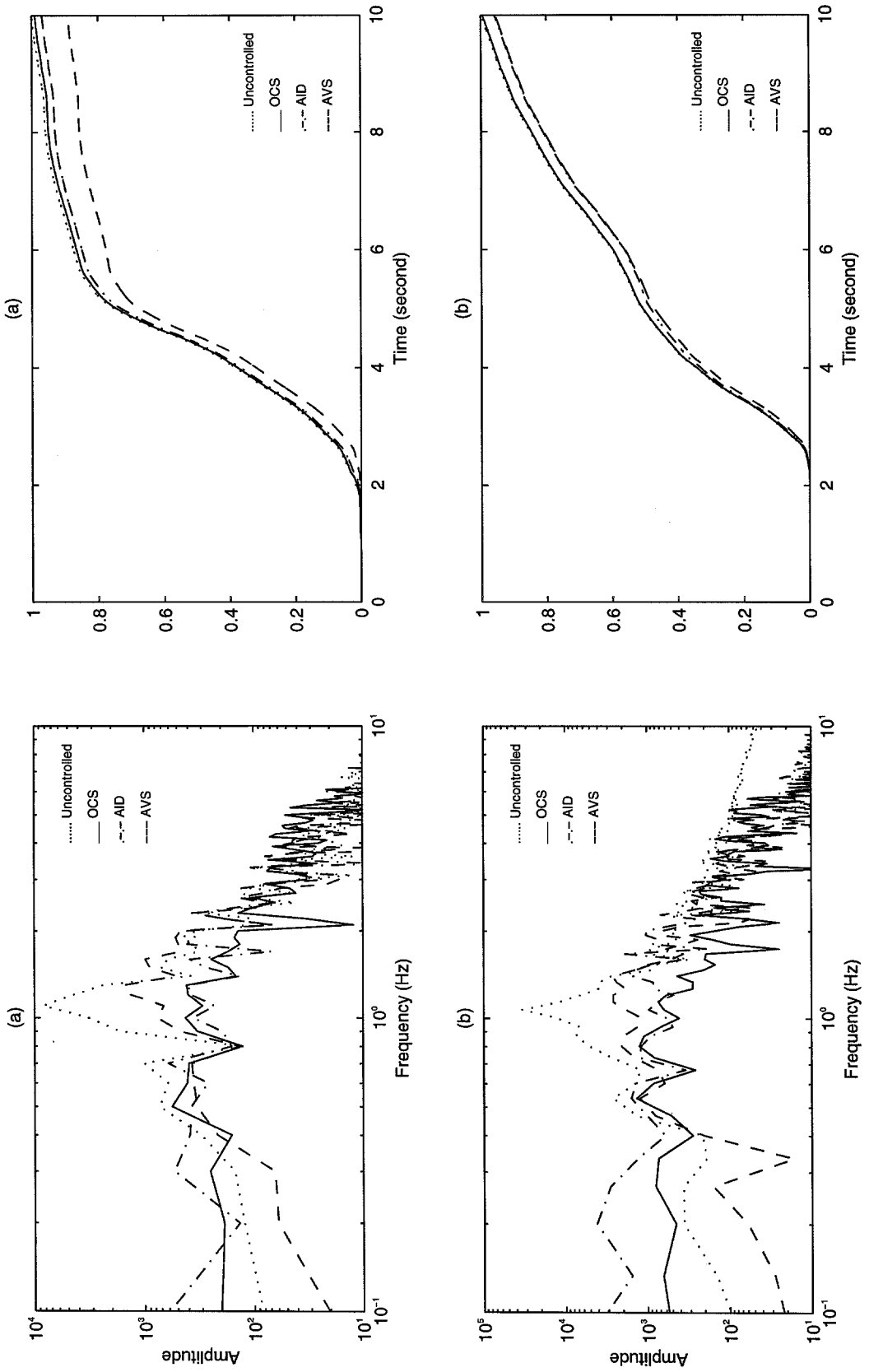

Figure 2.3.13: Fourier Amplitude Spectra of the responses of the PS excited by the (a) ELC and (b) RRS ground motions

Figure 2.3.14: Energy flow diagrams of the AIC system excited by the (a) ELC and (b) RRS ground motions

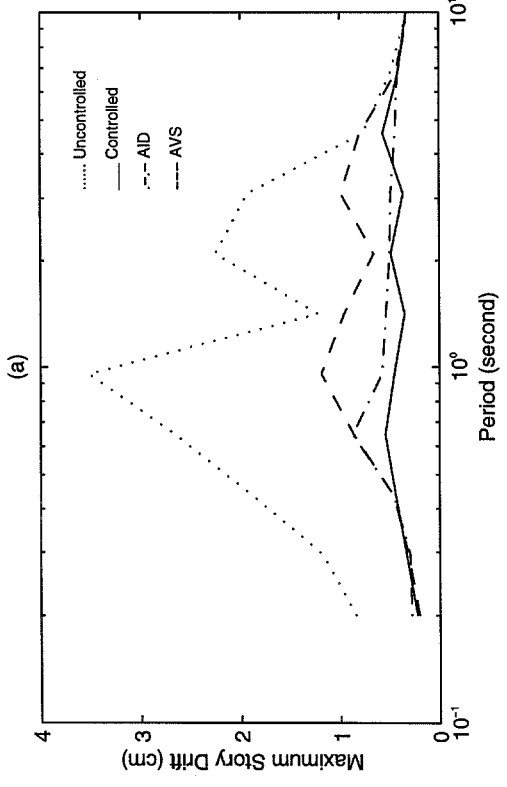

Figure 2.4.1: SDS of the PS under the (a) ELC and (b) RRS excitations

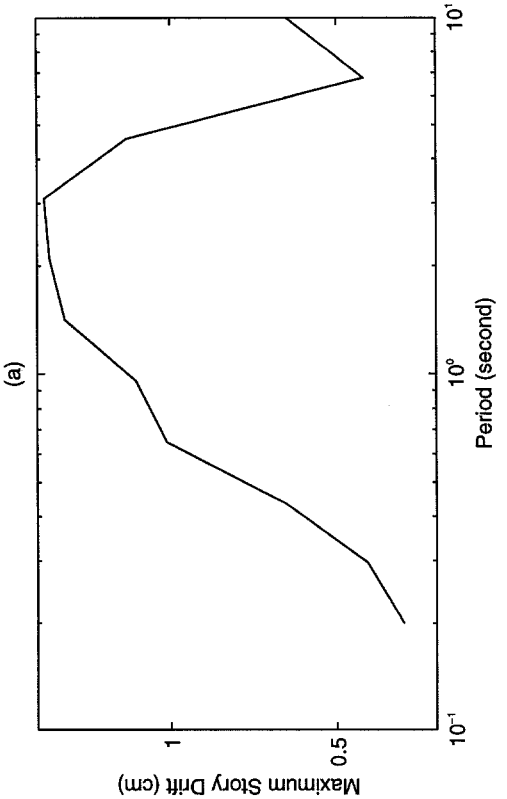

Figure 2.4.2: SDS of the AS under the (a) ELC and (b) RRS excitations

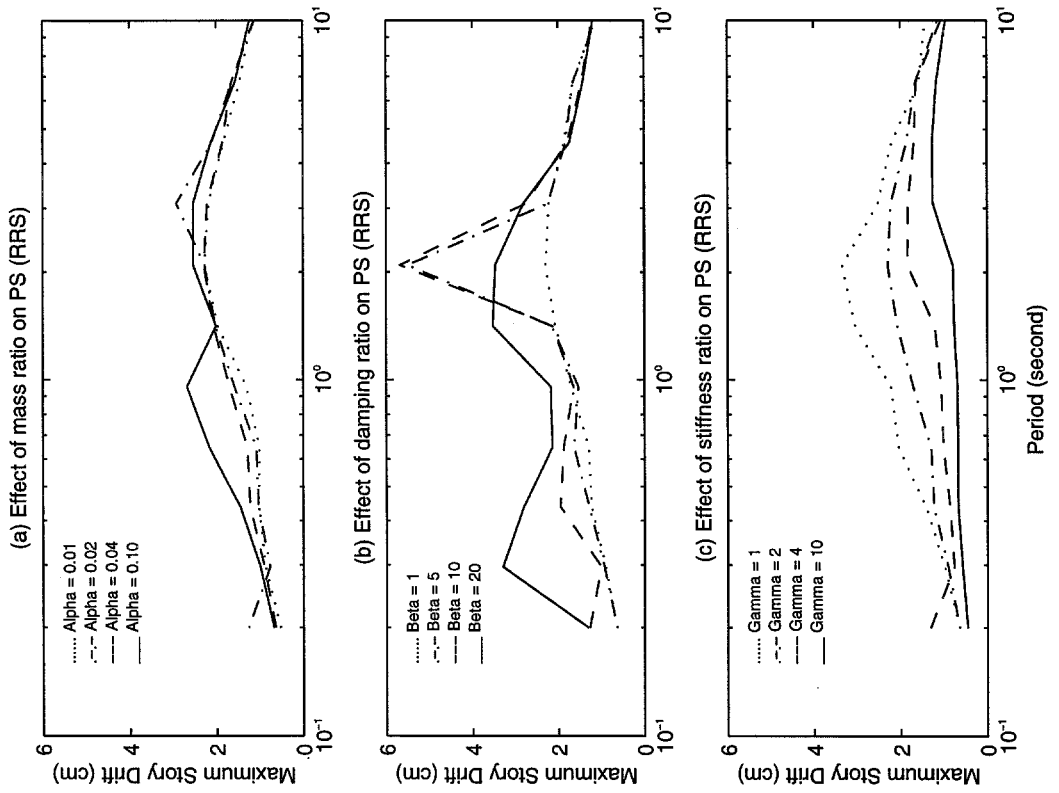

Figure 2.4.4: SDS of the PS excited by the RRS ground motion (effects of the mass, damping, and stiffness of the AS)

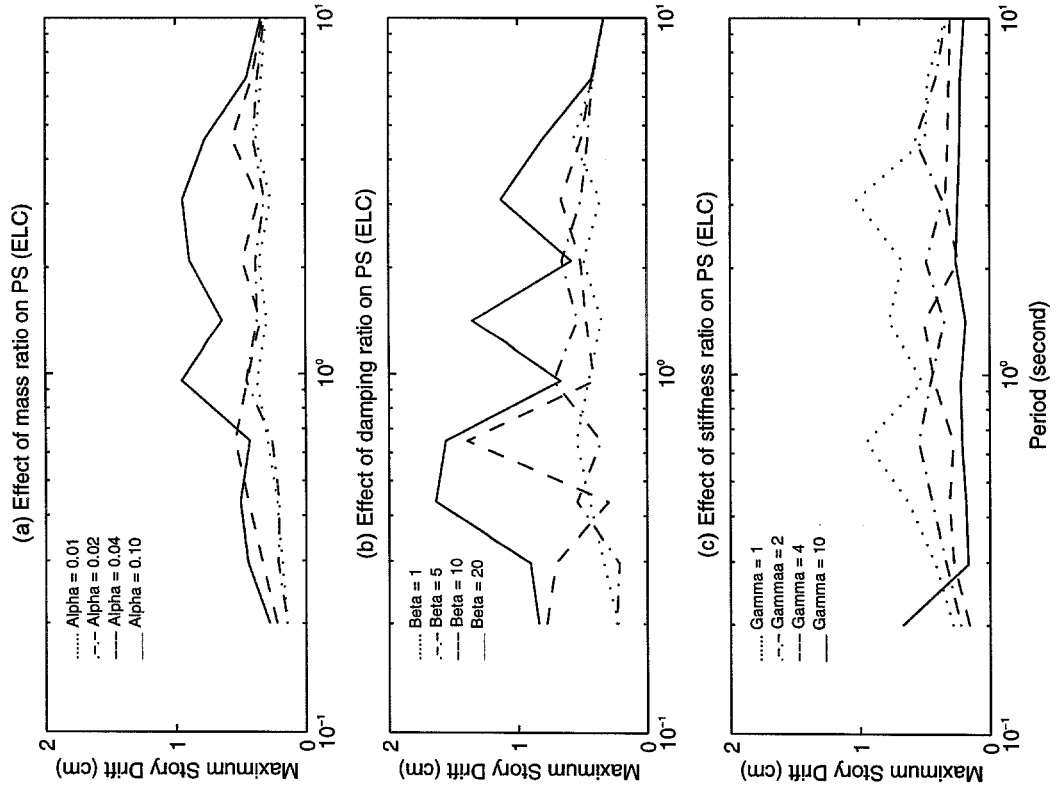

Figure 2.4.3: SDS of the PS excited by the ELC ground motion (effects of the mass, damping, and stiffness of the AS)

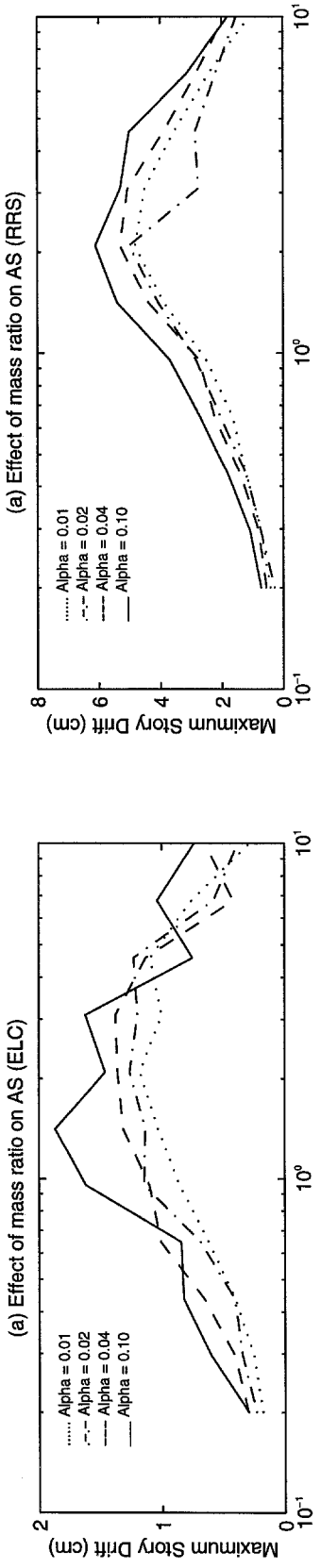

Figure 2.4.5: SDS of the AS excited by the ELC ground motion (effects of the mass, damping, and stiffness of the AS)

Figure 2.4.6: SDS of the AS excited by the RRS ground motion (effects of the mass, damping, and stiffness of the AS)

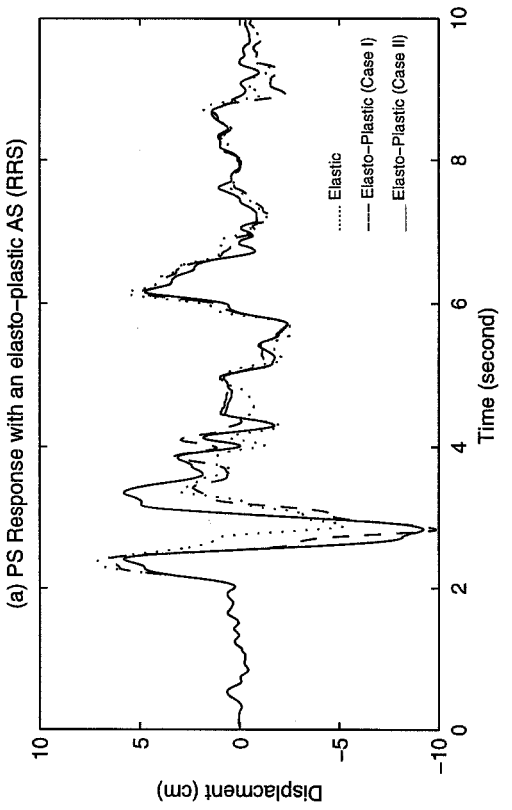

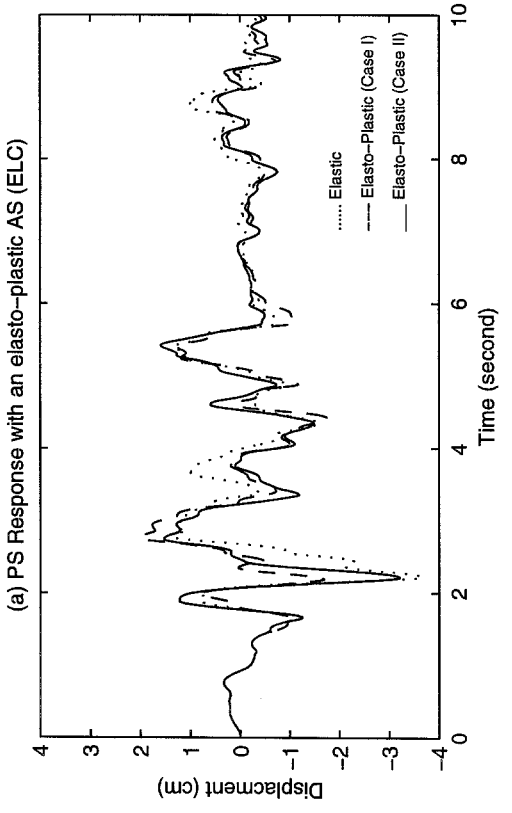

Figure 2.4.7: Displacement time histories of the (a) PS and (b) AS with an elasto-plastic AS excited by the ELC ground motion

Figure 2.4.8: Displacement time histories of the (a) PS and (b) AS with an elasto-plastic AS excited by the RRS ground motion

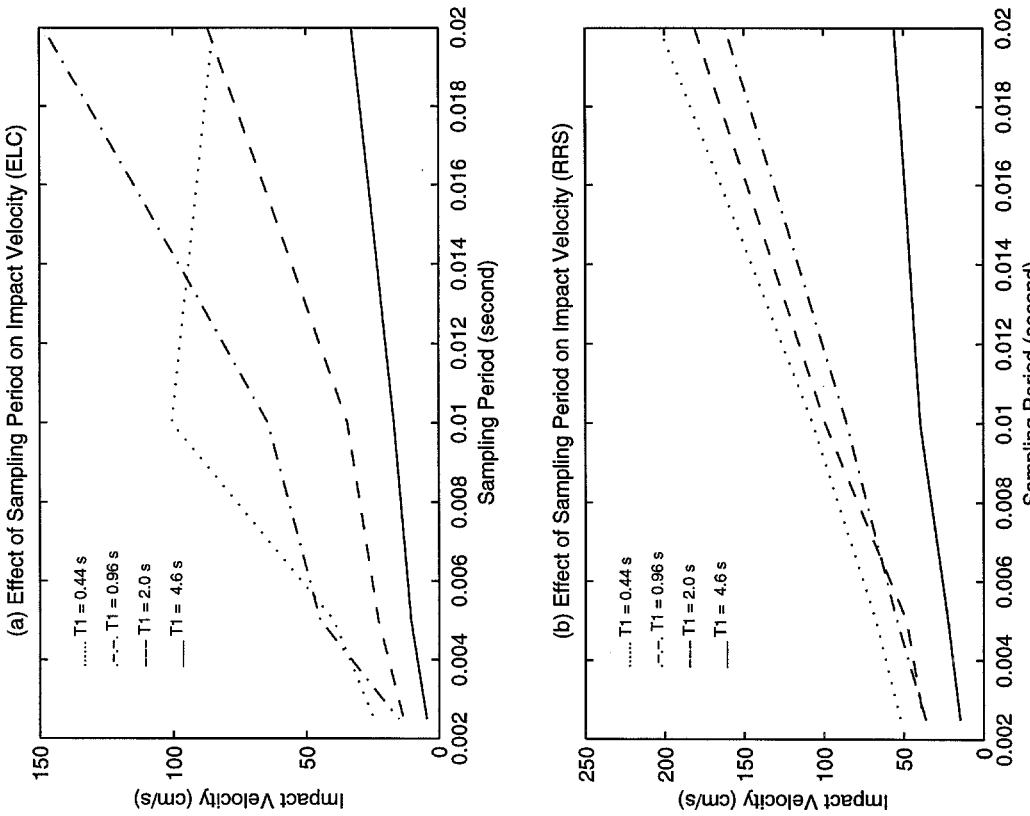

Figure 2.5.1: Effect of sampling interval on the impact velocity excited by the (a) ELC and (b) RRS ground motions

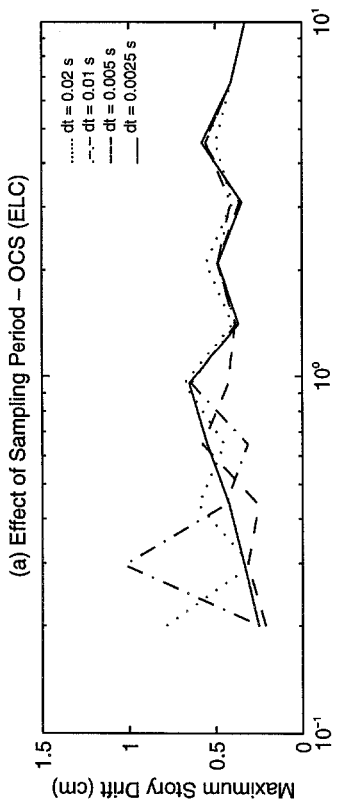

Figure 2.5.2: Effect of sampling interval - SDS of the PS excited by the ELC ground motion

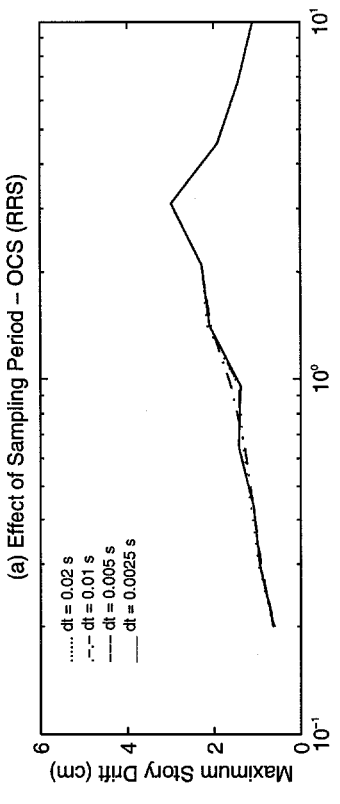

Figure 2.5.3: Effect of sampling interval - SDS of the PS excited by the RRS ground motion

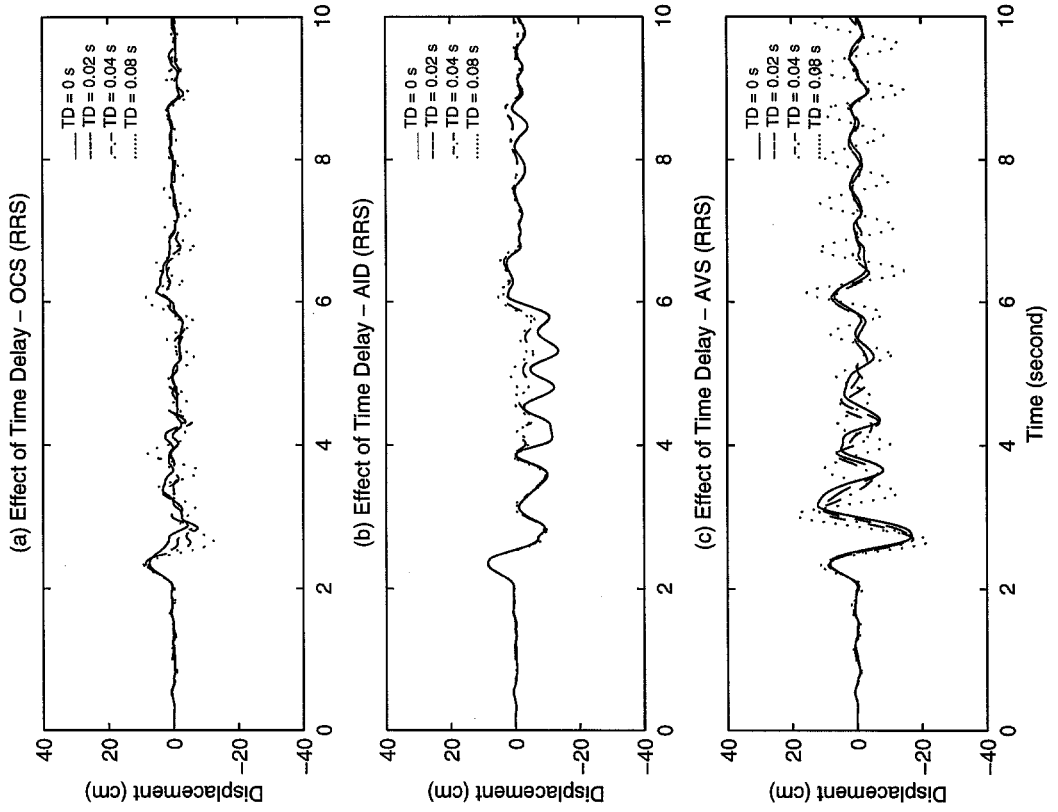

Figure 2.5.5: Effect of time delay - displacement time histories of the PS excited by the RRS ground motion

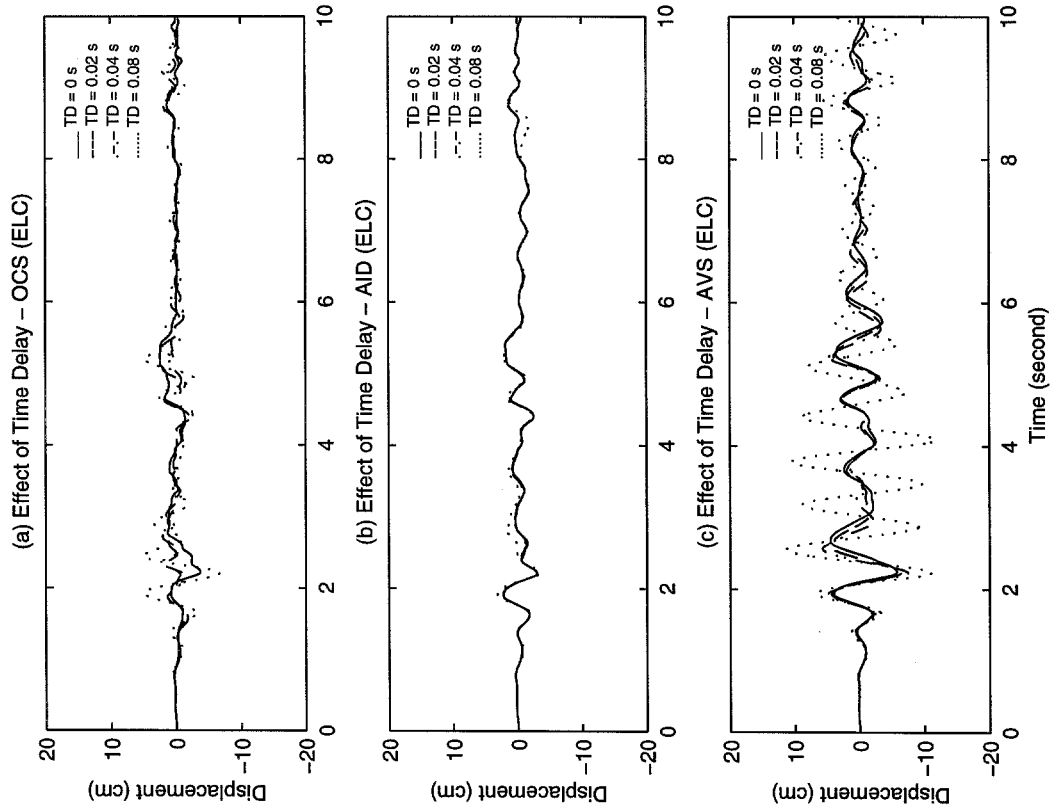

Figure 2.5.4: Effect of time delay - displacement time histories of the PS excited by the ELC ground motion

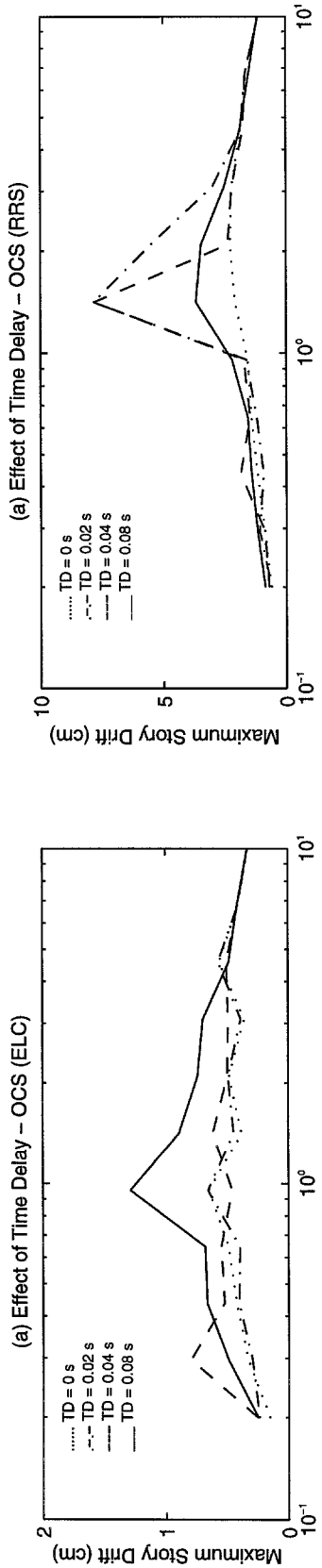

Figure 2.5.6: Effect of time delay - SDS of the PS excited by the ELC ground motion

Figure 2.5.7: Effect of time delay - SDS of the PS excited by the RRS ground motion

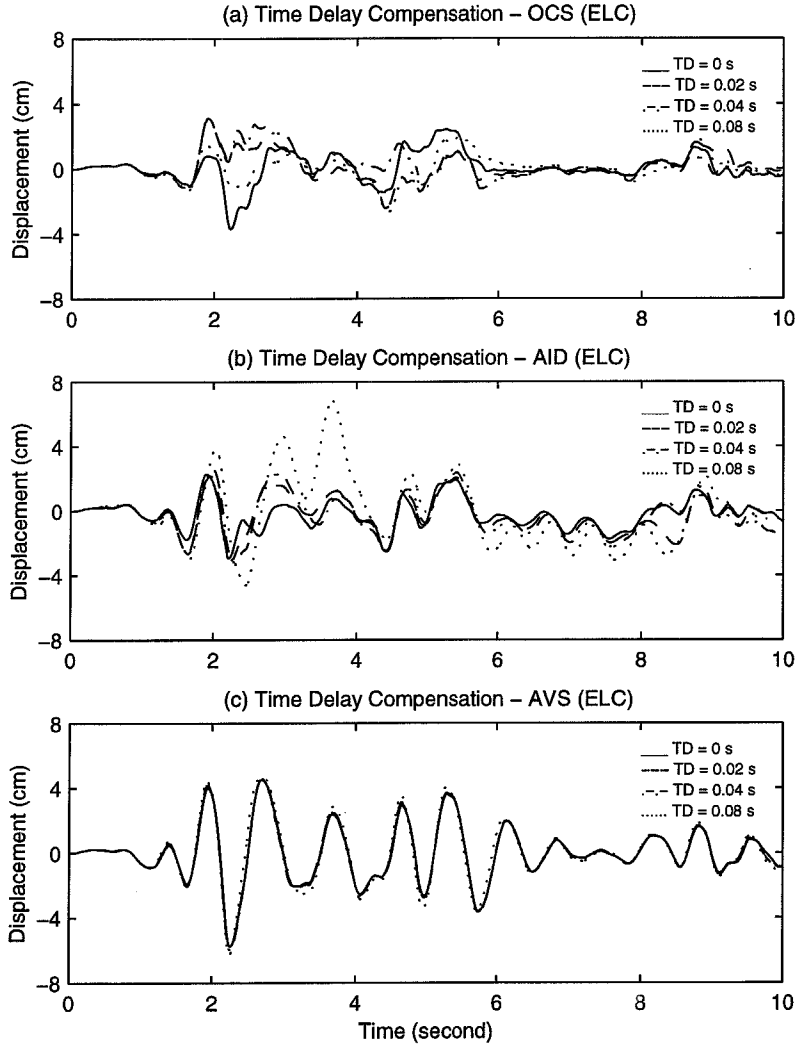

Figure 2.5.8: Time delay compensation - displacement time histories of the PS excited by the ELC ground motion

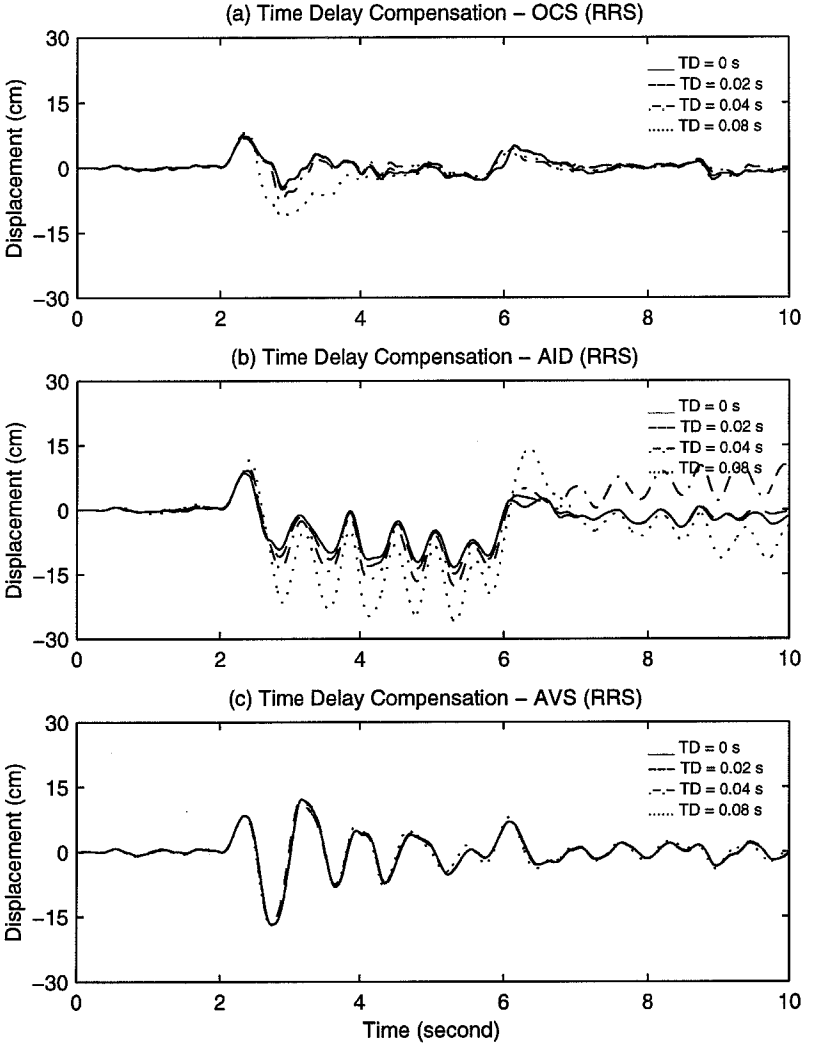

Figure 2.5.9: Time delay compensation - displacement time histories of the PS excited by the RRS ground motion

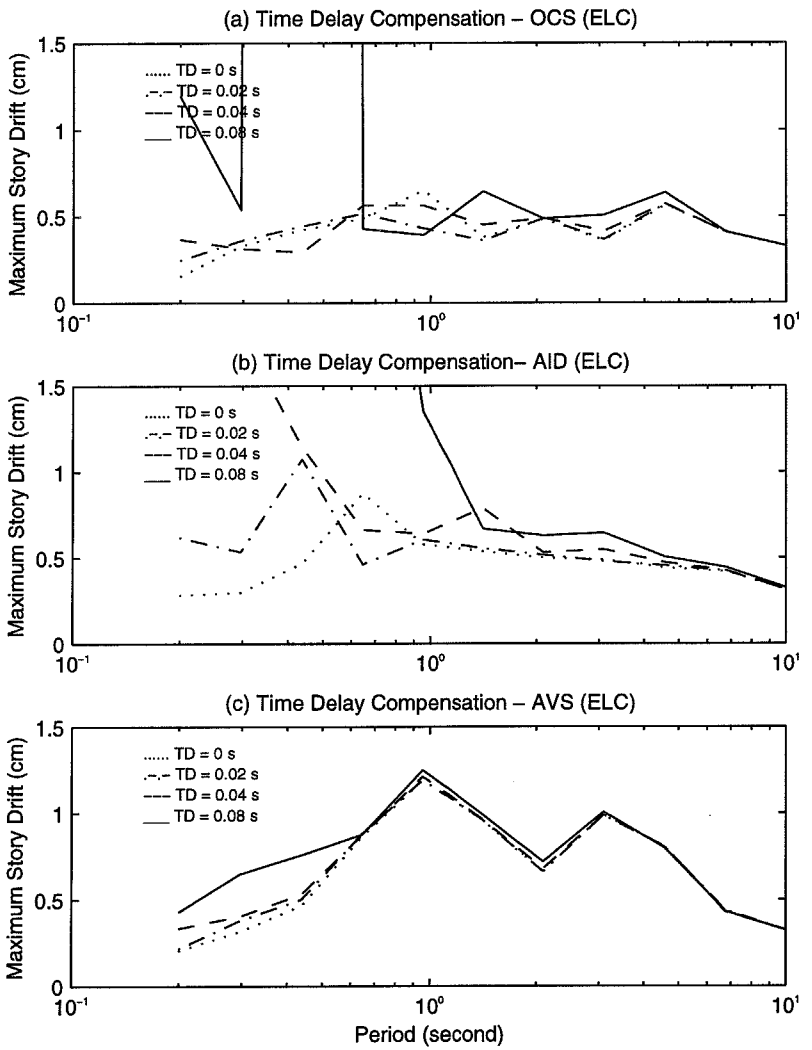

Figure 2.5.10: Time delay compensation - SDS of the PS excited by the ELC ground motion

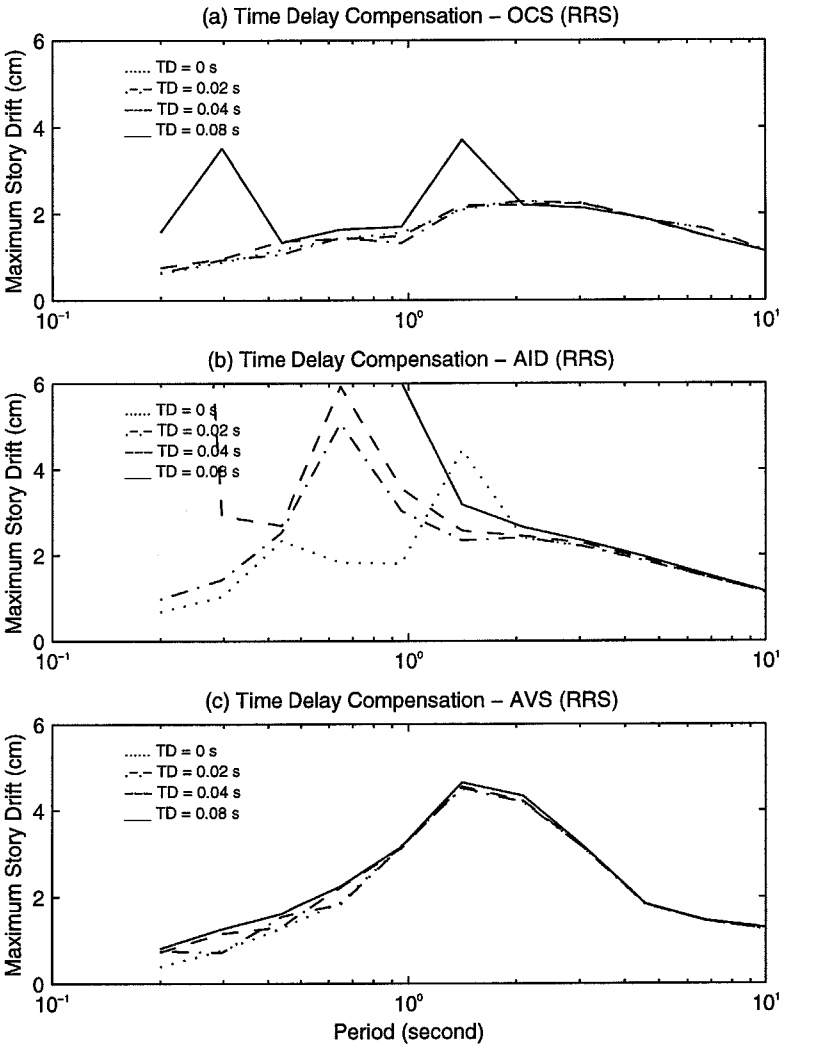

Figure 2.5.11: Time delay compensation - SDS of the PS excited by the RRS ground motion

Chapter 3

Multi-Degree-of-Freedom Systems

This chapter extends the AIC concept from SDOF systems to Multi-Degree-of-Freedom (MDOF) systems. To simplify the number of possible structural configurations needed to be examined in each sampling period, two sub-optimal control approaches are proposed. The effectiveness of the OCS, AID, and AVS algorithms in these two control approaches are demonstrated through time history and Response Spectrum analyses of the AIC system in earthquake ground motions. The effects of mass, damping, and stiffness of the AS on the response of the PS are investigated in parametric studies. Practical issues such as the sampling interval and time delay on the system performance are also examined. The efficacy of the simple predictive time delay compensation scheme developed in Chapter 2 is tested.

3.1 The Active Interaction Control Concept (MDOF)

3.1.1 Problem Formulation

It was shown in Chapter 2 that the seismic response of the PS in an AIC system can be significantly suppressed by actively attaching or detaching the PS and AS according to either the OCS, AID, or AVS algorithm. Such analyses were conducted for cases in which the PS and AS were each modeled by a SDOF system. Since the physical properties of the SDOF system can be thought of as corresponding to those of a particular mode

of a MDOF system, the results obtained from the SDOF approach in Chapter 2 can be viewed as a first order approximation of the dynamic behavior of the MDOF system.

As a follow-on study, this chapter extends the AIC concept from SDOF systems to MDOF systems. For simplicity, but without loss of generality, the PS and AS considered herein are respectively modeled as an N-story shear building (an N-DOF system), and a series of active bracing systems (N SDOF systems) constructed within each story of the PS. The vibration of the PS is controlled by the dynamic interactions between the PS and AS based on their relative motion according to a prescribed AIC algorithm.

In this chapter, the characteristics of the AIC system described earlier in Section 2.1.1 are still valid. To avoid unnecessary future confusion, it is prudent here to clarify some of the terms that will be used throughout this chapter.

The term 'story' represents a complete horizontal division of a building that comprises the structural and nonstructural contents between two adjacent levels. The term 'floor' refers to the top slab of a certain story on which its upper story stands. By this definition, the '1st floor' refers to the top slab of the 1st (ground) story. The term 'story drift' means the relative horizontal displacement, measured in centimeters (cm), between two adjacent floors. A schematic plot showing these definitions is given in Figure 3.1.1.

It is assumed that the mass of the N-story shear building is concentrated at the top floor of each story, and each floor is interconnected by massless columns which provide linear restoring forces in the lateral direction. The building stories are numbered from the ground (1st story) to the top (N^{th} story). The story mass and stiffness of the PS and AS are respectively denoted by m_{1i}, k_{1i}, and m_{2i}, k_{2i}, where i is the story number, and the first subscript, 1 or 2, represents the PS or the AS respectively.

During an earthquake, the PS is excited by the seismic wave transmitted into the system from the ground, and the AS is shaken by the motion of the floor upon which it is fixed. The motion of the PS is actively controlled by attaching or detaching the AS to its upper floor according to an AIC algorithm which will be described momentarily.

Suppose that at time, t, the PS and AS are attached in the first M ($M <= N$) stories and that the PS and AS were attached in the ith story at time t_i and maintained thereafter, where t_i, $< t$ and $i \in [1, M]$. Then the motion of the AIC system, now a ($2N$-M) DOF system, is given by the following matrix equation

$$M\ddot{X}(t) + C\dot{X}(t) + KX(t) = MLa(t) + F(t) \tag{3.1.1}$$

where M, C, and K are, respectively, the ($2N$-M)×($2N$-M) mass, damping, and stiffness matrices of the entire AIC system; X is the ($2N$-M)-dimensional displacement vector of the PS (N-DOF system) and detached AS ((N-M)-DOF system) relative to the ground

$$X(t) = [x_{11}(t), x_{12}(t), \cdots\cdots, x_{1N}(t), x_{2(M+1)}(t), x_{2(M+2)}(t), \cdots\cdots, x_{2N}(t)]^T \tag{3.1.2}$$

where $x_{1i}(t)$ and $x_{2i}(t)$ are, respectively, the displacements of the PS and AS on the ith floor relative to the ground; L is the ($2N$-M)-dimensional constant vector

$$L = [1, 1, \cdots\cdots, 1, 1]^T; \tag{3.1.3}$$

$a(t)$ is the accelerogram of the ground motion; and $F(t)$ is the ($2N$-M)-dimensional control force vector

$$F(t) = K_a X_a(t) \tag{3.1.4}$$

where K_a is the ($2N$-M)×$2N$ location-stiffness matrix whose non-zero entries corresponding to the locations of the interaction or control force are the stiffness of the AS, and $X_a(t)$ is the $2N$-dimensional vector which keeps the displacements of the PS and AS measured at the initiation of the last attachment at each story level

$$X_a(t) = [x_{11}(t_1), x_{12}(t_2), \cdots\cdots, x_{1N}(t_N), x_{21}(t_1), x_{22}(t_2), \cdots\cdots, x_{2N}(t_N)]^T. \tag{3.1.5}$$

At those stories where the PS and AS are attached, the displacement, velocity, and acceleration of the AS are related to the corresponding terms of the PS by

$$\left.\begin{aligned} x_{2i}(t) &= x_{1,i}(t) + [x_{2i}(t_i) - x_{1i}(t_i)] \\ \dot{x}_{2i}(t) &= \dot{x}_{1i}(t) \\ \ddot{x}_{2i}(t) &= \ddot{x}_{1i}(t) \end{aligned}\right\} \quad i = 1 \text{ to } M. \tag{3.1.6}$$

Details of how to construct the system matrices in Equation (3.1.1) are given in Appendix A.4 where three different configurations of a three-story shear building (PS) and associated AS are exemplified and corresponding system matrices are given.

Equation (3.1.1) is solved in the state-space representation as in Section 2.1.5.

It is of interest to note that the number of DOF of the AIC system varies with the structural configuration in time. As mentioned earlier, the number of DOF of the AIC system is $2N$-M when the PS and AS are attached in M out of N stories. Two extreme cases are shown in the first two examples in Appendix A.4, where the number of DOF of the AIC system are, respectively, N and $2N$ for the cases that the PS and AS are, respectively, attached ($M = N$) in all stories and detached ($M = 0$) in all stories.

The variation of the number of DOF of the AIC system partially reveals the basis of the AIC strategy. That is, actively altering the structural configuration of the system to enable the PS to respond to external dynamic loads in the most favorable manner according to a prescribed control algorithm. This is also the original idea behind the pioneer work of the AVS algorithm.

It is also of interest to note that the control force between the PS and AS, $U(t)$, is generated by the active interaction between the attached PS and AS with no need for an external energy source. The AS serves as the actuator. The equation of motion of the AS, coupled with that of the PS in Equation (3.1.1), describes the actuator dynamics.

As seen in the examples of Appendix A.4, the non-zero entries in the stiffness matrix, K_a, come from the stiffness of the AS, and the entries in the displacement vector, X_a, originate from the displacement of the PS and AS relative to the ground measured at the initiation of their last attachment. This clearly indicates that the control force applied to the PS at each story level is just the interaction force generated by the relative displacement between the PS and AS measured at the initiation of their last attachment.

3.1.2 Control Objectives

As before, for a near-field earthquake with a pulse-like time history, the main control objective of AIC for MDOF systems is to minimize the maximum story drift. For a far-field earthquake with its more random-appearing time history, an additional control ob-

jective is to reduce the absolute acceleration of the PS so as to protect structural contents and improve the comfort of occupants. For shear buildings considered in this study, the maximum story drift normally occurs in the 1st story between the 1st floor slab and the ground, and the maximum absolute acceleration in the top story is often the control target.

3.1.3 Control Approaches

At each story level, two possible configurations between the PS and AS exist: attach and detach. Hence, the total number of the possible structural configurations for N-Story shear buildings is 2^N. If all state variables of the AIC system and the ground acceleration are observable instantaneously, then an optimal control approach can be obtained theoretically, according to which the most appropriate structural configuration can be selected from the 2^N combinations in each sampling interval.

However, the number of possible configurations increases dramatically with the number of stories. For shear buildings with 10 or more stories ($N > 10$), this number ($2^N > 1000$) becomes so large that it is practically impossible to determine the most appropriate configuration from so many configurations in each sampling interval.

With the above in view, it is proposed that, instead of trying to select the most appropriate structural configurations from all possible combinations, the control decision is made at each story level individually. In other words, the attachment or detachment between the AS on the ith floor and the PS on (i+1)th floor is solely determined by the relative motions of the PS between the ith and (i+1)th floors and the AS on the ith floor, regardless of the motions of the PS and AS on other floors.

Apparently, such control strategy for each story level is locally optimal, but in general may not be optimal for the system as a whole, as the control decision at one story level could adversely affect the response of other stories. Nevertheless, the evident benefit of this control strategy for high-rise buildings remains. By this control strategy, the total number of possible structural configurations needed to be examined in each sampling

interval is reduced to $2N$ from 2^N. It is hoped that this simplified sub-optimal control approach is able to yield admissible tradeoff in the controlled system response. This leads to the first control strategy proposed in this chapter, which is termed as the Nodal Control (NC) approach.

A prerequisite for application of the NC approach is that the state variables, such as the displacement and velocity, of the PS and AS are completely observable at all story levels in each sampling interval. In practice, due to the limited sensors installed in the AIC system, the state variables of an AIC system are often partially observable, which is known as the limited state information. This motivates the development of the second control approach strategy in this chapter, which is termed as the Modal Control (MC) approach.

In lieu of making control decision in each of the N stories separately as in the NC approach, the MC approach focuses on the vibrational energy removal associated with one particular or several dominant modes of the PS. This approach is based on the observation that for earthquake excitations only a few (perhaps, a single) response modes of the PS are significantly excited. The vibrational energy associated with these highly excited modes constitutes the major portion of the total vibrational energy in the PS. For mid-rise shear buildings (10 to 20 stories), the first mode is likely to dominate the seismic response because (a) it possesses the largest modal participation factor, and (b) the fundamental frequency of these shear buildings is often within the frequency range of the maximum seismic energy.

In the MC approach, the following two undesirable situations should be treated with special care. The first situation is that if the PS and AS are not attached or detached synchronically in all stories, the motion of the PS will probably not be dominated by any single mode. This effect will be seen in the cases of NC approach in Section 3.2.1. The second situation is the so-called spillover effect, in which case the control decision appropriate to control one mode may unexpectedly excite other uncontrolled modes.

To avoid the occurrence of these undesirable situations in the MC approach, the stiffness of the AS is intentionally chosen to be proportional to that of the PS at each story level so that the stiffness distribution of the PS will remain unchanged for the cases that the PS is attached to or detached from the AS. As a result, the motion of the PS can be maintained primarily in the first mode during the control process. Recall that the mass of the AS is much smaller than that of the PS.

In addition, the mass of the AS is carefully adjusted so that the frequencies of the AS at all story levels are tuned to the same value. As a result, an identical control decision is likely to be reached in all stories simultaneously in each sampling interval. Therefore, in the MC approach, the PS and AS can be attached or detached at all story levels simultaneously in accordance with the control decision for any story where the state variables are measured.

Since the objective of AIC is to reduce the maximum story drift of the PS and since the maximum story drift of a shear building mostly occurs in the 1st story, the PS and AS are concurrently attached or detached at all story levels according to the control decision for the 1st story. Therefore, the total number of possible structural configurations needed to be examined in each sampling interval drops to 2 for the MC approach, from $2N$ for the NC approach, and from 2^N for the optimal control approach.

It should be noted that in theory the best sensor location to measure the response of the first mode is at the top floor where the largest modal displacement occurs. However, since the control decision is made based on the motion of the PS and AS on the 1st floor slab relative to the ground, it is often convenient to place the sensor on the 1st floor slab to facilitate data acquisition and processing in the MC approach.

Table 3.1.1 summarizes the characteristics of the optimal control, NC, and the MC approaches. The numbers in parenthesis are the numbers of possible structural configurations needed to be examined in each sampling period for cases N = 10 and 20.

Table 3.1.1: Characteristics of the optimal control, NC and the MC approaches

Control approach	State variables measured	Number of configurations examined in each sampling interval	Attachment made at story levels
Optimal	all N stories	2^N (1024, 2048)	individually
Nodal	all N stories	$2N$ (20, 40)	individually
Modal	1st story	2 (2, 2)	simultaneously

3.1.4 Control Algorithms

At any story level, the OCS, AID, and AVS control algorithms for MDOF systems are essentially the same as for SDOF systems. The control decision for a particular story, say the ith story, should be made based on the relative ***story*** velocity and displacement of the PS and AS in the same story, i.e., the difference between the velocity and displacement on the ith floor and those on the (i-1)th floor. In the 1st story, these quantities become the relative velocity and displacement on the 1st floor slab relative to those of the ground.

In summary, the OCS, AID, and AVS algorithms for the SDOF systems in Section 2.1.5 can be likewise applied to each story of the MDOF systems if the following changes are made:

$$x_1 \to x_{1i} - x_{1(i-1)}, \quad x_2 \to x_{2i} - x_{1(i-1)}, \quad \dot{x}_1(t) \to \dot{x}_{1i} - \dot{x}_{1(i-1)}, \quad \dot{x}_2 \to \dot{x}_{2i} - \dot{x}_{1(i-1)}, \; i = [2, N]$$

and

$$x_1 \to x_{1i}, \quad x_2 \to x_{2i}, \quad \dot{x}_1(t) \to \dot{x}_{1i}, \quad \dot{x}_2 \to \dot{x}_{2i}, \; i = 1.$$

3.1.5 Structural Configuration

Mass, damping, and stiffness matrices of the PS

Most of the cases considered in this chapter involve an 8-story (steel frame) shear building (PS), whose fundamental period (in second) is given by the UBC [ICBO, 1994]

$$T_{11} = 0.0853(Nh)^{3/4} \tag{3.1.7}$$

where N is the number of stories and h is the story height (in meter). Putting $N = 8$ and $h = 3.5$ meters, Equation (3.1.7) yields $T_{11} = 0.96 \cong 1$ second. Therefore, the response obtained for the 1 second period SDOF systems in the preceding chapter may be viewed as the first mode response of this 8-story shear building.

For simplicity, each story mass of the PS is taken as a constant, m, and the mass matrix of the PS therefore becomes $M_1 = mI$. The story stiffness of the PS is assumed to be linearly distributed along the height of the PS

$$k_{1i} = \left(2 - \frac{i-1}{N-1}\right) k_0 \tag{3.1.8}$$

so that $k_{11} = 2k_0$ and $k_{1N} = k_0$, where k_0 is the scaling factor to be determined.

The Rayleigh Quotient for the PS is

$$\omega_{11}^2 = \left(\frac{2\pi}{T_1}\right)^2 = \frac{(\phi_{11}, K_1\phi_{11})}{(\phi_{11}, M_1\phi_{11})} = k_0(\phi_{11}, K_0\phi_{11}) \tag{3.1.9}$$

where ω_{11} is the fundamental frequency of the PS, K_1 is the stiffness matrix of the PS ($K_1 = K_0$ when $k_0 = 1$), $(\cdot\ ,\ \cdot)$ denotes the operation of vector inner product, and the mode shape vector of first mode of the PS, ϕ_{11}, is found by solving the following eigen-value problem

$$K_0\phi_{11} = M_1\phi_{11} \tag{3.1.10}$$

and is normalized with respect to the mass matrices by

$$(\phi_{11}, M_1\phi_{11}) = 1. \tag{3.1.11}$$

Now, k_0 can be determined from Equation (3.1.9)

$$k_0 = \frac{4\pi^2}{T_{11}^2(\phi_{11}, K_0\phi_{11})}. \tag{3.1.12}$$

The damping matrix of the PS can be assembled from the modal space

$$C_1 = \phi_1 diag(2\omega_{11}\zeta_{11}, 2\omega_{12}\zeta_{12}, \cdots, 2\omega_{1i}\zeta_{1i}, \cdots, 2\omega_{1N}\zeta_{1N})\phi_1^T \tag{3.1.13}$$

where ω_{1i} and ζ_{1i} are the frequency and modal damping ratio corresponding to the ith mode of the PS, and ϕ_1 is the mode shape matrix of the PS. ω_{1i} (the ith column of ω_1) and ϕ_1 can be found by solving the following generalized eigen-value problem

$$[K_1 - \omega_1^2 M_1]\phi_1 = 0. \tag{3.1.14}$$

It should be noted that the modal properties of the PS obtained in the above derivation are for the case without the presence of the AS. This is justifiable because the mass of the AS is much smaller than that of the PS. The presence of the AS will only slightly affect the mode shape of the PS. It should also be noted that the mass, damping, and stiffness matrices of the PS are fully deterministic when the number of stories, N, and the story mass of the PS, m, are specified.

Mass and stiffness of the AS

As mentioned earlier, to keep the PS vibrating in its first mode as much as possible during the control process, the stiffness of the AS should be chosen proportional to that of the PS at each story level, i.e.,

$$k_{2i} = \gamma k_{1i} = \gamma\left(2 - \frac{i-1}{N-1}\right)k_0 \tag{3.1.15}$$

where γ is the stiffness ratio between the AS and the PS, and $\gamma > 1$.

In order to tune the frequencies of the AS to be uniform at all story levels, the mass distribution of the AS should be proportional to the stiffness distribution, i.e.,

$$m_{2i} = \left(2 - \frac{i-1}{N-1}\right)\alpha m \tag{3.1.16}$$

where

$$\alpha = \frac{m_{21}}{m} << 1. \tag{3.1.17}$$

Nominal values

As may be shown in Equation (2.1.7), the dynamic response for a linear system remains the same if the mass, damping, and stiffness of the system change proportionally. Therefore, in all cases examined in this chapter, the mass, damping, and stiffness of the PS and AS, are normalized with respect to the 1st story mass of the PS.

The mass of the AS is specified by taking α = 10%. To avoid the drifting phenomenon in the AID algorithm shown in Figures 2.3.11 and 2.3.12 and to make a fair comparison of all AIC algorithms, the story stiffness ratio between the AS and PS is taken as 2, i.e., $\gamma = 2$, although a better control result is expected to be achieved in the OCS and AVS algorithms for a larger γ. The damping ratio of the PS in each mode, ζ_{1i}, i=[1, N], is assumed to be 2%. The damping ratio of the AS in each story, ζ_{2i}, i=[1, N], is assumed to be 2%. These values are considered to be physically realizable in view of the characteristics of the AIC system. Table 3.1.2 summarizes the normalized mass and stiffness (with respect to the 1st story mass of the PS), damping ratio, and frequency of the PS and AS of the 8-story shear building.

Table 3.1.2: Normalized mass and stiffness, damping ratio, and frequency of the PS and AS of the 8-story shear building

	PS				AS			
Story/ Modal	Norm. Mass	Damp. Ratio*	Norm. Stiffness	Freq.* (Hz)	Norm. Mass	Damp. Ratio	Norm. Stiffness	Freq. (Hz)
8	1	2%	647	10.19	0.050	2%	1294	25.6
7	1	2%	739	9.07	0.0571	2%	1479	25.6
6	1	2%	832	8.09	0.0643	2%	1664	25.6
5	1	2%	924	7.04	0.0714	2%	1849	25.6
4	1	2%	1017	5.76	0.0786	2%	2033	25.6
3	1	2%	1109	4.28	0.0857	2%	2218	25.6
2	1	2%	1202	2.65	0.0929	2%	2403	25.6
1	1	2%	1294	0.96	0.100	2%	2588	25.6

* modal properties

Base shear

In civil engineering practice, the amount of seismic load carried by a building is often quantified by the dimensionless base shear coefficient

$$\mu = \frac{V}{W} \tag{3.1.18}$$

where V is the maximum base shear of the building, which is equivalent to the maximum shear force in the columns of the 1st story

$$V = k_{11} \max_{\forall t} |x_{11}(t)|, \tag{3.1.19}$$

where k_{11} is the 1st story stiffness of the PS and x_{11} is the 1st story displacement (in cm) of the PS relative to the ground; W is the weight of the building

$$W = \sum_{i=1}^{N} m_{1i} g = 981N \tag{3.1.20}$$

in which m_{1i} is the normalized mass of the PS given in Table 3.1.2, and $g = 981$ cm/s/s.

For the 8-story shear building, Table 3.1.2 gives k_{11} = 1294 and N = 8. Equation (3.1.18) becomes

$$\mu = 0.165 \max_{\forall t} |x_{11}(t)|. \tag{3.1.21}$$

Since the maximum story drift of a shear building mostly occurs in the 1st story, the control objective - to minimize the maximum story drift is therefore identical to minimizing the base shear or base shear coefficient of the building. Hence, all results and discussions on the maximum story drift in later part of this chapter apply likewise to the base shear or base shear coefficient.

3.2 Seismic Responses of MDOF Systems (NC Approach)

3.2.1 Story Drift Responses of the PS

Figures 3.2.1 to 3.2.6 show the 1st, 4th, and 8th story drift responses of the PS. To facilitate easier comparison, Tables 3.2.1 and 3.2.2 give data on the peak and RMS values of the story drift responses in these figures.

It is seen that the story drift responses are greatly reduced in all controlled cases as compared with the uncontrolled case. In the uncontrolled case, the response is gradually built up and the response peak is finally reached in about five seconds. In all controlled cases, such a resonance buildup is completely eliminated as the responses in subsequent

cycles are further suppressed. In fact, the peak response occurring immediately after the first S-wave arrival at approximately 2 seconds is never surpassed by the peaks at later times. Hence, the degree of reduction of the peak response immediately after the first S-wave arrival can be a quick indication of the effectiveness of an AIC algorithm.

In terms of the peak and RMS values of the story drift responses, the controlled PS also clearly performs better than the uncontrolled PS, as seen in Tables 3.2.1 and 3.2.2. Larger reduction is generally observed in the responses of upper stories. As anticipated, the maximum story drift of the PS occurs in the 1st story in all uncontrolled and controlled cases except the one in Figure 3.2.5 wherein the PS is controlled by the AVS algorithm excited by the ELC ground motion.

Table 3.2.1: Peak and RMS values of the 1st, 4th, and 8th story drift responses excited by the ELC ground motion uncontrolled and controlled by the OCS, AID, and AVS algorithms in the NC approach

	1st story		4th story		8th story	
Algorithm	Peak	RMS	Peak	RMS	Peak	RMS
Uncontrolled	3.35	1.15	3.35	1.20	1.67	0.54
OCS	1.99	0.49	1.13	0.26	0.67	0.16
AID	1.98	0.44	1.29	0.33	0.96	0.18
AVS	1.06	0.34	1.25	0.36	0.95	0.17

Table 3.2.2: Peak and RMS values of the 1st, 4th, and 8th story drift responses excited by the RRS ground motion uncontrolled and controlled by the OCS, AID, and AVS algorithms in the NC approach

	1st story		4th story		8th story	
Algorithm	Peak	RMS	Peak	RMS	Peak	RMS
Uncontrolled	10.21	3.68	10.71	3.84	4.33	1.61
OCS	8.77	1.26	2.98	0.55	2.31	0.32
AID	3.95	0.71	3.45	0.66	1.72	0.30
AVS	4.22	0.71	3.78	0.75	2.65	0.35

In the uncontrolled case, the responses of the PS are clearly dominated by the first mode as a harmonic wave with approximately 1 second period is observed in all story responses. In the controlled cases, the dominant effect of the first mode is observable in

the 1st story response, less obvious in the 4th story response, and almost invisible in the 8th story response. This is because, in the NC approach, the control decisions are made independently at each story level. The attachments between the PS and AS in all stories are unlikely to be established at the same time. As a result of such un-synchronized connections between the PS and AS, few lower modes but more higher modes are excited. As reflected in Figures 3.2.1 to 3.2.6, more high frequency contents are brought into the controlled responses than in the uncontrolled ones, especially in upper stories.

Among the AIC algorithms considered, the AVS algorithm provides the smoothest story drift responses and the largest reduction of the peak story drifts in the ELC case; the AID algorithm suppresses the peak story drift to the largest extent in the RRS case; and the OCS algorithm is more effective in reducing the RMS values of the story drift responses.

It should be noted that in the OCS algorithm, a pronounced overshoot occurs in the 8th story response excited by the RRS ground motion, as shown in Figure 3.2.2. This peak is believed to be caused by the timing failure between the PS and AS, in which case the detached AS is unable to catch up with the suddenly increased velocity of the PS as the near-field velocity pulse arrives. However, such timing failures can be avoided by making the frequency of the AS higher and choosing a finer sampling interval.

3.2.2 Attachment Time Histories

Figures 3.2.7 and 3.2.8 show 1st story attachment (or detachment) time histories of the AIC system during the first four seconds of the ELC and RRS excitations. The numbers of attachments for different control algorithms are summarized in Table 3.2.3.

It is seen that, in the initial phase of the excitation, the PS and AS are attached and detached in a similar fashion in all controlled cases. As time passes by, the PS and AS are attached and detached more frequently in the OCS and AVS algorithms. By the end of the first four seconds of excitation, there have been approximately twice as many attachments

accomplished in the OCS and AVS algorithms than in the AID algorithm. It should be noted that the best control efficiency is not achieved in the OCS algorithm which involves the most attachments. Instead, it seems that attaching less often but maintaining each attachment relatively longer works better in the AID and AVS algorithms.

Table 3.2.3: Number of attachments between the PS and AS in the 1st story under the first four seconds of ELC and RRS excitations controlled by the OCS, AID, and AVS algorithms in the NC approach

	OCS	AID	AVS
ELC	87	34	69
RRS	90	44	67

It is interesting to see that the attachment time histories for the AID case in Figure 3.2.8 (b) is highly similar to the AVS case in Figure 3.2.8 (c). A comparable control effect is accordingly noticed in Figures 3.2.5 and 3.2.7.

3.2.3 Story Drift Responses of the AS

The 1st, 4th, and 8th story drift responses of the AS are plotted in Figures 3.2.9 and 3.2.10 for the OCS algorithm. Table 3.2.4 summarizes the peak story drifts of the AS in these figures. The corresponding responses of the AS for the AID and AVS algorithms are similar to those of the PS in Figures 3.2.3 to 3.2.6 and are therefore omitted. The peak story drifts for the AID and AVS algorithms, can be obtained from Tables 3.2.1 and 3.2.2 with the aid of Equations (2.2.13) and (2.2.14). They are also compiled in Table 3.2.4 for comparison.

It is seen that the response of the AS is a combination of two sequences of motion with different frequency contents. The first sequence is a lightly damped higher frequency harmonic motion of the detached AS and the second sequence is a lower frequency motion of the attached PS and AS. Clearly, the more frequently the two sequences of motion are altered, the more frequently the PS and AS are attached, and the shorter the attach-

ments are maintained. As the two sequences are altered more frequently in the 1st story than in the 4th and 8th stories in Figures 3.2.9 and 3.2.10, one can conclude that the PS and AS are attached (or detached) more often in lower stories than in upper stories.

In the AIC algorithms, the peak story drift of the AS is proportional to the maximum control force the AS applies to the PS during the control process. The peak story drift of the AS is therefore an important parameter in the preliminary design of an AIC system. Generally speaking, to reach the same level of control effect, a more efficient AIC algorithm requires a smaller peak story drift of the AS. In this respect, the OCS algorithm would be the most efficient among the three AIC algorithms considered, as the smallest peak story drifts corresponding to the OCS algorithm are seen in Table 3.2.4.

Table 3.2.4: Maximum story drift of the AS at the 1st, 4th, and 8th stories excited by the ELC and RRS ground motions controlled by the OCS, AID, and AVS algorithms in the NC approach

	ELC			RRS		
Algorithm	1st	4th	8th	1st	4th	8th
OCS	1.56	1.02	0.58	4.09	4.23	1.96
AID	3.96	2.58	1.92	7.90	6.90	3.44
AVS	1.06	1.25	0.95	4.22	3.78	2.65

In the case of the RRS ground motion, from Equation (3.1.21), the base shear coefficients for the OCS, AID, and AVS algorithms are respectively 0.67, 1.3, and 0.70, which means that the shear forces carried by the AS in the 1st story are respectively 67%, 130%, and 70% of the building weight. This requires that the AS be designed much stiffer than the PS.

3.2.4 Absolute Acceleration Responses of the PS

As mentioned earlier, besides protecting a high-rise building from structural damage by suppressing the peak story drift response, reducing the peak absolute acceleration of the building so as to improve the comfort of the occupants is an additional control objective

of AIC. The absolute acceleration in a building also represents the amount of seismic force that the building experiences in an earthquake. For high-rise buildings, the peak absolute acceleration in the top story is often the control target. Figures 3.2.11 and 3.2.12 plot the 8th story absolute acceleration time histories of the PS. Table 3.2.5 summarizes the peak and RMS values of the corresponding response quantities.

Table 3.2.5: Peak and RMS values of the 8th story absolute acceleration of the PS excited by the ELC and RRS ground motions controlled by the OCS, AID, and AVS algorithms in the NC approach

	Uncontrolled		OCS		AID		AVS	
	Peak	RMS	Peak	RMS	Peak	RMS	Peak	RMS
ELC	1.10	0.36	0.94	0.14	1.74	0.23	1.78	0.23
RRS	2.88	1.06	3.04	0.32	2.78	0.39	4.98	0.47

The most distinguishing feature in these figures is the prominent pulse caused by the sudden attachments between the PS and AS. The peak values of the pulses in the AID and AVS cases far exceed those in the uncontrolled case, whereas the peak values of the pulses in the OCS algorithm are comparable to those in the uncontrolled case. However, the RMS values of the absolute acceleration in all controlled cases are generally smaller than the uncontrolled counterpart, as seen in Table 3.2.5. Compared to the OCS case, the pulses in the AID and AVS cases are much sharper and appear more frequently.

3.2.5 Fourier Amplitude Spectra

The effectiveness of the AIC algorithms may also be demonstrated and compared in the frequency domain. Figures 3.2.13 and 3.2.14 depict the Fourier Amplitude Spectra of the 1st, 4th, and 8th story drift responses of the PS. It is seen that all resonance peaks at modal frequencies in the uncontrolled case are greatly suppressed in all controlled cases. The controlled responses are erratic and whipsawed, especially in the high frequency range.

3.2.6 Maximum Story Drift Distribution of the PS

To give a broader view of the control result achieved by the AIC algorithms, Figure 3.2.15 presents the maximum story drift distribution of the PS along the story height. It is seen that all AIC algorithms in general are very effective in reducing the maximum story drift. For the ELC case in Figure 3.2.15 (a), approximately 50% reduction of the story drift is accomplished by all AIC algorithms. In particular, the AVS algorithm gives the largest story drift reduction in lower stories and the OCS algorithm yields the best control effect in upper stories. For the RRS case in Figure 3.2.15 (b), the response of the PS is considerably suppressed by both the AID and AVS algorithms, whereby an over 50% reduction of the story drift is accomplished at all story levels. For the OCS algorithm, larger reduction of story drift is seen in upper stories, but only minor reduction of the story drift is achieved in the 1st and 2nd stories.

3.2.7 Summary

Table 3.2.6 summarizes the qualitative performance assessments of the OCS, AID, and AVS algorithms in the NC approach for all cases examined in this section.

Table 3.2.6: Qualitative performance assessments of the OCS, AID, and AVS algorithms in the NC approach for all cases examined in Section 3.2

Algorithm	Maximum Story Drift Reduction	Absolute Acceleration Reduction
OCS	Satisfactory	Satisfactory
AID	Good	Fair
AVS	Excellent	Poor

3.3 Seismic Responses of MDOF Systems (MC Approach)

As described in Section 3.1.3, in the MC approach, the attachments and detachments between the PS and AS are established simultaneously in all stories according to the control decision made at a particular story level where the sensor is located. In most of this section, it is assumed that the sensor is installed on the 1st floor slab of the building and the control decision is made based on the measurements of the relative motion between the 1st floor slab and the ground. Results for cases in which control decisions are made at other story levels will be shown at the end of this section.

3.3.1 Story Drift Responses of the PS

Figures 3.3.1 to 3.3.6 plot the 1st, 4th, and 8th story drift responses of the PS. Table 3.3.1 gives data on the peak and RMS values of the response quantities plotted.

One can see from these figures and tables that all AIC algorithms achieve significantly improved results over the uncontrolled counterpart in terms of both peak and RMS values of story drift responses. As to the OCS algorithm, larger reduction of the story drift responses at all story levels is generally observed in the MC approach as opposed to the NC approach. For instance, for the RRS case, an almost 80% reduction of the peak 1st story drift is attained by the MC approach in Figure 3.3.2, whereas only a 20% reduction is accomplished by the NC approach in Figure 3.2.2. Regarding the AID algorithm, a slightly improved control result is achieved in the MC approach in contrast to the NC approach. The AVS algorithm, however, does not produce better control result in the MC approach as compared to the NC approach.

One can also see that the controlled responses in the MC approach are much smoother than those in the NC approach. In all controlled cases, the story drift responses in the 1st and 4th stories are mostly composed of a harmonic motion with a 1 second period. This is

expected because in the MC approach the PS and AS are attached and detached concurrently at all story levels so that the motion of the first mode is maintained and the participation of other modes is reduced.

Table 3.3.1: Peak and RMS values of the 1st, 4th, and 8th story drift responses of the PS excited by the ELC ground motion uncontrolled and controlled by the OCS, AID, and AVS algorithms in the MC approach

	1st story		4th story		8th story	
Algorithm	Peak	RMS	Peak	RMS	Peak	RMS
Uncontrolled	3.35	1.15	3.35	1.20	1.67	0.54
OCS	1.26	0.36	1.13	0.38	0.67	0.18
AID	1.15	0.39	1.50	0.40	0.92	0.19
AVS	2.10	0.62	1.42	0.59	1.15	0.39

Table 3.3.2: Peak and RMS values of the 1st, 4th, and 8th story drift responses of the PS excited by the RRS ground motion uncontrolled and controlled by the OCS, AID, and AVS algorithms in the MC approach

	1st story		4th story		8th story	
Algorithm	Peak	RMS	Peak	RMS	Peak	RMS
Uncontrolled	10.21	3.68	10.71	3.84	4.33	1.61
OCS	2.28	0.51	2.29	0.51	1.10	0.27
AID	3.71	0.67	2.43	0.59	1.04	0.27
AVS	4.48	1.02	3.74	0.96	2.28	0.63

3.3.2 Attachment Time Histories

Figures 3.3.7 and 3.3.8 show the attachment time histories of the AIC system in the 1st story during the first four seconds of the ELC and RRS excitations. Table 3.3.3 lists the total number of attachments in these figures.

It is seen from Tables 3.2.3 and 3.3.3 that there are more attachments involved in the OCS algorithm than in the AID and AVS algorithms and that there are less attachments involved in the MC approach than in the NC approach. It is interesting to note that in the

OCS algorithm, even though the total number of attachments drops significantly in the MC approach as opposed to in the NC approach, a better control effect is achieved.

Table 3.3.3: Number of attachments between the PS and AS in the 1st story under the first four seconds of ELC and RRS excitations controlled by the OCS, AID, and AVS algorithms in the MC approach

	OCS	AID	AVS
ELC	42	22	38
RRS	54	34	37

3.3.3 Story Drift Responses of the AS

The 1st, 4th, and 8th story drift responses of the AS for the OCS algorithm are displayed in Figures 3.3.9 and 3.3.10. Table 3.3.4 lists the peak values of the story drift responses in these figures. As before, the corresponding plots for the AID and AVS algorithms are omitted as the dynamics of the AS are neglected in these algorithms.

Table 3.3.4: Peak values of the 1st, 4th, and 8th story drift responses of the AS excited by the ELC and RRS ground motions uncontrolled and controlled by the OCS, AID, and AVS algorithms in the MC approach

	ELC			RRS		
Algorithm	1st	4th	8th	1st	4th	8th
OCS	1.13	0.94	0.46	3.65	3.10	1.77
AID	2.29	3.00	1.85	7.42	4.86	2.08
AVS	2.10	1.42	1.15	4.48	3.74	2.28

It is seen that the responses of the AS have identical frequency content in all stories. This indicates that the PS and AS are indeed simultaneously attached and detached in all stories. The story drifts of the AS decrease gradually from lower to upper stories. Compared to the NC approach, a slight decrease of the peak story drifts is observed in the OCS and AID algorithms, but a slight increase of the peak story drifts is found in the

AVS algorithm. For the same excitation, a smaller peak story drift of the AS corresponds to a smaller force needed to control the PS and thus indicates better control efficiency of an AIC algorithm. Hence, one can conclude that in contrast to the NC approach, the control efficiencies of the OCS and AID algorithms are improved in the MC approach, while the control efficiency of the AVS algorithm is deteriorated in the MC approach.

3.3.4 Absolute Acceleration Responses of the PS

Figures 3.3.11 and 3.3.12 depict the 8th story absolute acceleration responses of the PS. Table 3.3.5 lists the peak and RMS values of the response quantities in these figures.

Table 3.3.5: Peak and RMS values of the 8th story absolute acceleration of the PS excited by the ELC and RRS ground motions controlled by the OCS, AID, and AVS algorithms in the MC approach

	Uncontrolled		OCS		AID		AVS	
	Peak	RMS	Peak	RMS	Peak	RMS	Peak	RMS
ELC	1.10	0.36	0.86	0.16	0.88	0.18	2.15	0.47
RRS	2.88	1.06	2.77	0.30	2.58	0.35	4.27	0.75

It is seen that the absolute acceleration responses are moderately suppressed in the OCS algorithms, slightly suppressed in the AID algorithm, and magnified in the AVS algorithm. In terms of the peak and RMS values of the absolute acceleration, a better control effect is achieved by the OCS and AID algorithms but a worse control effect is attained by the AVS algorithm in the MC approach as compared to in the NC approach. It is interesting to note that for the RRS case the general appearance of the controlled responses for the MC approach case in Figures 3.3.12 is highly similar to that for the NC approach case in Figure 3.2.12.

3.3.5 Fourier Amplitude Spectra

Figures 3.3.13 and 3.3.14 plot the Fourier Amplitude Spectra of the 1st, 4th, and 8th story drift responses of the PS. It is seen that the resonance peaks found in the uncontrolled case are effectively suppressed in all controlled cases. Compared to the NC approach, greater reduction of the story drift responses is achieved in the high frequency range by both the OCS and AID algorithms in the MC approach, but several noticeable peaks are found in the high frequency range for the AVS algorithm in the MC approach.

3.3.6 Maximum Story Drift Distribution of the PS

Figures 3.3.15 to 3.3.18 show the maximum story drift distribution along the story height for the cases that the measurements and control decisions are made at the 1st, 3rd, 5th, and 8th story levels, respectively. Table 3.3.6 summarizes the number of attachments between the PS and AS in the first four seconds of ELC and RRS excitations.

Table 3.3.6: Number of attachments between the PS and AS in the first four seconds of the ELC and RRS excitations controlled by the OCS, AID, and AVS algorithms in the MC approach (control decisions are made in the 1st, 3rd, 5th, and 8th stories)

	ELC				RRS			
Algorithm	1st	3rd	5th	8th	1st	3rd	5th	8th
OCS	42	214	48	14	54	164	46	33
AID	22	19	18	23	34	27	22	25
AVS	38	22	21	28	37	30	30	28

It is seen that in the OCS algorithm, the best location to measure the relative motion between the PS and AS and to make control decision is clearly at the 1st story level. Comparing Figure 3.3.15 with Figure 3.2.15, it is seen that the OCS algorithm in the MC approach overcomes the control deficiency in lower stories in the NC approach and sig-

nificantly reduces the maximum story drift in all stories. In fact, Figure 3.3.15 achieves the best overall control effect in all AIC algorithms and approaches examined so far in this chapter.

The worst control effect achieved by the OCS algorithm is found in Figure 3.3.16 corresponding to the case that the measurements and control decisions are made at the 3rd story level. Note that the 3rd story is very close to the anti-node of the 2nd mode for the 8-story shear building studied in this chapter. Thus, it is believed that spill-over effect has actually occurred in this case where the attachments between the PS and AS significantly excite the 2nd mode of the shear building. The large number of attachments between the PS and AS found in Table 3.3.6 provides more evidence of the participation of higher modes. It is interesting to note that in Figures 3.3.17 and 3.3.18 the controlled results almost match the uncontrolled ones for the cases in which the measurement and control decisions are made at the 5th and 8th story levels.

As seen in Figures 3.3.15 to 3.3.18, the AID algorithm yields very consistent control efficiency for all cases in which the measurements and control decisions are made at different story levels.

The AVS algorithm, on the other hand, is very sensitive to which story level the measurements and control decisions are made. Figures 3.3.15 to 3.3.18 show that the AVS algorithm moderately and slightly reduces the maximum story drift for the cases in which the measurements and control decisions are made at the 1st and 8th story levels, respectively. However, instability takes place in the cases that the measurements and control decisions are made at the 3rd and 5th story levels. For this reason, the maximum story drift distributions for the AVS algorithm are not shown in Figures 3.3.16 (a) and 3.3.17 (b).

Table 3.3.7 provides the qualitative performance assessments for the cases in which the measurements and control decisions are made at the 1st, 3rd, 5th, and 8th story levels.

Table 3.3.7: Qualitative performance assessment of the OCS, AID, and AVS algorithms in the MC approach for the cases that the measurements and control decisions are made at the 1st, 3rd, 5th, and 8th story levels

Algorithm	1st story	3rd story	5th story	8th story
OCS	Excellent	Unstable	Fair	Fair
AID	Good	Good	Good	Good
AVS	Satisfactory	Unstable	Unstable	Fair

3.3.7 System Uncertainties

In the MC approach, it is assumed that the frequencies of the AS at all story levels are tuned to the same value (25.6 Hz for the 8-story shear building) so that an identical control decision is likely to be reached in all stories simultaneously in each sampling interval. The PS and AS are thus attached or detached at all story levels concurrently according to the control decision for any one story where the sensor is located and the state variables are measured.

However, in order to tune the frequencies of the AS to the same value, the mass and stiffness of the AS must be adjusted accurately, which, in practice, may be hard to realize. It is the purpose of this subsection to investigate how AIC algorithms are affected by the errors introduced uncertainties in the mass and stiffness of the AS. Such analyses are performed by computing the story drift response of the 8-story shear building for various cases (20 cases total) in which the deviation from nominal values of the mass and stiffness of the AS in each story are randomly assigned (uniform distribution) between 0 and 10%. Figures 3.3.19 and 3.3.20 plot the mean values of the maximum story drift distribution of the 8-story shear building. Tables 3.3.8 and 3.3.9 give data on the mean values and standard deviations of the maximum story drift.

Figures 3.3.19 and 3.3.20 and Table 3.3.8 show that AIC algorithms are slightly sensitive or moderately sensitive to uncertainties in the mass and stiffness of the AS, respectively. Comparing the AID and AVS algorithms, the OCS algorithm is more sensi-

tive to measurement uncertainties, especially to the uncertainties in the stiffness of the AS in Figure 3.3.20 (b). Degradation in the system response is generally observed when system uncertainties are introduced in the system.

Table 3.3.8: Mean values ($\bar{x}$) and standard deviations (σ) of the maximum story drift of the 8-story shear building excited by the ELC and RRS ground motions and controlled by the OCS, AID, AVS algorithms in the MC approach for cases in which uncertainties in the mass of the AS are randomly assigned between 0 and 10%

Story	ELC						RRS					
	OCS		AID		AVS		OCS		AID		AVS	
	$\bar{x}$	σ	$\bar{x}$	σ	$\bar{x}$	σ	$\bar{x}$	σ	$\bar{x}$	σ	$\bar{x}$	σ
8	0.66	0.10	0.92	0.01	1.12	0.04	1.47	0.44	1.09	0.01	2.30	0.17
7	0.97	0.15	1.40	0.01	1.55	0.12	2.02	0.56	1.81	0.01	3.09	0.14
6	1.14	0.19	1.62	0.01	1.70	0.08	2.41	0.69	2.18	0.00	3.49	0.13
5	1.11	0.19	1.65	0.01	1.64	0.05	2.64	0.79	2.17	0.00	3.27	0.17
4	1.04	0.16	1.50	0.01	1.49	0.01	2.80	1.00	2.43	0.00	3.73	0.04
3	1.03	0.15	1.31	0.01	1.51	0.10	2.84	1.02	2.84	0.00	4.21	0.03
2	1.04	0.16	1.18	0.06	1.72	0.15	3.00	1.08	3.34	0.00	4.49	0.03
1	0.99	0.14	1.16	0.05	1.80	0.20	3.02	1.02	3.72	0.00	4.51	0.04

Table 3.3.9: Mean values ($\bar{x}$) and standard deviations (σ) of the maximum story drift of the 8-story shear building excited by the ELC and RRS ground motions and controlled by the OCS, AID, AVS algorithms in the MC approach for cases in which uncertainties in the stiffness of the AS are randomly assigned between 0 and 10%

Story	ELC						RRS					
	OCS		AID		AVS		OCS		AID		AVS	
	$\bar{x}$	σ	$\bar{x}$	σ	$\bar{x}$	σ	$\bar{x}$	σ	$\bar{x}$	σ	$\bar{x}$	σ
8	0.66	0.13	0.92	0.07	1.12	0.14	1.47	0.44	1.09	0.09	2.30	0.49
7	0.97	0.23	1.40	0.06	1.55	0.10	2.02	0.85	1.81	0.09	3.09	0.49
6	1.14	0.26	1.62	0.04	1.70	0.11	2.41	1.16	2.18	0.06	3.49	0.34
5	1.11	0.22	1.65	0.03	1.64	0.08	2.64	1.31	2.17	0.05	3.27	0.27
4	1.04	0.21	1.50	0.03	1.49	0.07	2.80	1.50	2.43	0.08	3.73	0.16
3	1.03	0.20	1.31	0.04	1.51	0.07	2.84	1.76	2.84	0.07	4.21	0.14
2	1.04	0.23	1.18	0.05	1.72	0.11	3.00	1.76	3.34	0.09	4.49	0.15
1	0.99	0.18	1.16	0.04	1.80	0.13	3.02	1.63	3.72	0.07	4.51	0.19

3.3.8 Summary

Table 3.3.10 summarizes the qualitative performance assessments of the OCS, AID, and AVS algorithms in the MC approach for all cases examined in this section.

Table 3.3.10: Qualitative performance assessments of the OCS, AID, and AVS algorithms in the MC approach for all cases examined in Section 3.3

Algorithm	Maximum Story Drift Reduction	Absolute Acceleration Reduction
OCS	Excellent	Good
AID	Good	Good
AVS	Satisfactory	Poor

3.4 Parametric Studies

3.4.1 Sequence of Analyses

In Sections 3.2 and 3.3, the efficiencies of the OCS, AID, and AVS algorithms in the NC and the MC approaches were assessed based on the seismic response of an 8-story shear building. To investigate these control algorithms and approaches from a broader perspective, this section examines the seismic responses of various AIC systems in terms of the number of stories, and the mass, damping, and stiffness of the AS.

In this section, the structure (PS) to which the AIC is applied is also an N-story shear building. Note that the structural parameters of the N-story shear building are fully deterministic if the number of stories, N, is specified. The parameters to be studied are the number of stories, N, the mass, damping, and stiffness of the AS relative to those of the PS, α, β, and γ. In each of the parametric studies, only the effect of one parameter (denoted by x) is assessed while the rest remain their nominal values. Table 3.4.1 shows the sequence of the analyses and nominal values of related parameters.

In the AID and AVS algorithms, the dynamics of the AS are neglected and the AS is assumed to relax back to its initial zero position immediately after a detachment. Therefore, the mass and damping of the AS have little effect on the PS response. However, a larger stiffness of the AS in these algorithms will facilitate larger energy transfer from the PS to the AS, as demonstrated in Tables 2.2.1 to 2.2.4. The effects of the mass, damping, and stiffness of the AS for the AID and AVS algorithms are omitted in this study.

Table 3.4.1: Sequence of analyses and nominal values of related parameters

Analysis	N	α	β	γ
1	x	10%	1	2
2	8	x	1	2
3	8	10%	x	2
4	8	10%	1	x

The values of variable, x, in each analysis are listed as follows:

Analysis 1: Effect of the number of stories: $N = 4, 8, 12, 16, 20$

Analysis 2: Effect of the mass of the AS: $\alpha = 5, 10, 15, 20\%$

Analysis 3: Effect of the damping of the AS: $\beta = 1, 5, 10, 20$ or $\zeta_{2i} = 2, 10, 20, 40\%$

Analysis 4: Effect of the stiffness of the AS: $\gamma = 0.5, 1, 2, 4$

3.4.2 Effect of Number of Stories

Figures 3.4.1 and 3.4.2 plot the maximum story drift responses verses the number of stories or the Story Drift Spectra (SDS) of the PS uncontrolled and controlled by the OCS, AID, and AVS algorithms in the NC and the MC approaches. Each of these figures is divided into two subfigures: (a) and (b), corresponding to the cases in which the AIC system is excited by the ELC and RRS ground motions.

In the NC approach, Figure 3.4.1 clearly shows that the AVS algorithm is the most effective in reducing the maximum story drift for buildings with story numbers ranging from 4 to 20. The OCS and AID algorithms are effective in reducing the story drift for buildings below 12 stories. The OCS algorithm does not yield satisfactory control result for buildings above 12 stories.

In the MC approach, it is seen from Figure 3.4.2 that both the OCS and AID algorithms achieve significantly reduced maximum story drift for buildings ranging from 4 to 12 stories. The AVS algorithm, however, only moderately reduces the maximum story drift for buildings in the lower story range.

After careful comparison, it can be seen that the SDS obtained from the SDOF models in Figure 2.4.1 have a similar shape to those obtained from the MDOF models in Figures 3.4.1 and 3.4.2. However, in terms of the maximum story drift, the former SDS are approximately one half of the latter SDS. This suggests that the hypothetical sinusoidal mode shape assumed in the SDOF model generally underestimates the actual story drift distribution in a MDOF system by 50%.

3.4.3 Effect of Mass of the AS

For the OCS algorithm, the effects of the mass, damping, and stiffness of the AS on the story drift response of the PS are respectively shown in subfigures (a), (b), and (c) of Figures 3.4.3 to 3.4.6, which plot the SDS for buildings ranging from 4 to 20 stories.

It is seen from Figures 3.4.3 (a) to 3.4.6 (a) that the maximum story drift generally decreases with the decrease of the mass of the AS. This is what one would expect since after a detachment a lighter AS can vibrate back to its opposite position to facilitate a reattachment to the PS in a more timely fashion, resulting in more vibrational energy being withdrawn from the PS to the AS.

It is also seen that the response curves in these figures are smooth and flat, which indicates that the mass of the AS has uniform effect on the story drift response for buildings in a wide story range. Although no computation has been performed for buildings with more than 20 stories, it is reasonable to infer from these available figures that the mass of the AS will have comparable effect on story drift response for taller buildings. In contrast to the NC approach, the maximum story drift response in the MC approach is more sensitive to the mass of the AS.

3.4.4 Effect of Damping of the AS

Figures 3.4.3 (b) to 3.4.6 (b) generally show that high damping in the AS does not have a positive effect on reducing the maximum story drift response of the PS. During the control process in the OCS algorithm, besides the brief turnaround between two attachments, the AS is mostly attached to the PS. Because the mass of the PS is much larger than that of the AS, the damping of the AS will not affect the motion of the attached PS and AS materially. Thus, adding damping to the AS will only reduce the motion of the detached AS. This is not desirable in AIC systems, because a reduced amplitude of the AS will limit the magnitude of the control force that the AS exerts on the PS.

3.4.5 Effect of Stiffness of the AS

It is seen from Figures 3.4.3 (c) to 3.4.6 (c) that a stiffer AS is generally effective in reducing the maximum story drift for buildings with less than 12 stories. However, the degree of reduction is less prominent than in the SDOF system in Chapter 2. It is also seen that increasing the stiffness of the AS can no longer further reduce the story drift for buildings with more than 12 stories, especially in the MC approach. The reason for this phenomenon is not completely clear. One possible reason is that more higher modes have been excited by the interaction between the PS and a stiffer AS.

3.5 Practical Issues

3.5.1 Sampling Interval

Section 2.5.1 showed that in the SDOF systems the OCS algorithm is more sensitive to the sampling interval than are the AID and AVS algorithms. The impact velocity between

the PS and AS in the OCS algorithm is proportional to the length of the sampling interval and the square of the frequency of the PS.

As a continuation, this subsection examines how the sampling interval influences the control efficiency of different AIC algorithms and approaches for MDOF systems. Since the control objective is to minimize the maximum story drift, the effect of sampling interval is studied by computing and comparing the maximum story drift responses corresponding to different sampling intervals for the 8-story shear building described in Section 3.1.5. The simulation results are displayed in Figures 3.5.1 to 3.5.4, each of which is divided into three subfigures: (a), (b), and (c), corresponding to the cases that the AIC system is controlled by the OCS, AID, and AVS algorithms, respectively.

Figures 3.5.1 and 3.5.2 show the maximum story drift distribution of the 8-story shear building controlled by the OCS, AID, and AVS algorithms in the NC approach. It is seen that the sampling interval significantly affects the control results of all AIC algorithms. The OCS algorithm is affected to the greatest degree. Generally speaking, the maximum story drift decreases with finer sampling interval. The story drift responses tend to converge faster with decreasing of sampling interval in the RRS case than the ELC case.

The sensitivity of an AIC algorithm to the sampling interval may be evaluated from the maximum allowable sampling interval defined in the Section 2.5.1. Seen from Figures 3.5.1 and 3.5.2, the corresponding maximum allowable sampling intervals for the OCS, AID, and AVS algorithms are 0.001, 0.002, and 0.005 seconds, respectively.

Figures 3.5.3 and 3.5.4 plot the maximum story drift distribution of the 8-story shear building controlled by the OCS, AID, and AVS algorithms in the MC approach. It is seen that the OCS algorithm in the MC approach is much more sensitive to the sampling interval than in the NC approach, as the story drift responses decrease markedly with the decreasing of sampling interval. In contrast, the effectiveness of the AID and AVS algorithms is less influenced by the sampling interval in the MC approach than in the NC approach. The maximum allowable sampling intervals for the OCS, AID, and AVS algorithms are 0.001, 0.01, and 0.01 seconds, respectively.

Table 3.5.1 summarizes the maximum allowable sampling intervals for the OCS, AID, and AVS algorithms in the NC and MC approaches.

Table 3.5.1: Maximum allowable sampling intervals (in seconds) for the OCS, AID, and AVS algorithms in the NC and MC approaches

	OCS Algorithm	AID Algorithm	AVS Algorithm
Nodal Control Approach	0.001	0.002	0.005
Modal Control Approach	0.001	0.01	0.01

As mentioned in Section 2.5.1, the rapid motion of the AS should be the focus in determining the maximum sampling period in the OCS algorithm. For the 8-story shear building examined in this subsection, the natural frequency of the AS in each story is tuned to 25.6 Hz. Therefore, the maximum allowable sampling frequency would roughly be $20 \times 25.6 \cong 500$ Hz, which corresponds to a sampling interval of 0.002 second. However, the numerical simulation results of Table 3.5.1 suggest that an even finer sampling interval, say 0.001 second, is probably needed in the OCS algorithm. In spite of this, it is noted that the characteristics of the story drift distributions in Figures 3.5.1 to 3.5.4 remain unchanged for different lengths of sampling intervals. Hence, the simulation results obtained earlier in this chapter using sampling intervals of 0.004 (ELC case) and 0.005 (RRS case) seconds are still adequate for a qualitative assessment of the OCS algorithm, although more accurate quantitative results could be obtained by employing finer sampling interval, say 0.001 second.

3.5.2 Time Delay

This subsection investigates how time delays affect the performance of AIC algorithms in MDOF systems. For the 8-story shear building described in Section 2.5.1, it is assumed that time delays at all story levels are 1) of the same duration, and 2) constant multiples of the sampling interval.

Simulation results for time delays of 0 (no time delay), 0.02, 0.04, 0.06 and 0.08 seconds are shown in Figures 3.5.5 to 3.5.8. Each of these figures is divided into three subfigures: (a), (b), and (c), corresponding to the cases that the AIC system is controlled by the OCS, AID, and AVS algorithms, respectively. To facilitate easier comparison, the responses are not plotted for the cases in which instabilities actually occur. Due to space limitation, only simulation results obtained from the ELC ground motion are presented.

NC Approach

Figures 3.5.5 and 3.5.6 display the 1st story drift responses and SDS of the PS controlled by the AIC algorithms in the NC approach with and without time delays.

In the OCS algorithm, severe deterioration is seen in Figures 3.5.5 (a) and 3.5.6 (a) for time delays of 0.02 and 0.04 seconds. Instabilities actually take place in the cases when the time delay exceeds 0.06 second (not shown). It should be noted that time delays in SDOF systems have caused degradation but not instability in the OCS algorithm. In the NC approach, it is believed that the delayed attachments and detachments between the PS and AS in one story have not only aggravated the response of the current story level but also spilled over to other story levels.

In the AID algorithm, the responses of the 8-story shear building remain robust with respect to short time delays, as all controlled responses in Figure 3.5.5 (b) are only slightly deteriorated by time delays. Figure 3.5.6 (b), however, shows that instability does take place for buildings with more than 12 stories when the time delay exceed 0.08 second.

Figures 3.5.5 (c) and 3.5.6 (c) show that the AVS algorithm is extremely sensitive to time delays in MDOF systems. Instability is observed in all cases when the time delay exceeds 0.02 second.

MC Approach

Figures 3.5.7 and 3.5.8 show the 1st story drift responses and SDS of the PS controlled by the AIC algorithms in the MC approach with and without time delays.

In the OCS algorithm, deteriorated but stable responses are observed in Figure 3.5.7 (a) for the 8-story shear building. However, instability occurs in buildings less than 8 and more than 16 stories when time delay reaches 0.04 second, as shown in Figure 3.5.8 (a).

In the AID algorithm, all responses in Figures 3.5.7 (b) and 3.5.8 (b) remain stable. In particular, the deterioration of responses for time delays of 0.02 and 0.04 seconds are barely distinguishable.

In the AVS algorithm, stable response is only found in 8- to 16-story buildings for a time delay of 0.02 second, as shown in Figures 3.5.7 (c) and 3.5.8 (c). Instabilities take place in all other cases.

Summary

The robustness of an AIC algorithm with respect to time delay may be evaluated by the critical time delay defined in Section 2.5.2. Table 3.5.2 summaries the critical time delays in the OCS, AID, and AVS algorithms in the NC and MC approaches for the 8-story shear building. Table 3.5.3 gives the general qualitative performance assessments for these control algorithms and approaches in the presence of time delays.

Table 3.5.2: Critical time delays (in seconds) in the OCS, AID, and AVS algorithms in the NC and MC approaches for the 8-story shear building

	OCS Algorithm	AID Algorithm	AVS Algorithm
Nodal Control Approach	0.04	> 0.08	0.02
Modal Control Approach	> 0.08	> 0.08	0.04

Table 3.5.3: Qualitative assessments of the robustness of the OCS, AID, and AVS algorithms in the NC and the MC approaches in the presence of time delays

	OCS Algorithm	AID Algorithm	AVS Algorithm
Nodal Control Approach	Not robust	Robust	Not robust at all
Modal Control Approach	Slightly robust	Robust	Not robust at all

3.5.3 Time Delay Compensation

Since Equation (2.1.9) is already expressed in matrix form which holds for MDOF systems, the predictive time delay compensation scheme for SDOF systems described in Section 2.5.3 can be applied likewise to MDOF systems. Note that in Step 3 of the predictive scheme, control decisions should be made at all story levels in MDOF systems.

The compensated results for cases examined in Section 3.5.2 are plotted in Figures 3.5.9 to 3.5.12. Each of these figures is also divided into three subfigures: (a), (b), and (c), corresponding to the OCS, AID, and AVS algorithms, respectively. The responses are not shown for the cases in which instabilities occur.

NC Approach

Figures 3.5.9 and 3.5.10 display the compensated result corresponding to the cases in Figures 3.5.5 and 3.5.6.

In the OCS algorithm, one can see from Figures 3.5.9 (a) and 3.5.10 (a) that the delayed responses for time delays of 0.02 and 0.04 seconds are improved by the predictive scheme. In particular, the compensated response for time delay of 0.02 second almost matches the response without time delay. The response for time delay of 0.04 second in Figure 3.5.5 (a) eventually becomes unstable at the end of the ELC excitation, whereas stable but degraded compensated response is found in Figure 3.5.11 (a). However, the predictive scheme is generally not effective in compensating time delays longer than 0.04 second.

In the AID algorithm, Figures 3.5.9 (b) and 3.5.10 (b) show that the predictive scheme shows competence in compensating time delays less than 0.04 seconds.

The predictive scheme very effectively compensates time delays in the AVS algorithm, as shown in Figures 3.5.9 (c) and 3.5.10 (c). In all cases examined, the compensated responses closely match the non-delayed responses.

MC Approach

Figures 3.5.11 and 3.5.12 plot the compensated result corresponding to the cases in Figures 3.5.7 and 3.5.8.

Figures 3.5.11 (a) and 3.5.12 (a) show that the predictive scheme is not effective in compensating time delays in the OCS algorithm, as the compensated responses generally become more deteriorated after compensation.

Figures 3.5.11 (b) and 3.5.12 (b) show that the predictive scheme is very effective in compensating time delays in the AID algorithm, although there is no need to compensate the slightly deteriorated non-delayed responses in these cases.

Figures 3.5.11 (c) and 3.5.12 (c) show that time delays in the AVS algorithm are effectively compensated by the predictive scheme for the MC approach. Only slight deterioration in the system responses is observed.

Summary

The effectiveness of the predictive scheme on an AIC algorithm may be evaluated by the longest time delay defined in Section 3.5.3. Table 3.5.4 summaries the longest time delays effectively compensated by the predictive scheme in the OCS, AID, and AVS algorithms in the NC and MC approaches for the 8-story shear building. Table 3.5.5 gives the qualitative performance assessments of the compensation effectiveness of the predictive scheme on the AIC control algorithms and approaches in the presence of time delays.

Table 3.5.4: Longest time delays (in seconds) compensated by the predictive scheme in the OCS, AID, and AVS algorithms in the NC and MC approaches for the 8-story shear building

	OCS Algorithm	AID Algorithm	AVS Algorithm
Nodal Control Approach	0.02	0.04	> 0.08
Modal Control Approach	0.02	0.08	> 0.08

Table 3.5.5: Qualitative assessments of the compensation effectiveness of the predictive scheme on the OCS, AID, and AVS algorithms in the NC and the MC approaches

	OCS Algorithm	AID Algorithm	AVS Algorithm
Nodal Control Approach	Fair	Fair	Excellent
Modal Control Approach	Poor	Good	Excellent

3.6 Conclusions

This chapter carries out a comprehensive study on the response of MDOF AIC systems under earthquake ground motions. Based on the analytical and numerical results obtained in the preceding sections, the following conclusions are drawn:

1. Use of either the NC or MC approaches can substantially reduce the number of configurations needed to be examined in each sampling interval. For an N-story building, the reduction is from 2^N to $2N$ and 2 for the NC and MC approaches, respectively.
2. Of the three AIC algorithms examined in MDOF systems, no single algorithm gives the best overall control efficiency in both NC and the MC approaches. In terms of reducing the maximum story drift, the OCS algorithm achieves the best control effectiveness in the MC approach, the AID algorithm gives the second best control results in both the NC and the MC approaches, and the AVS algorithm yields the best control efficiency in the NC approach. In terms of reducing the maximum absolute acceleration at the top floor of the building, the OCS and AID algorithms performed better than the AVS algorithm in both NC and the MC approaches. In the MC approach, the best control result is found in the case in which the measurement and control decision are both made at the 1st story level of the building.
3. An AS with a smaller mass, a smaller damping, and a larger stiffness is more effective in controlling the response of the PS. However, the effects of the mass, damping, and stiffness of the AS are less noteworthy in MDOF systems than in SDOF systems.

4. The OCS algorithm is much more sensitive to the sampling interval than the AID and AVS algorithms. A finer sampling interval is often needed in the MC approach than in the NC approach. Since the OCS algorithm is sensitive to high frequency motion, relatively better control effect is obtained in the RRS case than in the ELC case for the OCS algorithm.

5. In contrast to the NC approach, the robustness of AIC algorithms with respect to time delays in MDOF systems are improved in the MC approach. Compared to the system performance in SDOF systems, more deterioration and instability are observed in MDOF systems. The AID algorithm is more robust than the OCS and AVS algorithms with respect to time delays in MDOF systems.

6. The predictive scheme shows great promise in compensating time delays for the AVS algorithm in both NC and MC approaches, and for the AID algorithm in the MC approach. However, it is only effective in compensating short time delays (0.02 and 0.04 seconds) for the OCS algorithm in the NC and MC approaches.

7. The control results obtained from SDOF AIC systems in Chapter 2 provide a good qualitative approximation of the dynamic behavior of MDOF AIC systems. However, the hypothetical sinusoidal mode shape assumed in the SDOF model generally underestimates the actual story drift distribution in MDOF systems.

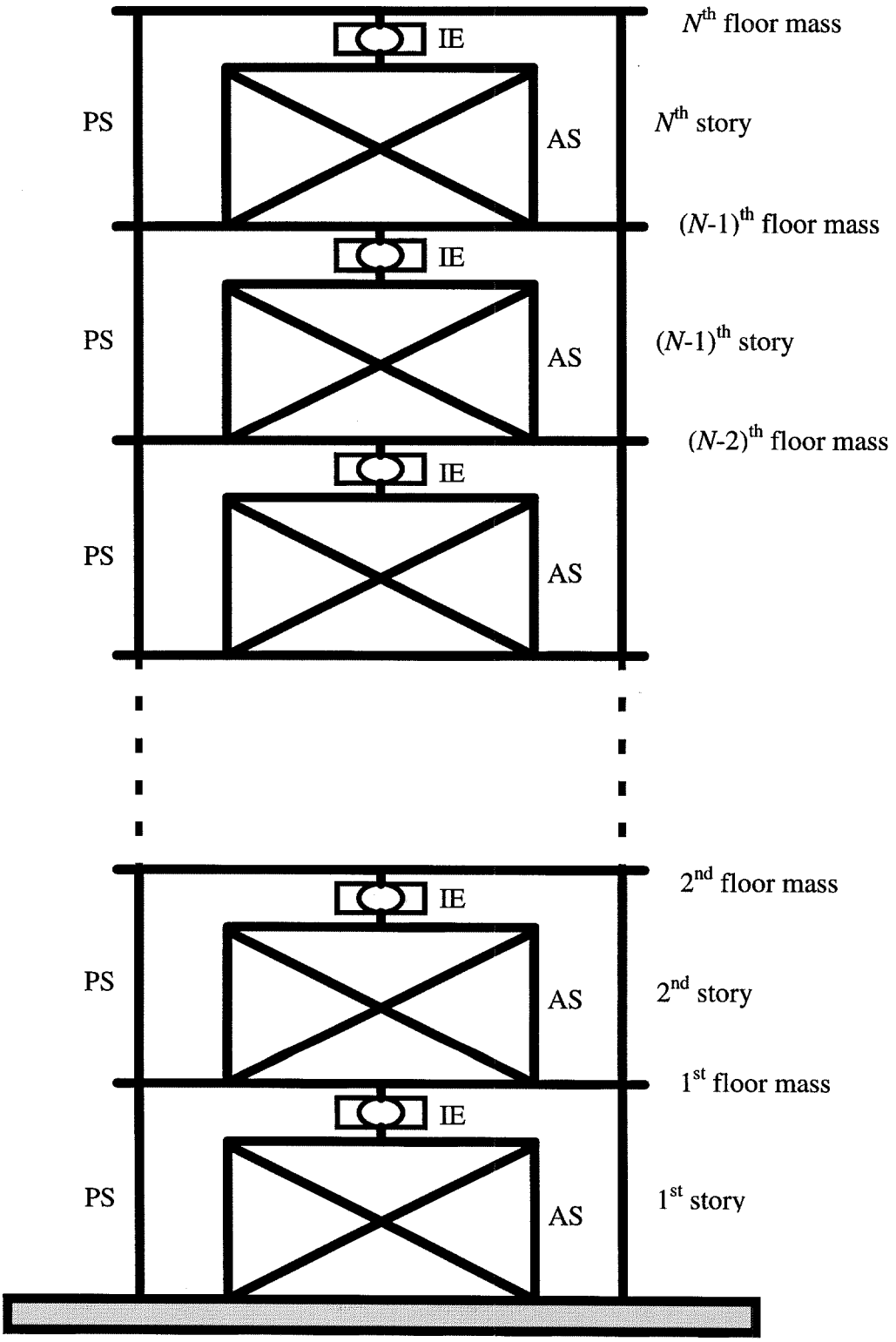

Figure 3.1.1: Schematic representation of a MDOF AIC system

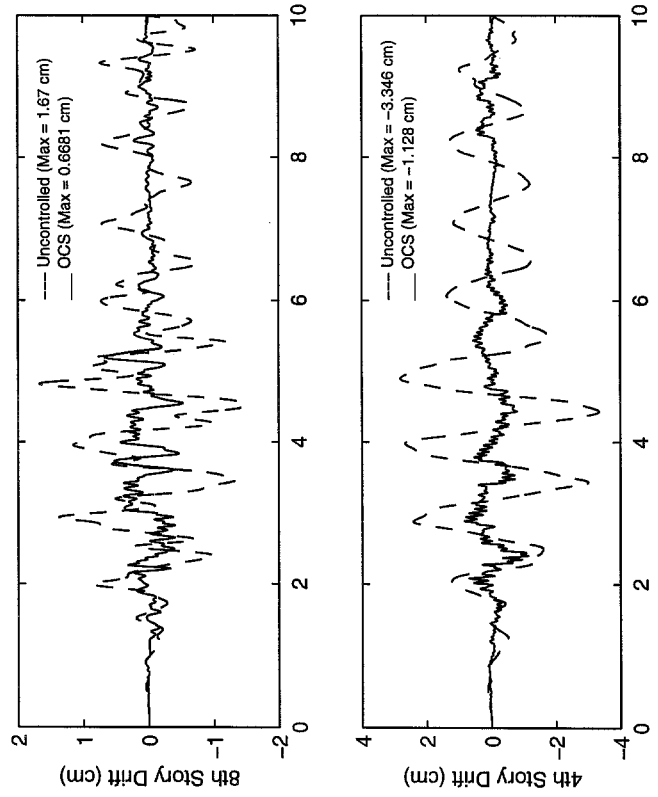

Figure 3.2.1: 1st, 4th, and 8th story drift responses of the PS excited by the ELC ground motion uncontrolled and controlled by the OCS algorithm in the NC approach

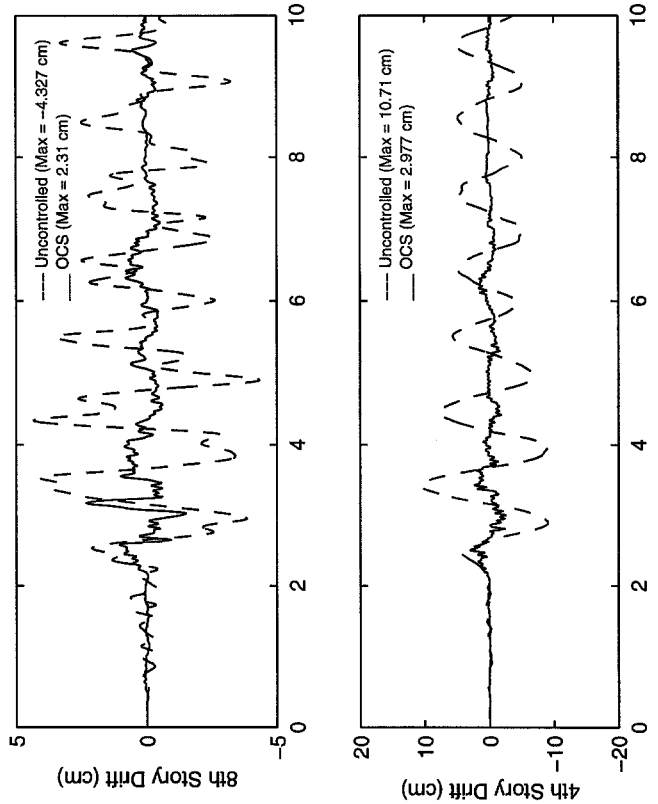

Figure 3.2.2: 1st, 4th, and 8th story drift responses of the PS excited by the RRS ground motion uncontrolled and controlled by the OCS algorithm in the NC approach

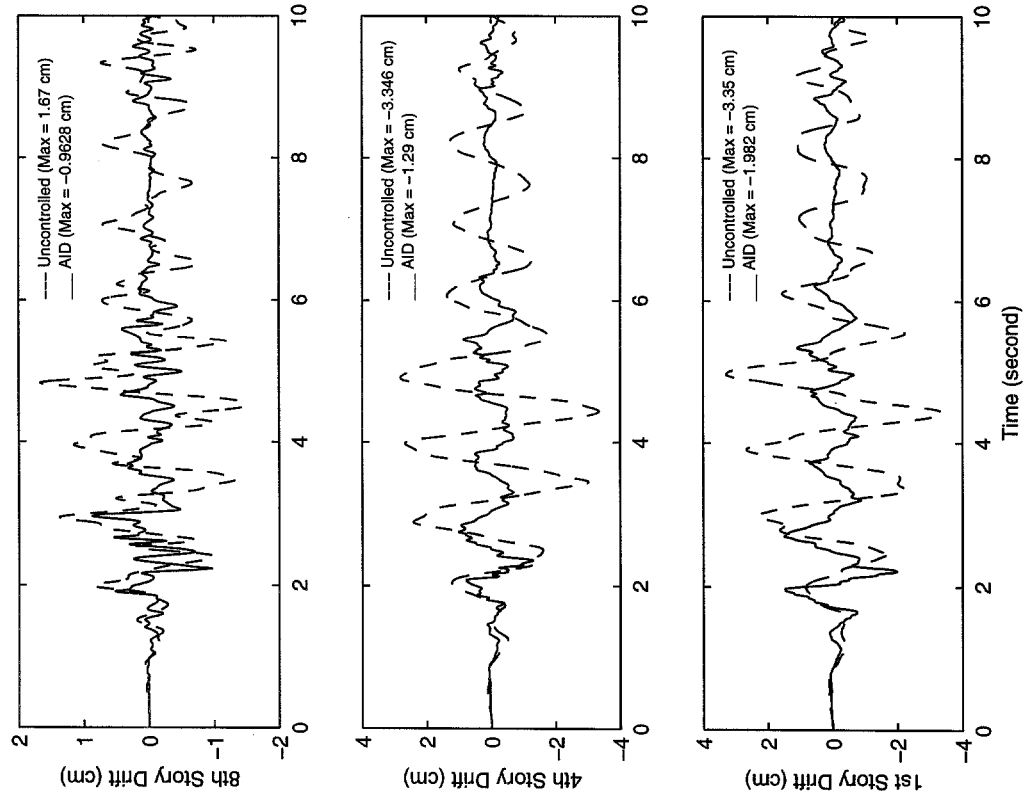

Figure 3.2.3: 1st, 4th, and 8th story drift responses of the PS excited by the ELC ground motion uncontrolled and controlled by the AID algorithm in the NC approach

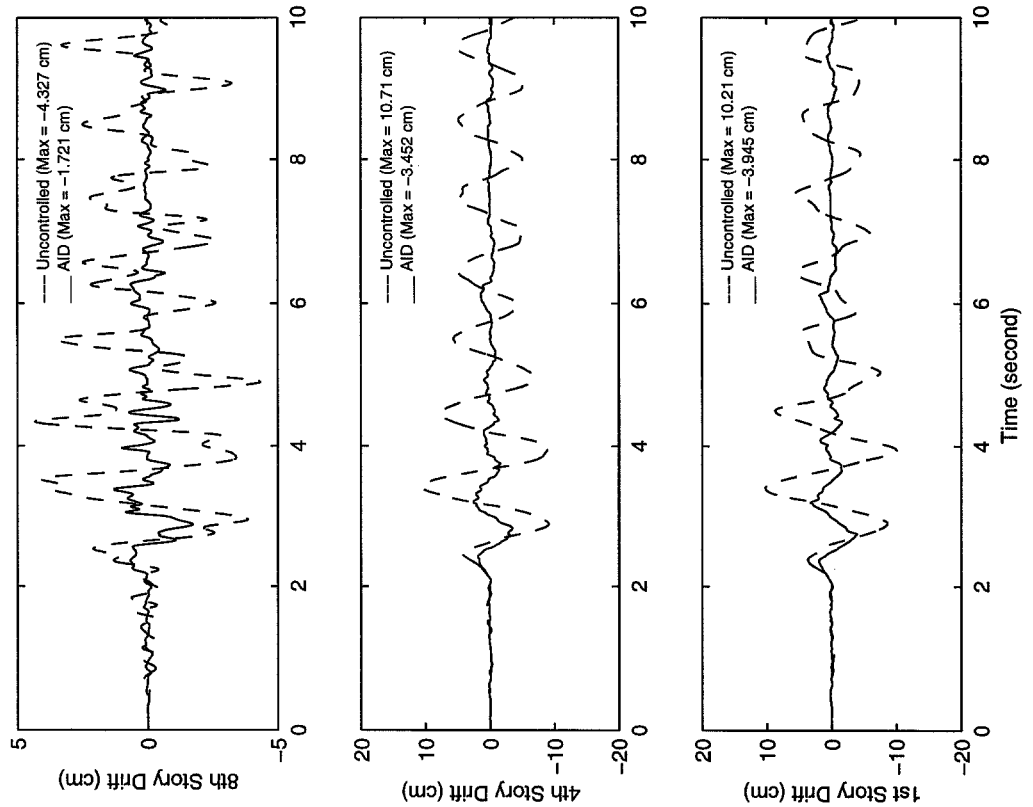

Figure 3.2.4: 1st, 4th, and 8th story drift responses of the PS excited by the RRS ground motion uncontrolled and controlled by the AID algorithm in the NC approach

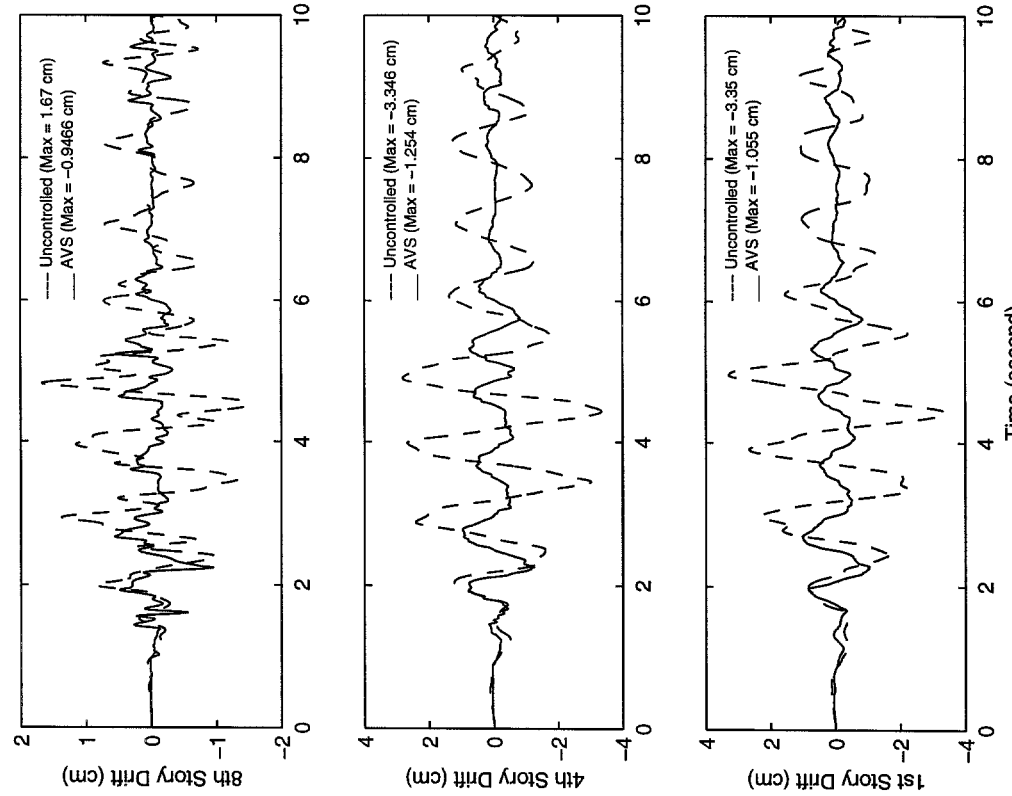

Figure 3.2.5: 1st, 4th, and 8th story drift responses of the PS excited by the ELC ground motion uncontrolled and controlled by the AVS algorithm in the NC approach

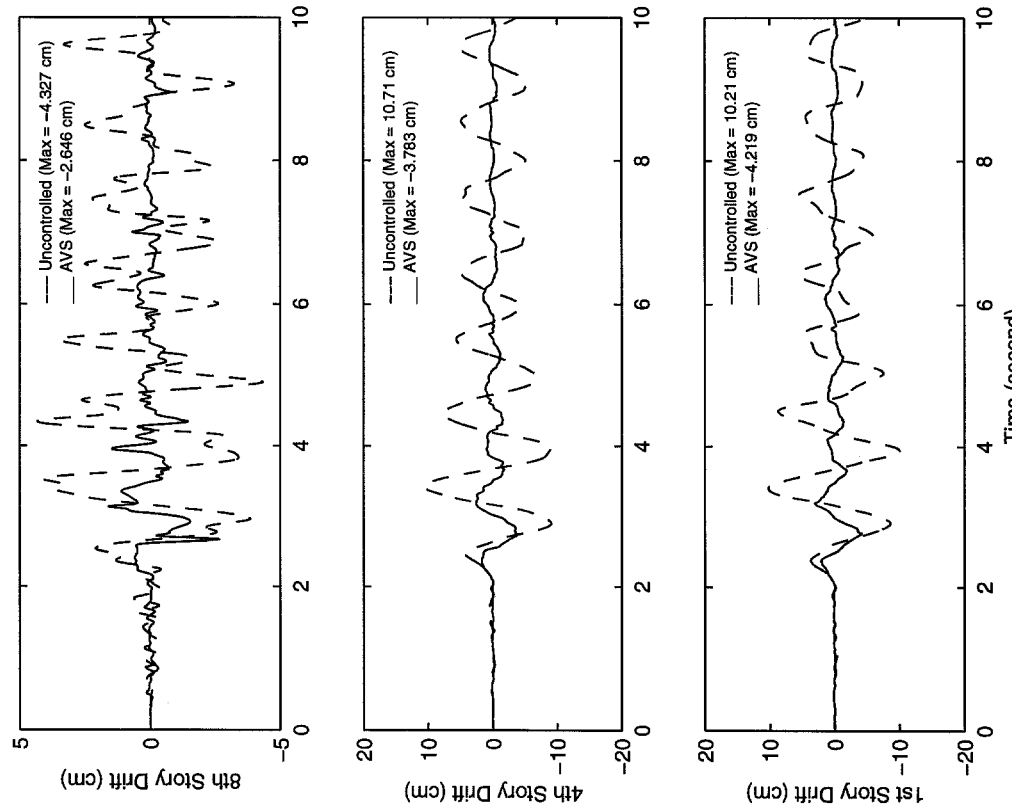

Figure 3.2.6: 1st, 4th, and 8th story drift responses of the PS excited by the RRS ground motion uncontrolled and controlled by the AVS algorithm in the NC approach

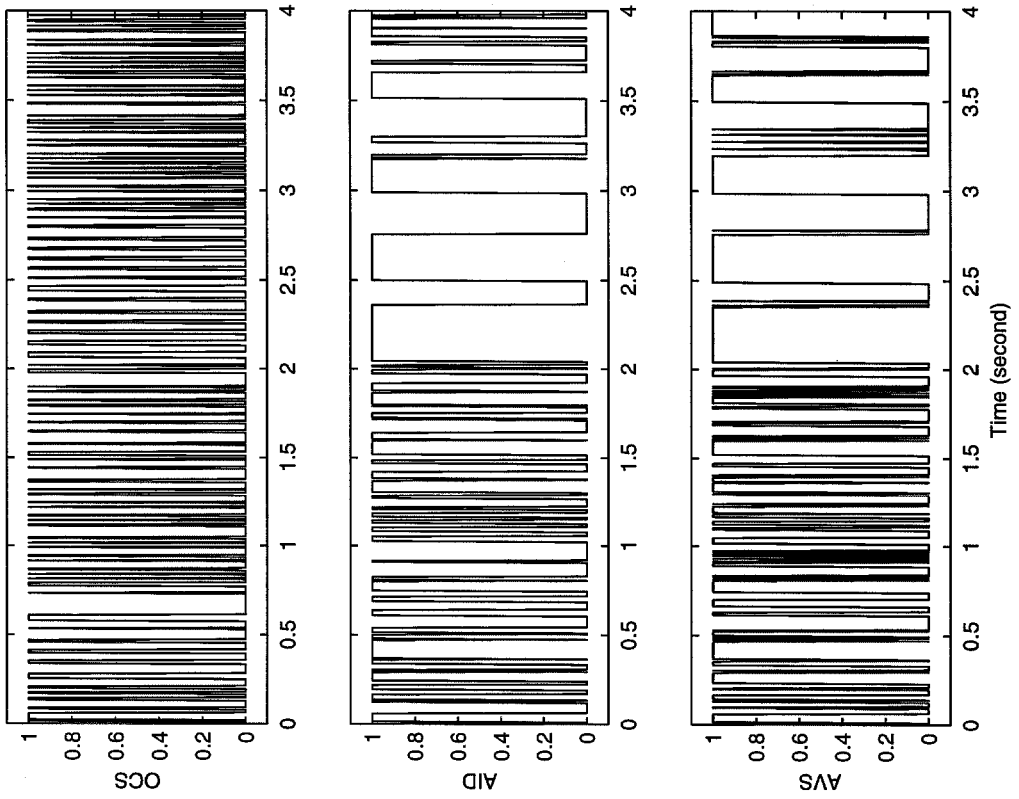

Figure 3.2.7: 1st story attachment time histories of the PS excited by the ELC ground motion controlled by the OCS, AID, and AVS algorithms in the NC approach

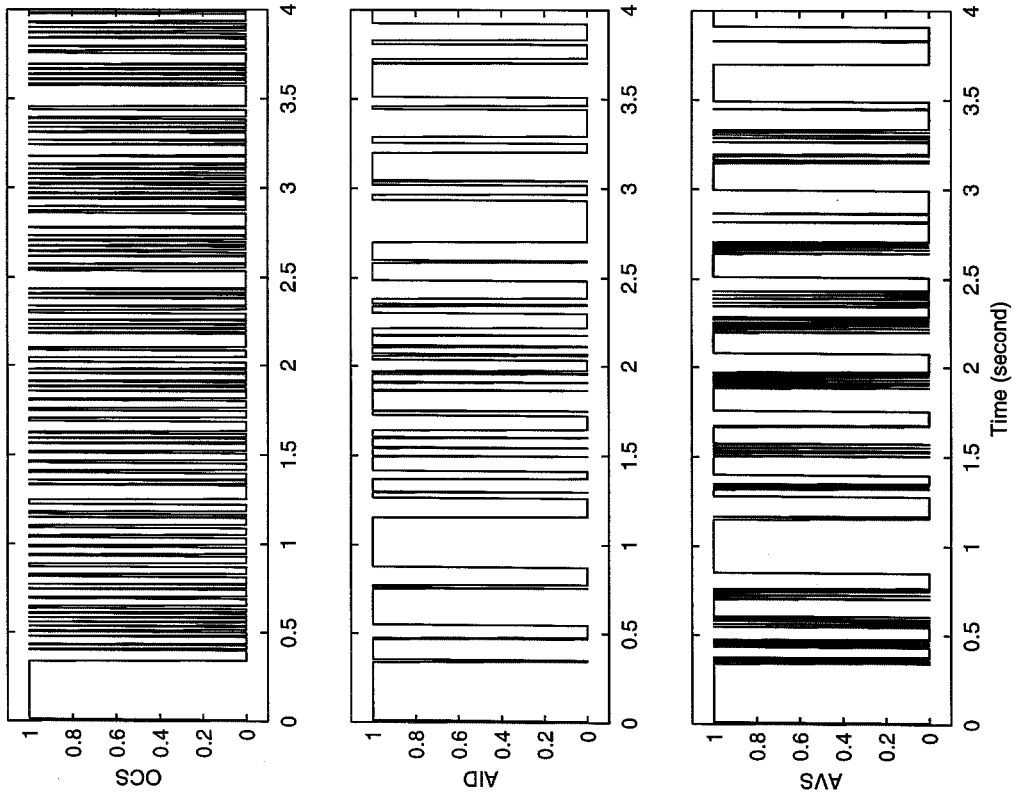

Figure 3.2.8: 1st story attachment time histories of the PS excited by the RRS ground motion controlled by the OCS, AID, and AVS algorithms in the NC approach

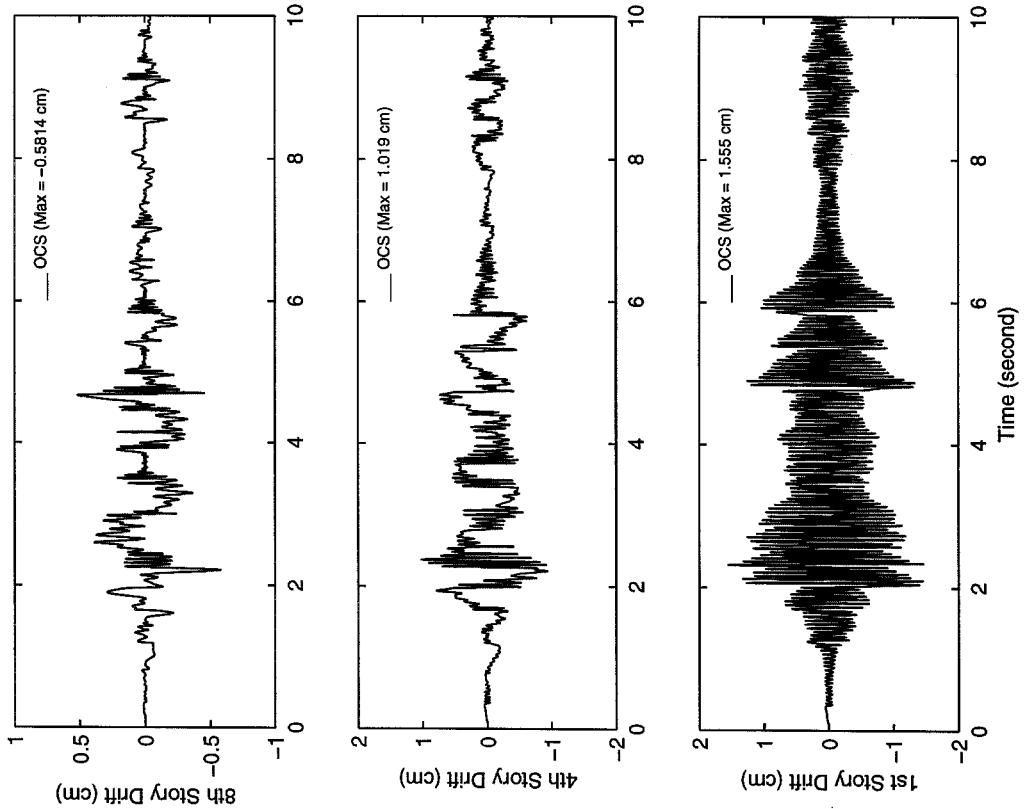

Figure 3.2.9: 1st, 4th, and 8th story drift responses of the AS excited by the ELC ground motion in the OCS algorithm in the NC approach

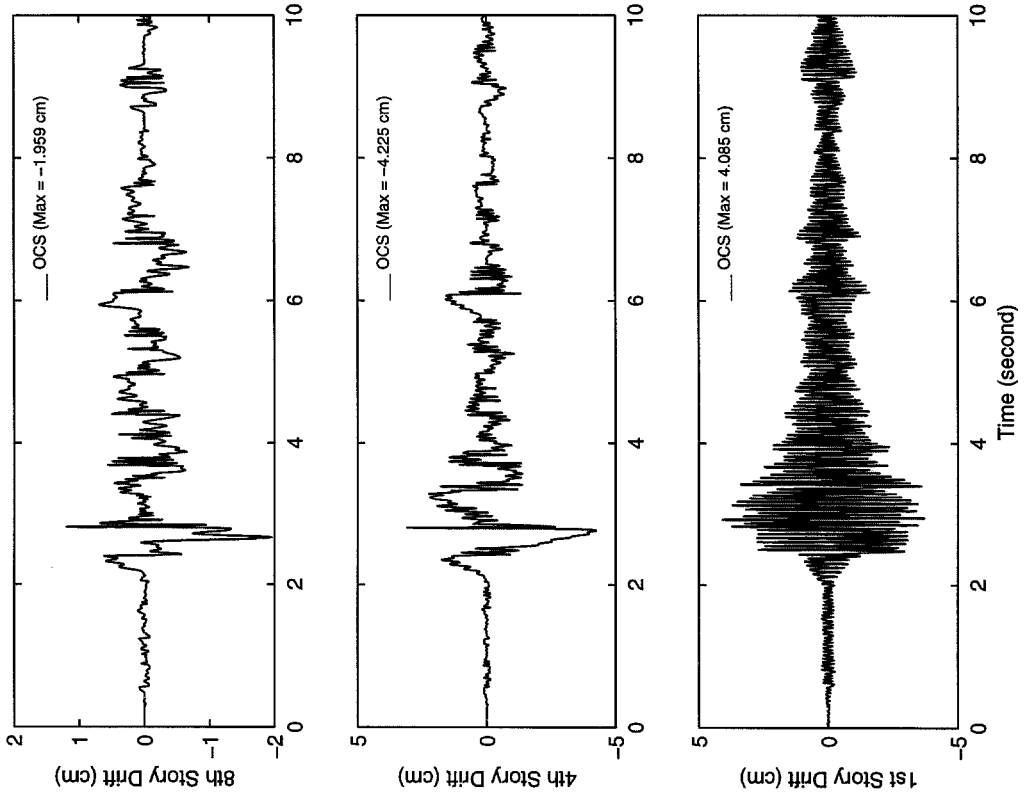

Figure 3.2.10: 1st, 4th, and 8th story drift responses of the AS excited by the RRS ground motion in the OCS algorithm in the NC approach

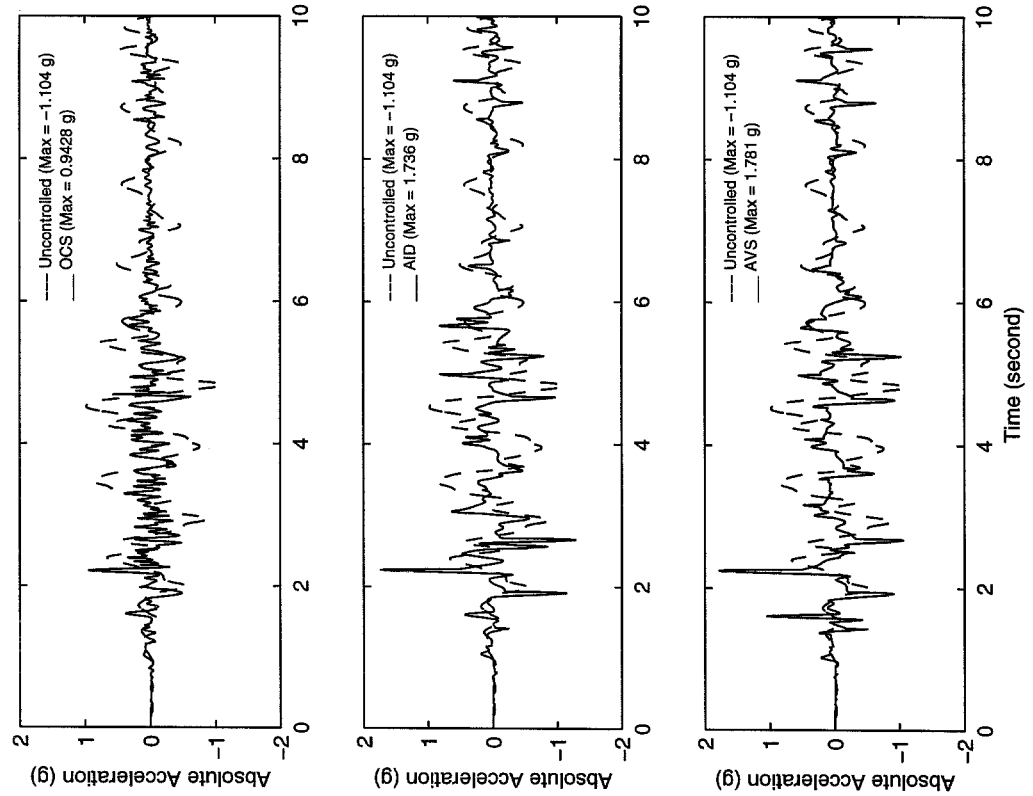

Figure 3.2.11: 8th story absolute acceleration responses of the PS excited by the ELC ground motion uncontrolled and controlled by the OCS, AID, and AVS algorithms in the NC approach

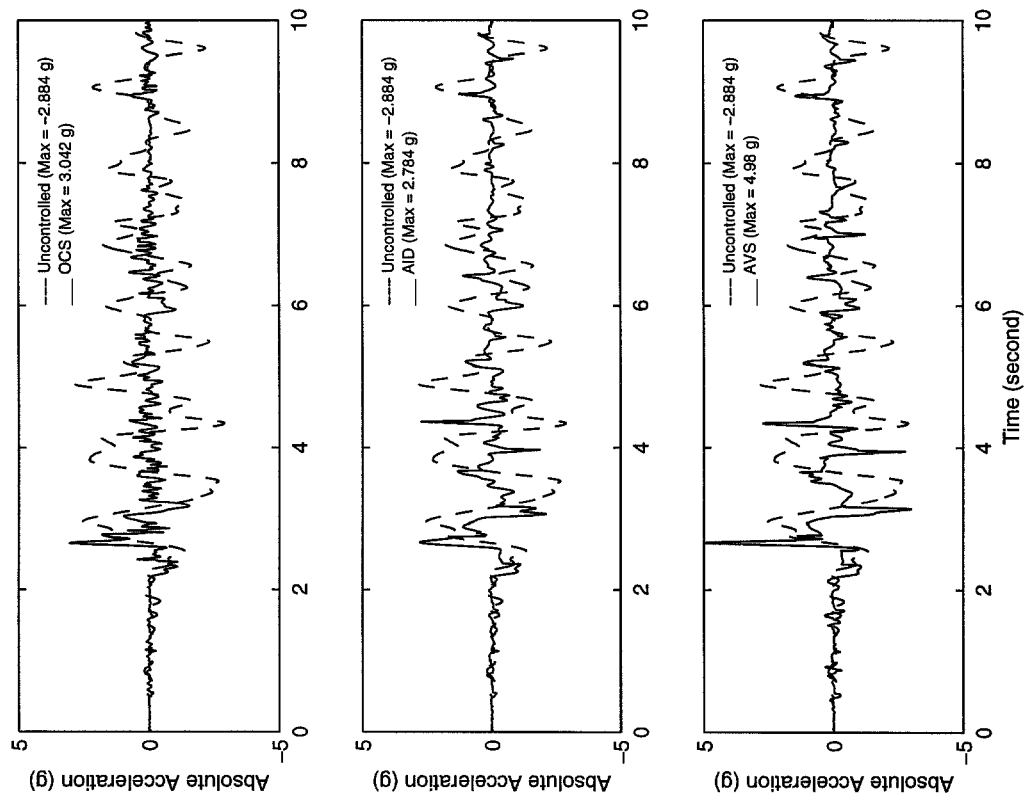

Figure 3.2.12: 8th story absolute acceleration responses of the PS excited by the RRS ground motion uncontrolled and controlled by the OCS, AID, and AVS algorithms in the NC approach

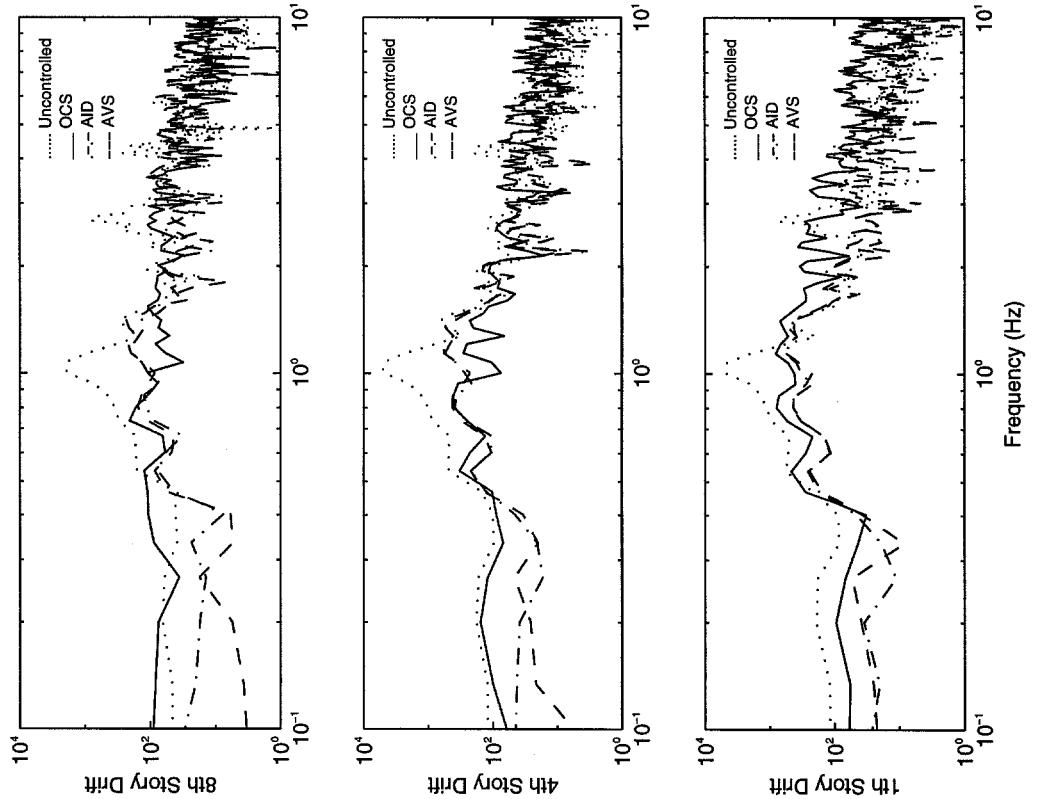

Figure 3.2.13: Fourier Amplitude Spectra of the 1st, 4th, and 8th story drift responses of the PS excited by the ELC ground motion uncontrolled and controlled by the OCS, AID, and AVS algorithms in the NC approach

Figure 3.2.14: Fourier Amplitude Spectra of the 1st, 4th, and 8th story drift responses of the PS excited by the RRS ground motion uncontrolled and controlled by the OCS, AID, and AVS algorithms in the NC approach

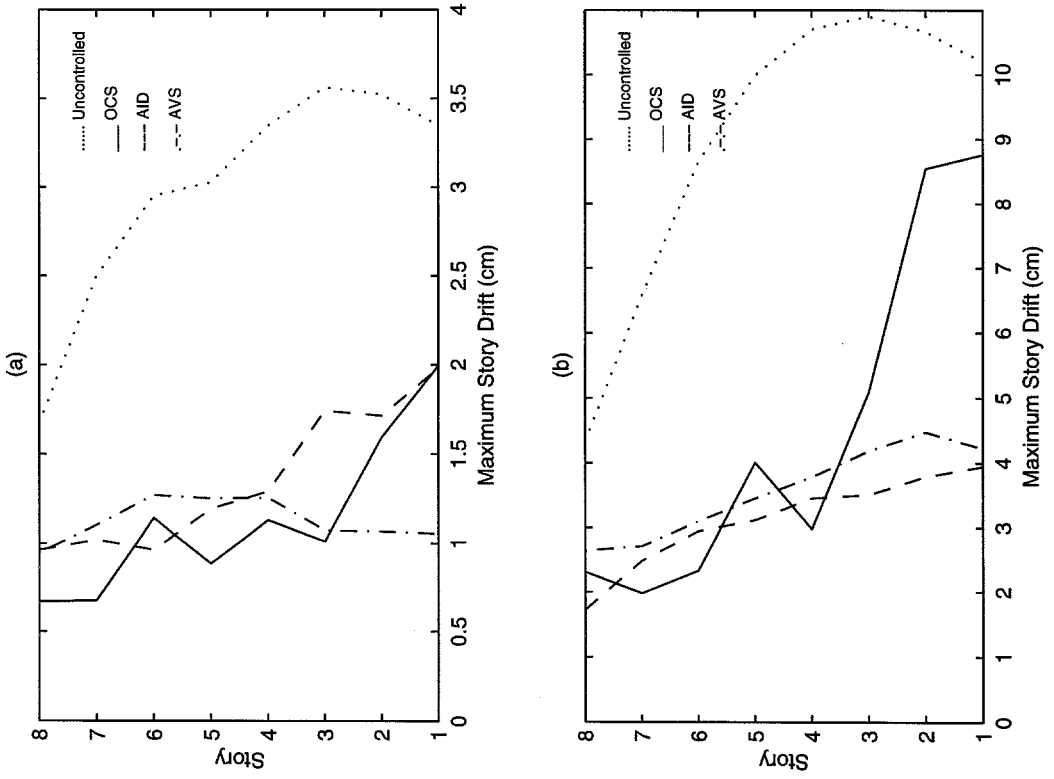

Figure 3.2.15: Maximum story drift distribution of the PS excited by the (a) ELC and (b) RRS ground motions uncontrolled and controlled by the OCS, AID, and AVS algorithms in the NC approach

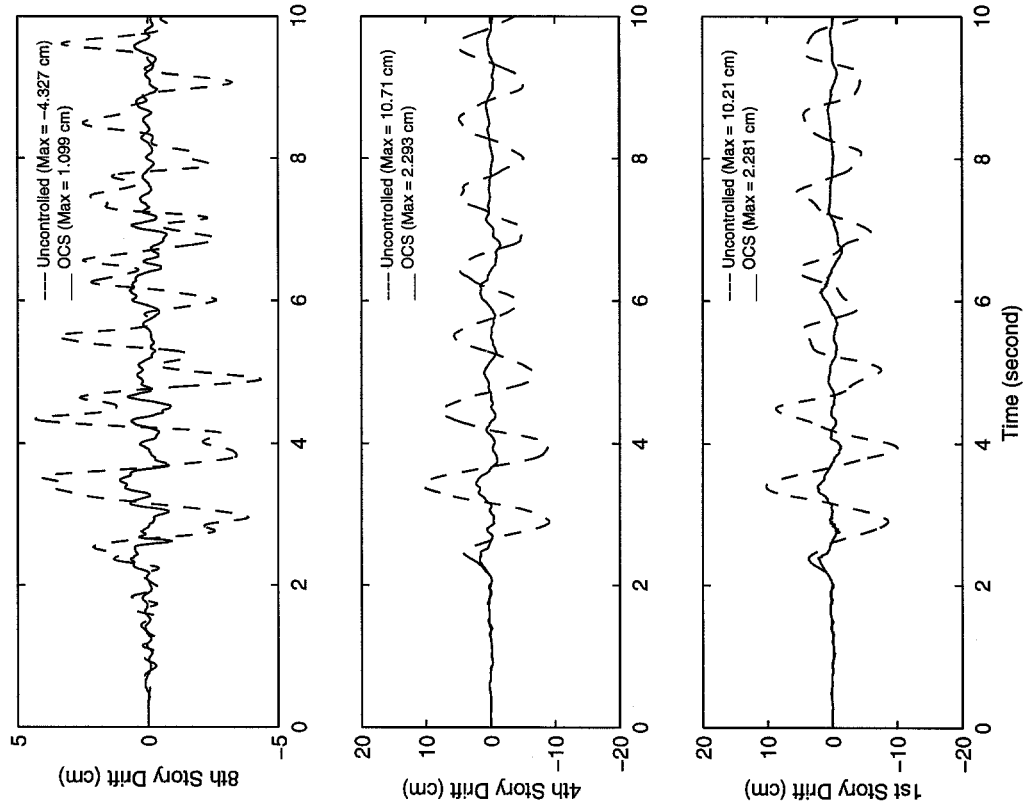

Figure 3.3.1: 1st, 4th, and 8th story drift responses of the PS excited by the ELC ground motion uncontrolled and controlled by the OCS algorithm in the MC approach

Figure 3.3.2: 1st, 4th, and 8th story drift responses of the PS excited by the RRS ground motion uncontrolled and controlled by the OCS algorithm in the MC approach

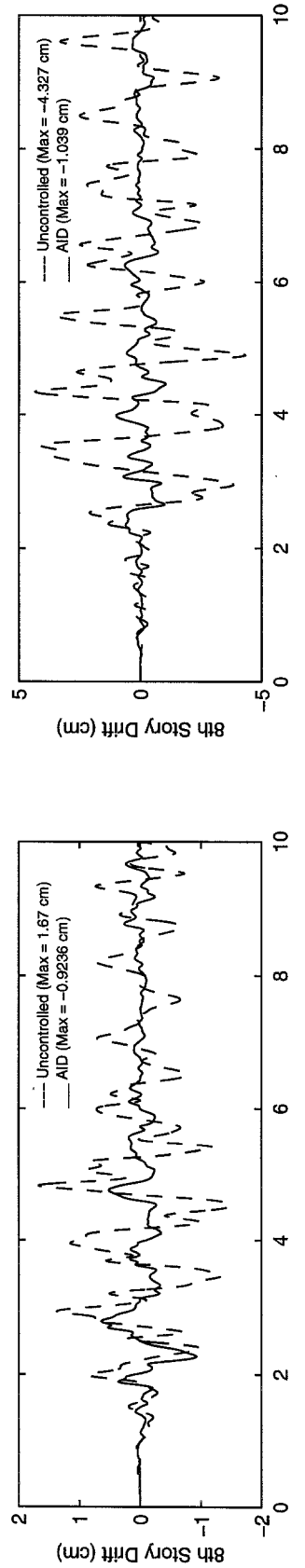

Figure 3.3.3: 1st, 4th, and 8th story drift responses of the PS excited by the ELC ground motion uncontrolled and controlled by the AID algorithm in the MC approach

Figure 3.3.4: 1st, 4th, and 8th story drift responses of the PS excited by the RRS ground motion uncontrolled and controlled by the AID algorithm in the MC approach

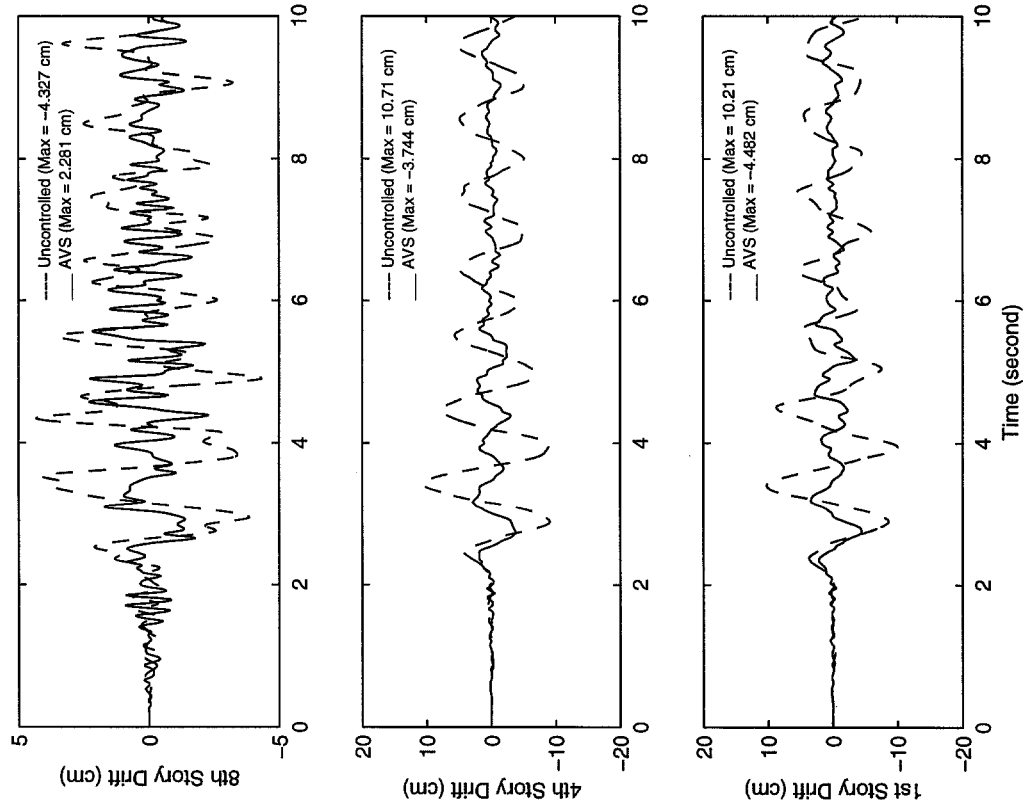

Figure 3.3.5: 1st, 4th, and 8th story drift responses of the PS excited by the ELC ground motion uncontrolled and controlled by the AVS algorithm in the MC approach

Figure 3.3.6: 1st, 4th, and 8th story drift responses of the PS excited by the RRS ground motion uncontrolled and controlled by the AVS algorithm in the MC approach

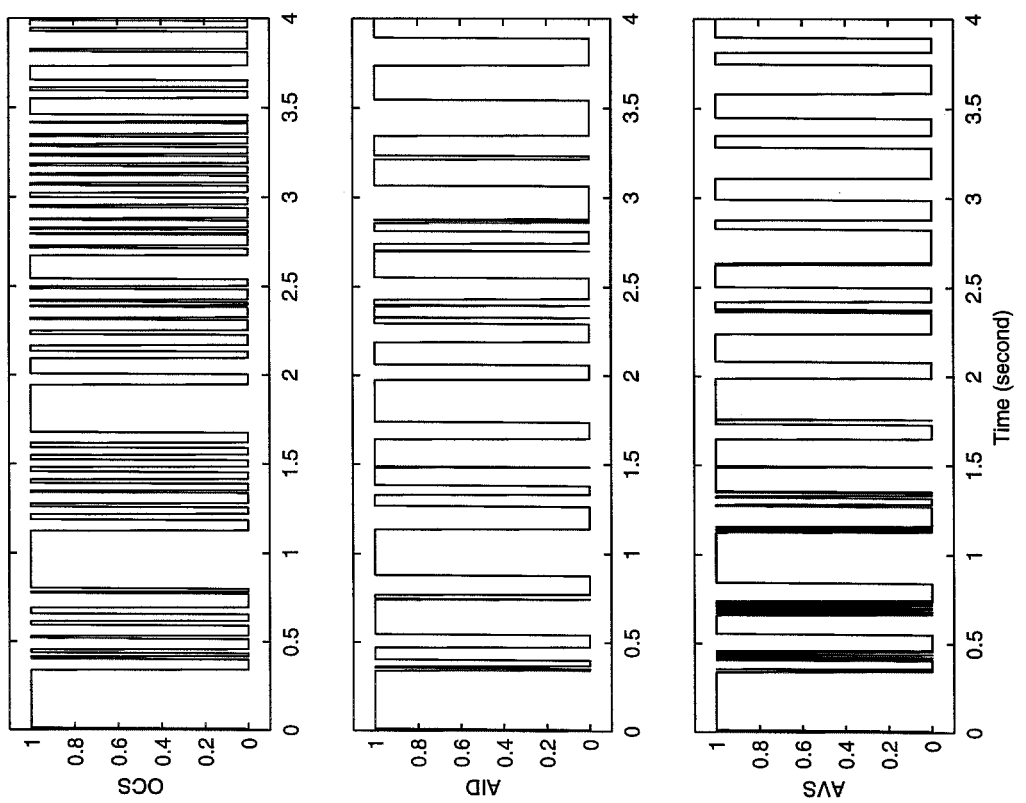

Figure 3.3.7: 1st story attachment time histories of the PS excited by the ELC ground motion controlled by the OCS, AID, and AVS algorithms in the MC approach

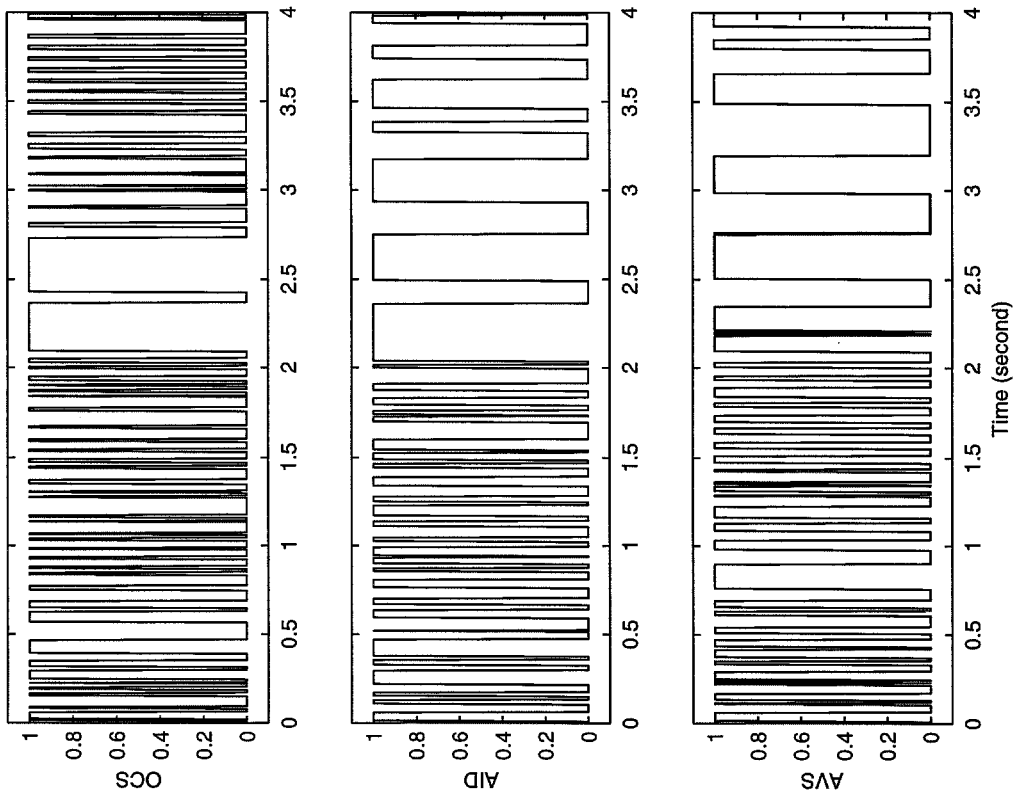

Figure 3.3.8: 1st story attachment time histories of the PS excited by the RRS ground motion controlled by the OCS, AID, and AVS algorithms in the MC approach

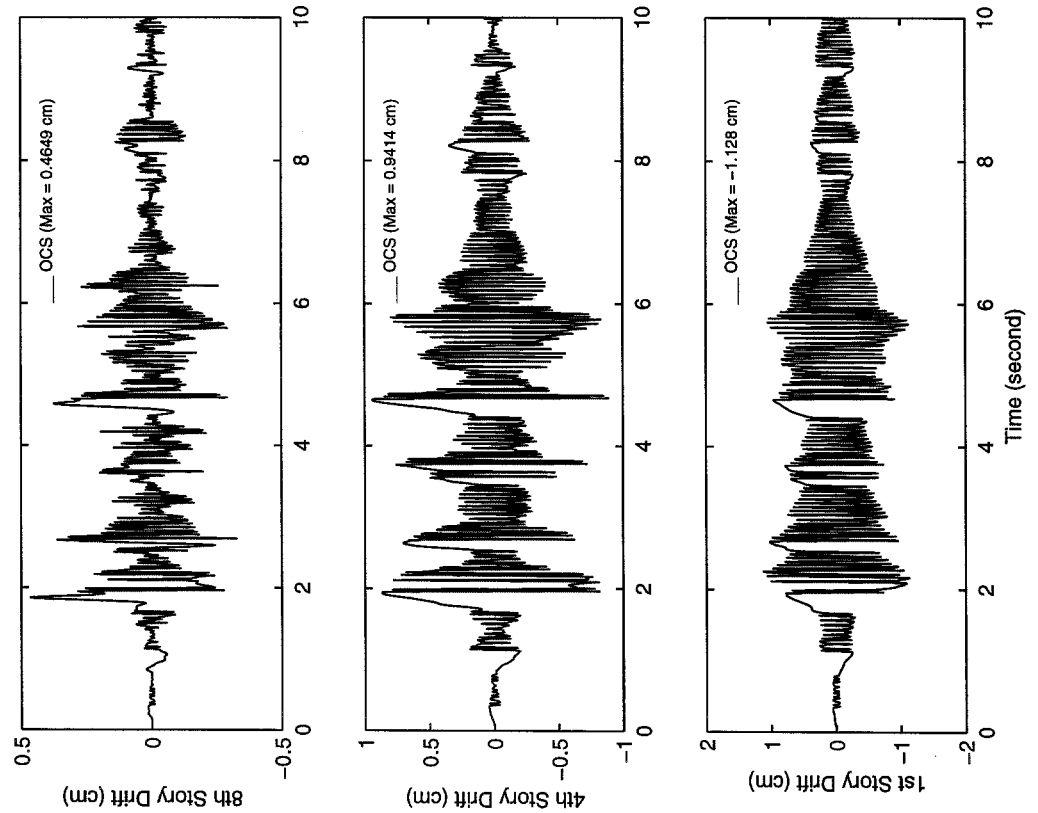

Figure 3.3.9: 1st, 4th, and 8th story drift responses of the AS excited by the ELC ground motion in the OCS algorithm in the MC approach

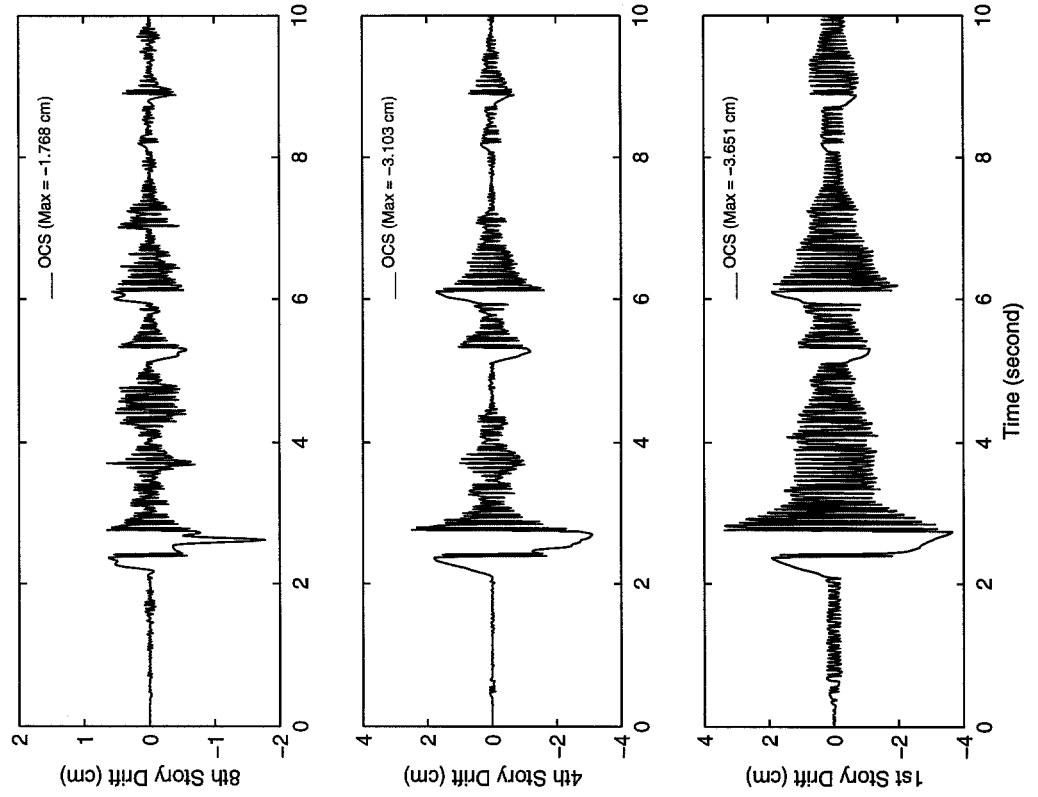

Figure 3.3.10: 1st, 4th, and 8th story drift responses of the AS excited by the RRS ground motion in the OCS algorithm in the MC approach

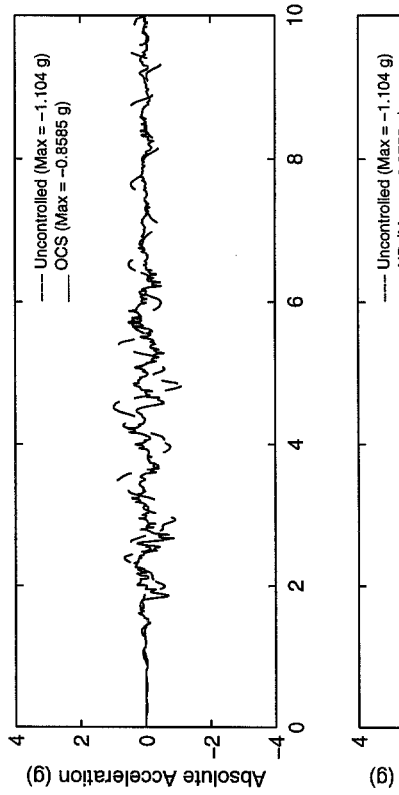

Figure 3.3.11: 8th story absolute acceleration responses of the PS excited by the ELC ground motion uncontrolled and controlled by the OCS, AID, and AVS algorithms in the MC approach

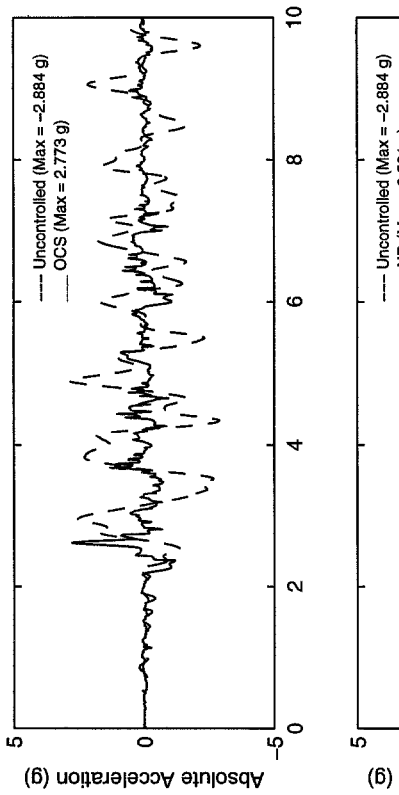

Figure 3.3.12: 8th story absolute acceleration responses of the PS excited by the RRS ground motion uncontrolled and controlled by the OCS, AID, and AVS algorithms in the MC approach

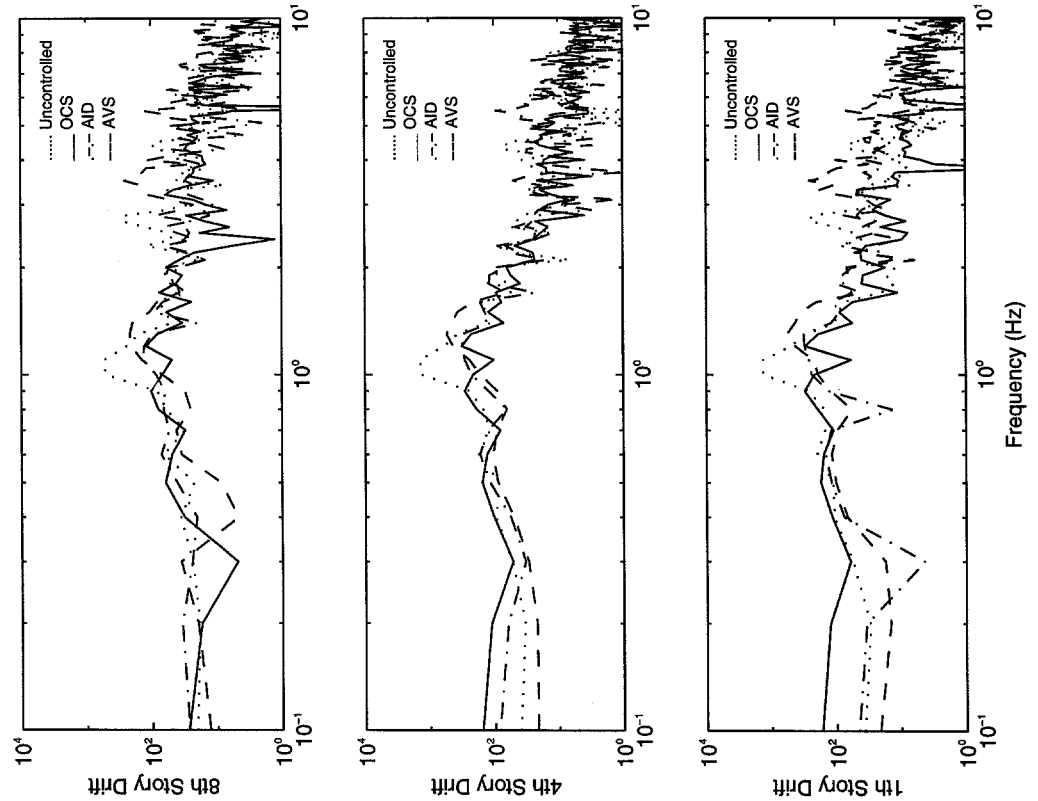

Figure 3.3.13: Fourier Amplitude Spectra of the 1st, 4th, and 8th story drift responses of the PS excited by the ELC ground motion uncontrolled and controlled by the OCS, AID, and AVS algorithms in the MC approach

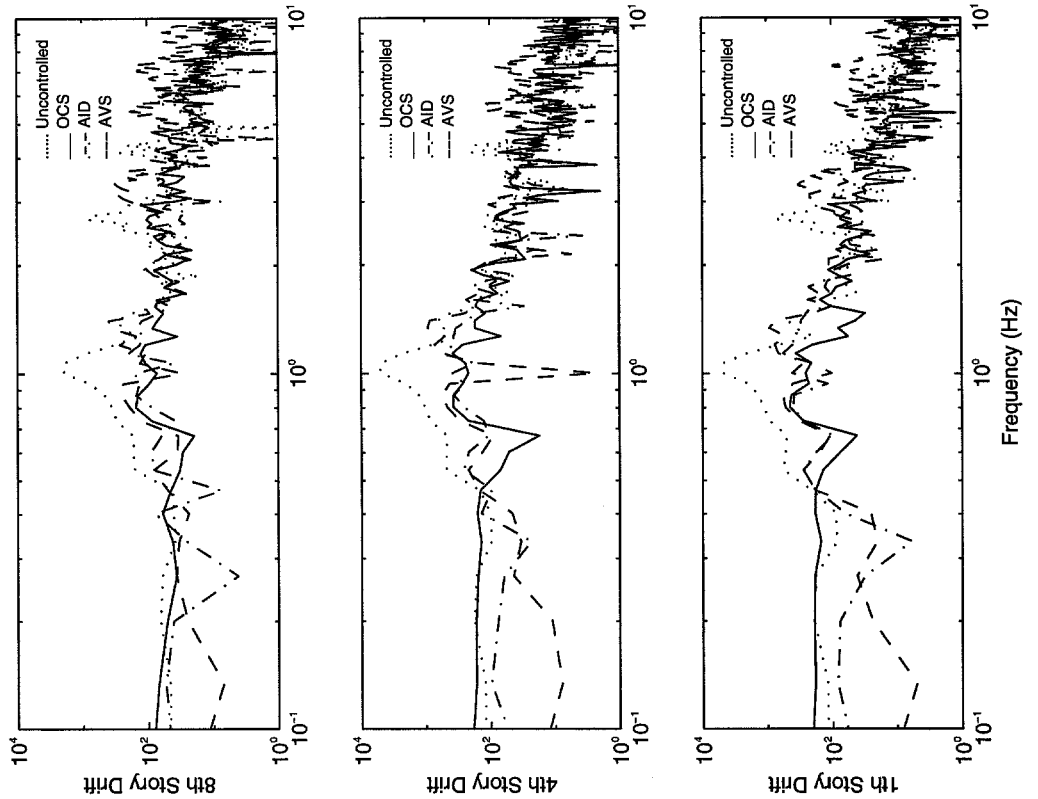

Figure 3.3.14: Fourier Amplitude Spectra of the 1st, 4th, and 8th story drift responses of the PS excited by the RRS ground motion uncontrolled and controlled by the OCS, AID, and AVS algorithms in the MC approach

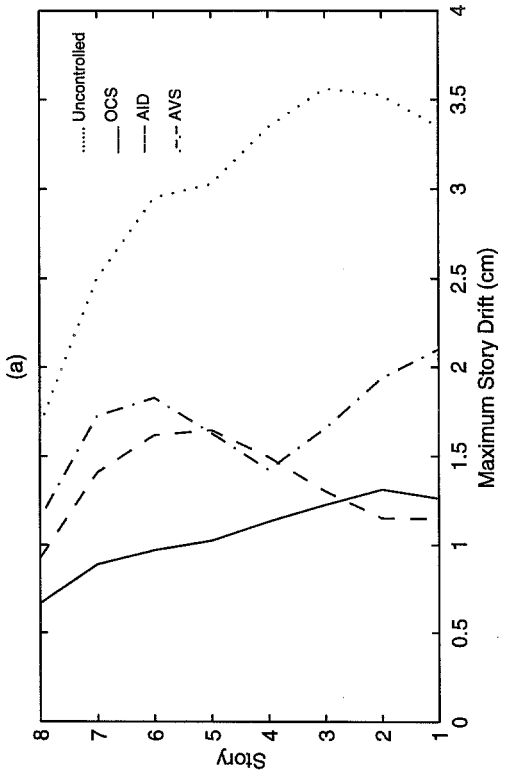

Figure 3.3.15: Maximum story drift distribution of the PS excited by the (a) ELC and (b) RRS ground motions uncontrolled and controlled by the OCS, AID, and AVS algorithms in the MC approach (control decision made in the 1st story)

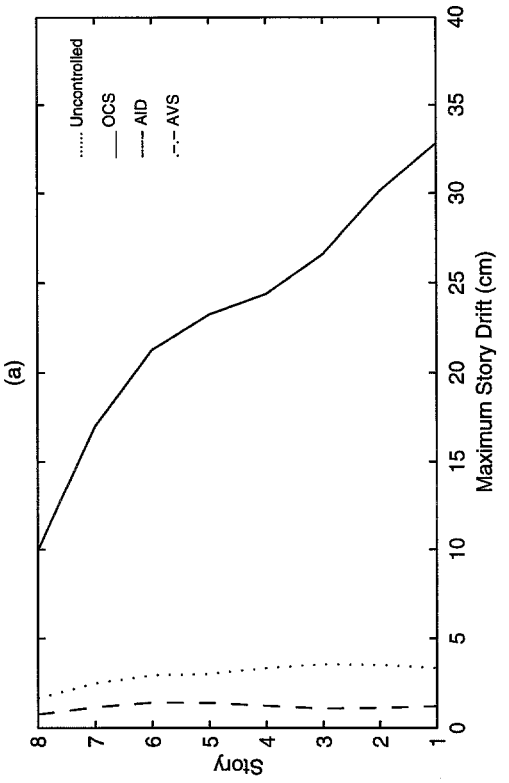

Figure 3.3.16: Maximum story drift distribution of the PS excited by the (a) ELC and (b) RRS ground motions uncontrolled and controlled by the OCS, AID, and AVS algorithms in the MC approach (control decision made in the 3rd story)

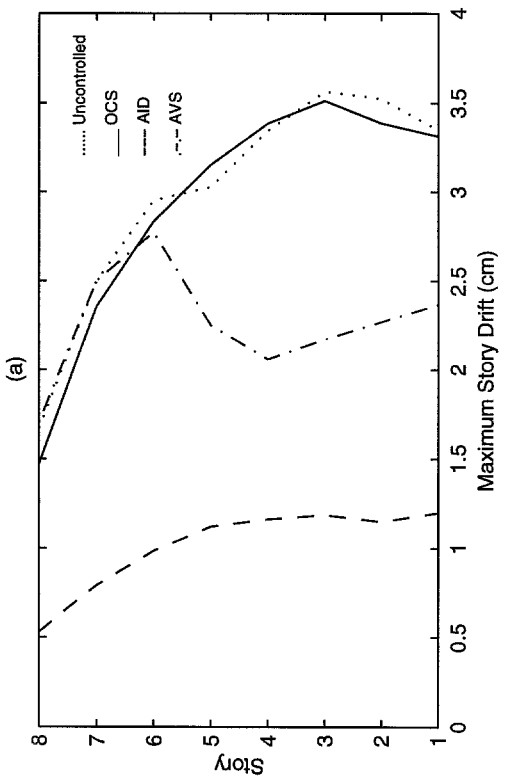

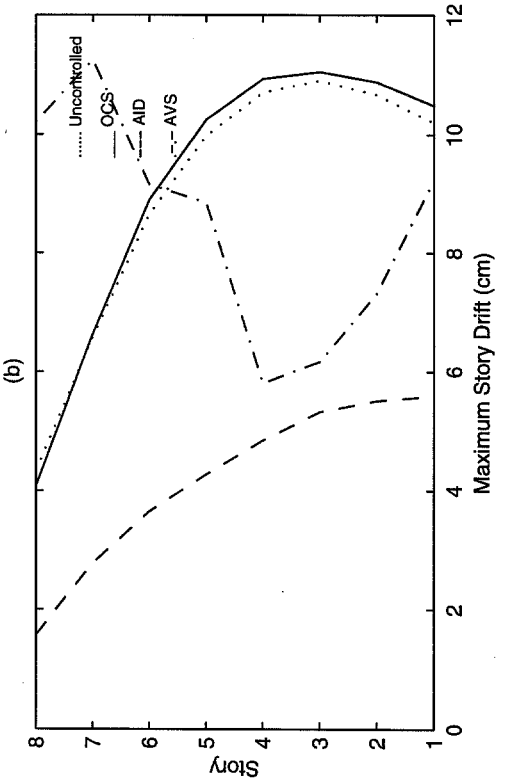

Figure 3.3.18: Maximum story drift distribution of the PS excited by the (a) ELC and (b) RRS ground motions uncontrolled and controlled by the OCS, AID, and AVS algorithms in the MC approach (control decision made in the 8th story)

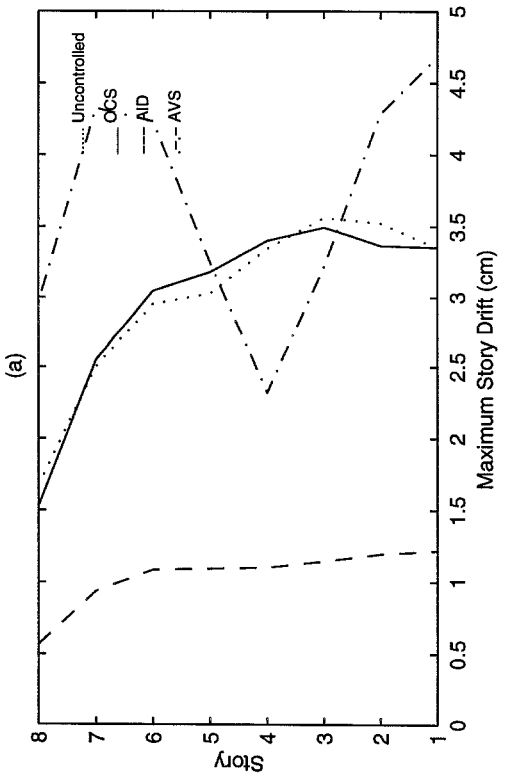

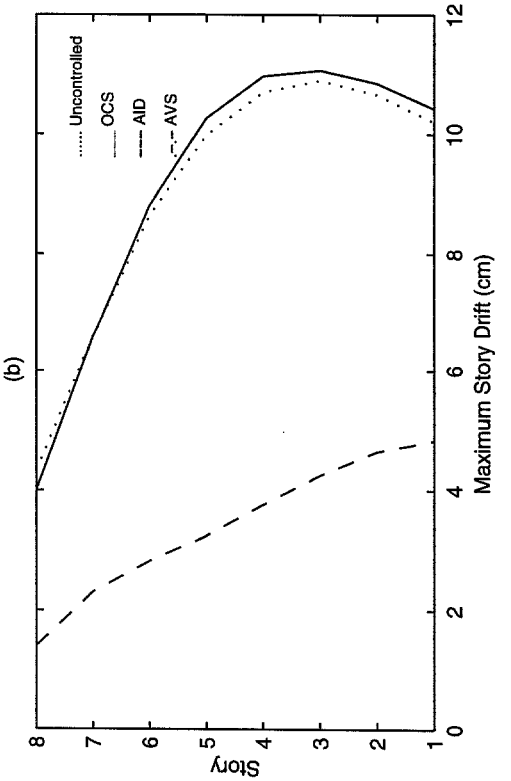

Figure 3.3.17: Maximum story drift distribution of the PS excited by the (a) ELC and (b) RRS ground motions uncontrolled and controlled by the OCS, AID, and AVS algorithms in the MC approach (control decision made in the 5th story)

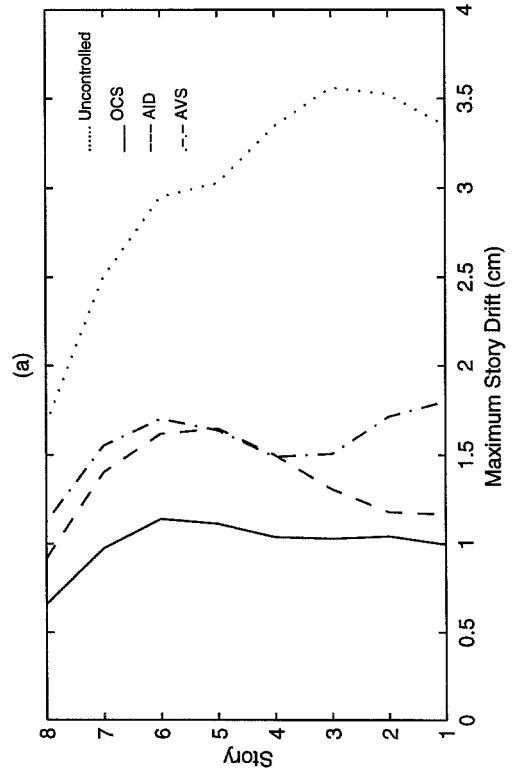

Figure 3.3.19: Maximum story drift distribution of the PS excited by the (a) ELC and (b) RRS ground motions uncontrolled and controlled by the OCS, AID, and AVS algorithms in the MC approach (uncertainties in the mass of the AS)

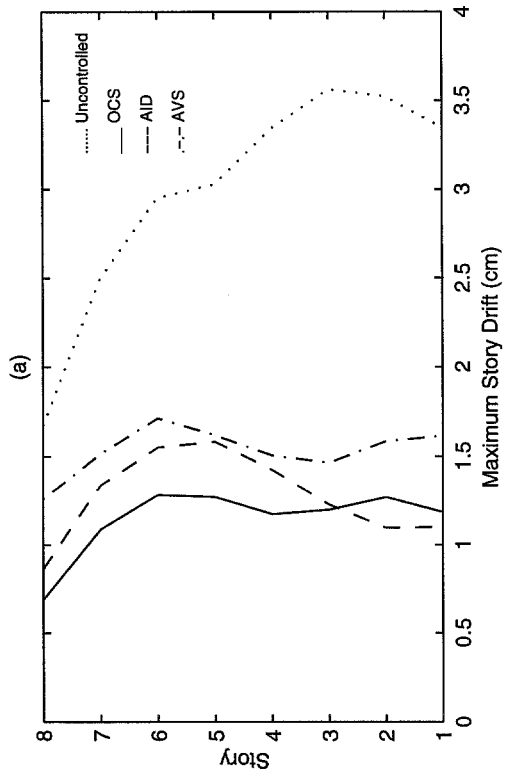

Figure 3.3.20: Maximum story drift distribution of the PS excited by the (a) ELC and (b) RRS ground motions uncontrolled and controlled by the OCS, AID, and AVS algorithms in the MC approach (uncertainties in the stiffness of the AS)

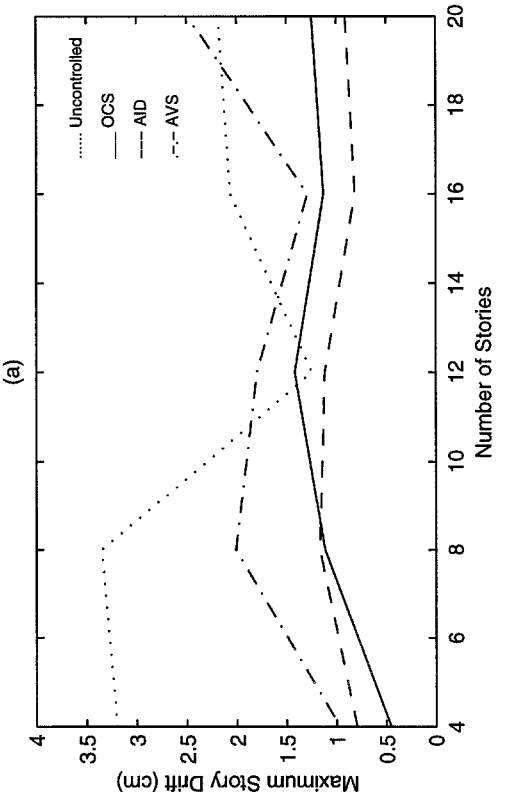

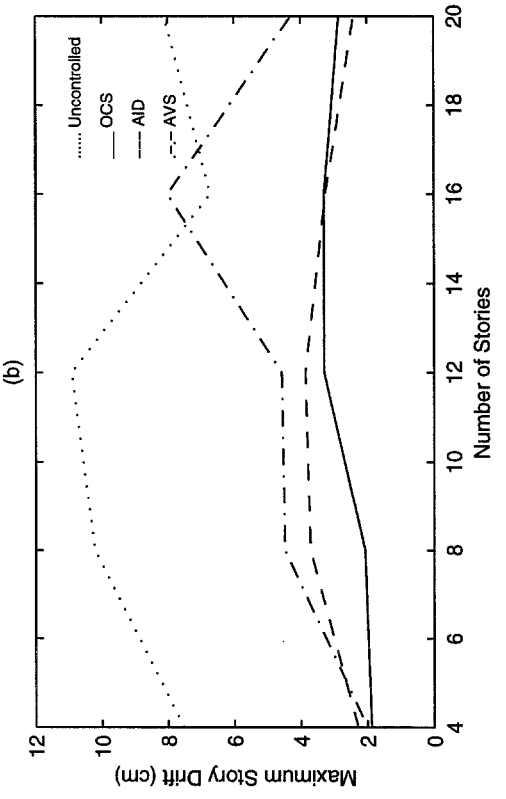

Figure 3.4.2: SDS of the PS excited by the (a) ELC and (b) RRS ground motions uncontrolled and controlled by the OCS, AID, and AVS algorithms in the MC approach

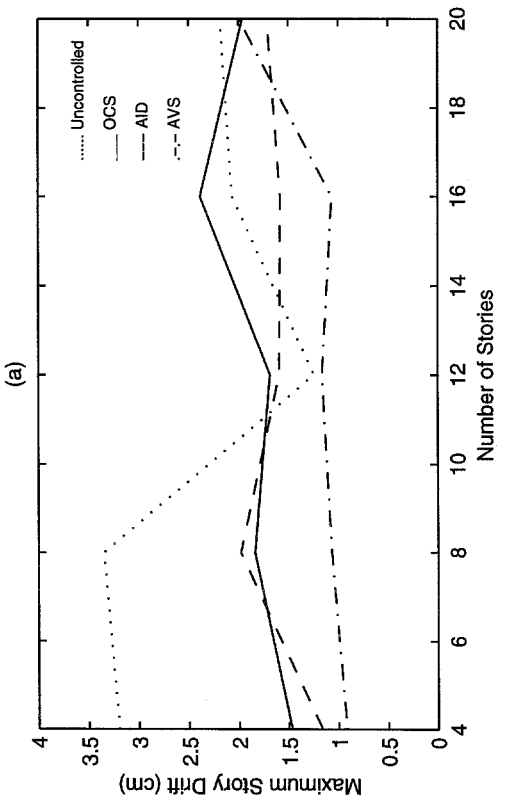

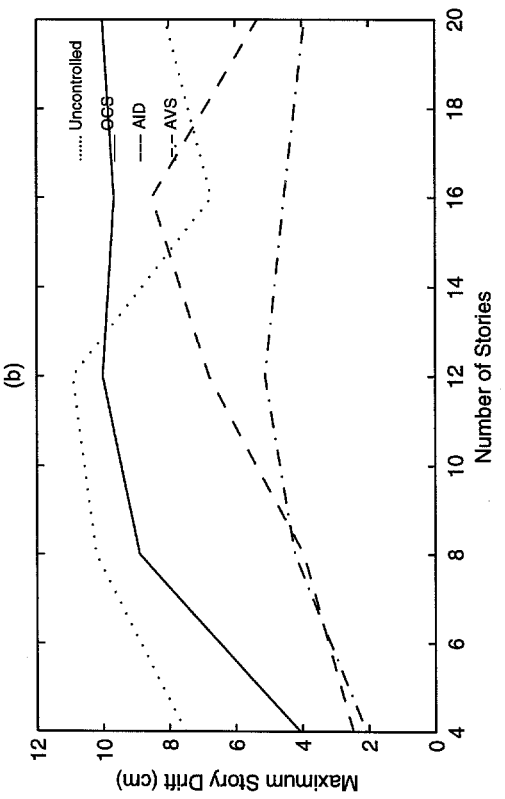

Figure 3.4.1: SDS of the PS excited by the (a) ELC and (b) RRS ground motions uncontrolled and controlled by the OCS, AID, and AVS algorithms in the NC approach

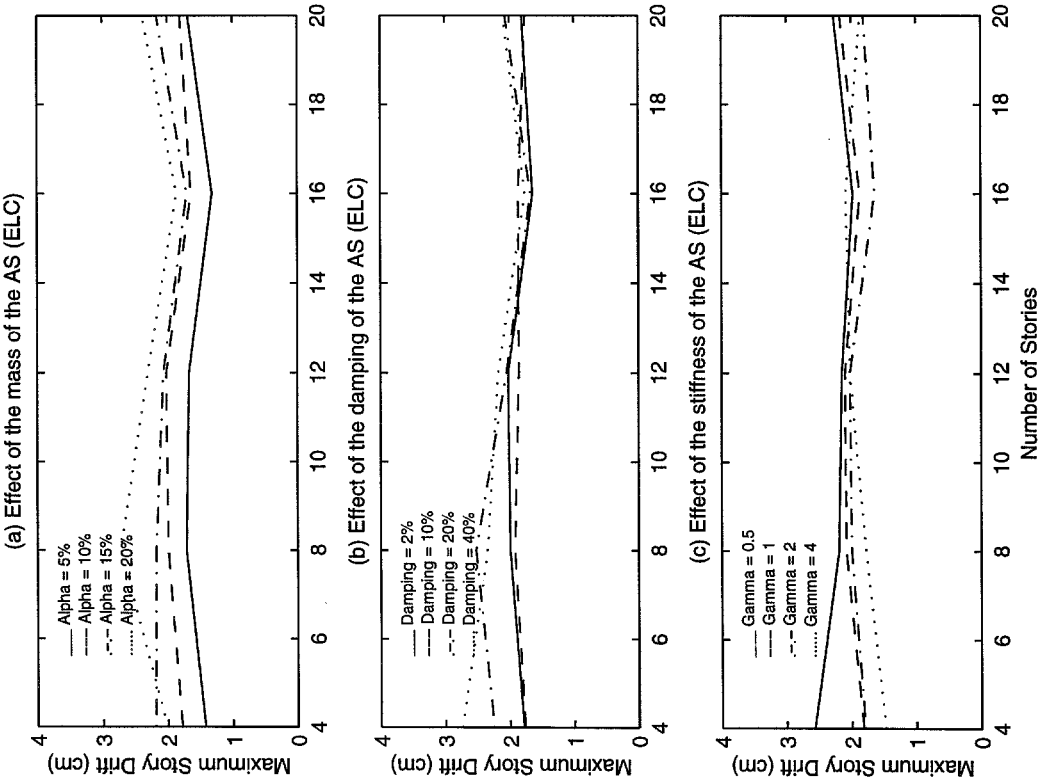

Figure 3.4.3: SDS of the PS excited by the ELC ground motion controlled by the OCS algorithm in the NC approach (effects of the mass, damping, and stiffness of the AS)

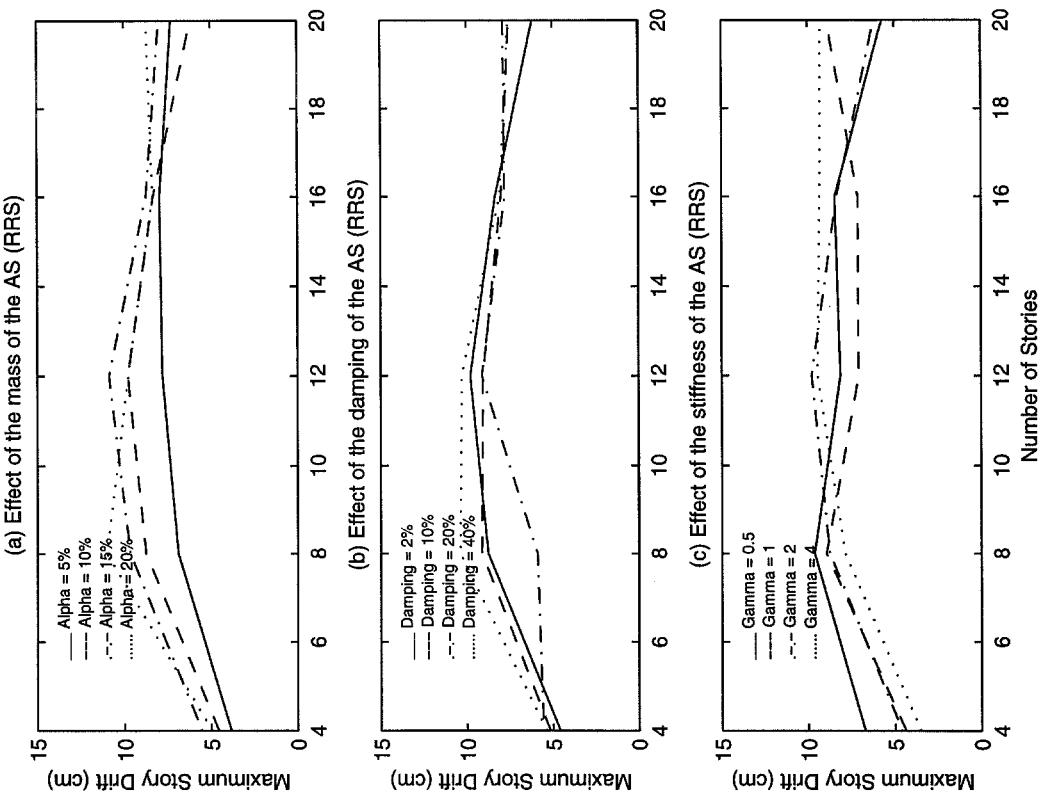

Figure 3.4.4: SDS of the PS excited by the RRS ground motion controlled by the OCS algorithm in the NC approach (effects of the mass, damping, and stiffness of the AS)

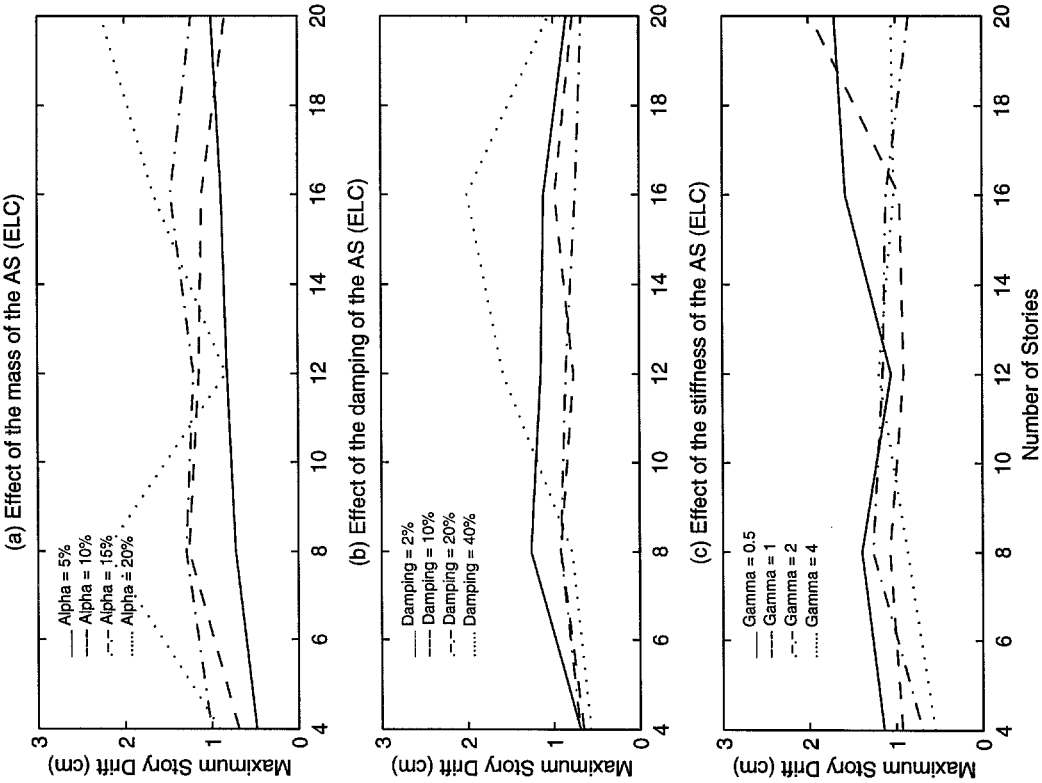

Figure 3.4.5: SDS of the PS excited by the ELC ground motion controlled by the OCS algorithm in the MC approach (effects of the mass, damping, and stiffness of the AS)

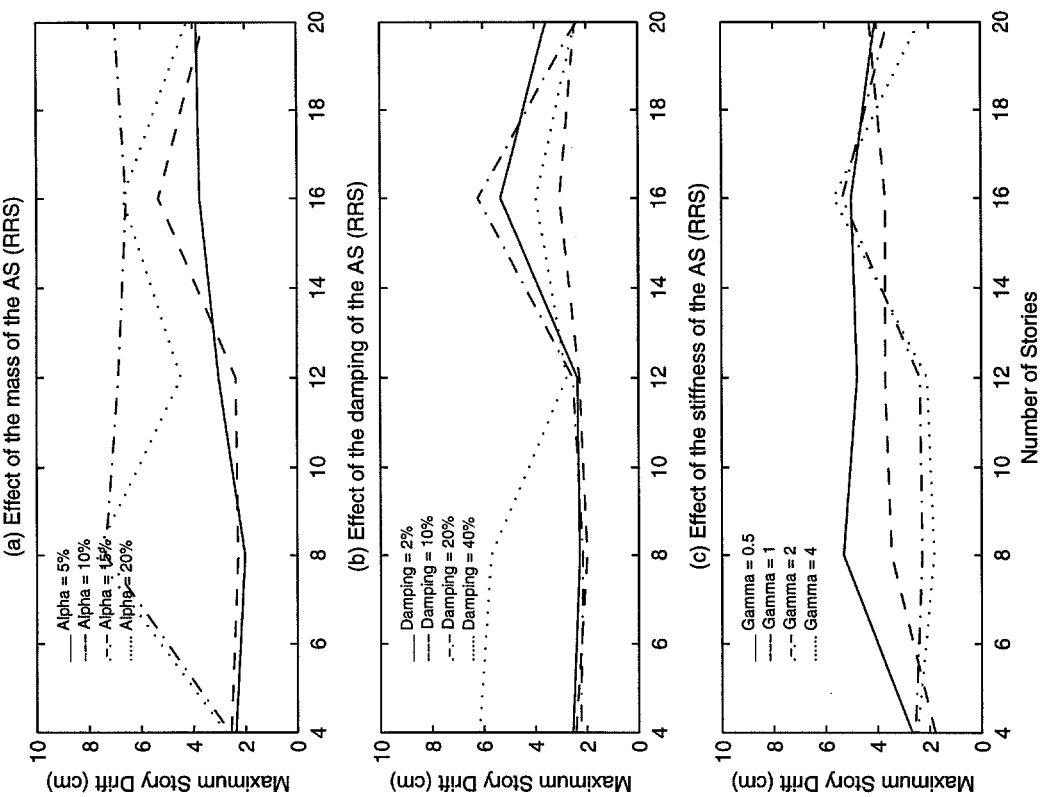

Figure 3.4.6: SDS of the PS excited by the RRS ground motion controlled by the OCS algorithm in the MC approach (effects of the mass, damping, and stiffness of the AS)

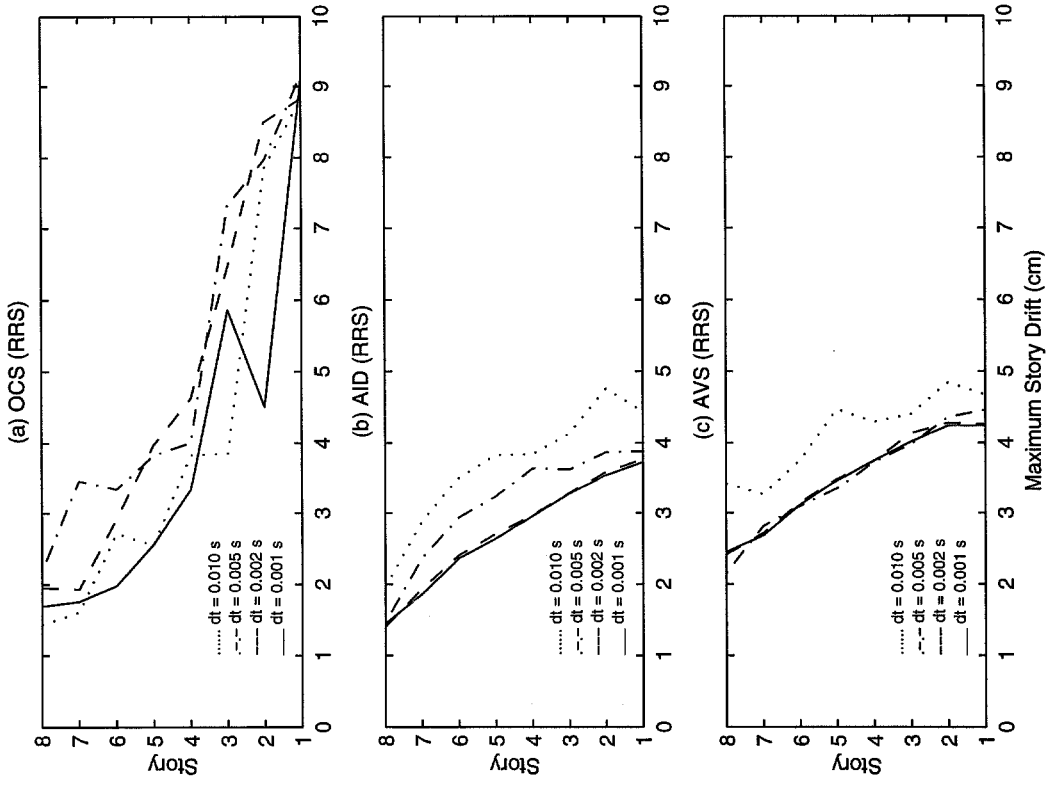

Figure 3.5.2: Maximum story drift distribution of the PS excited by the RRS ground motion controlled by the OCS algorithm in the NC approach (effect of the sampling interval)

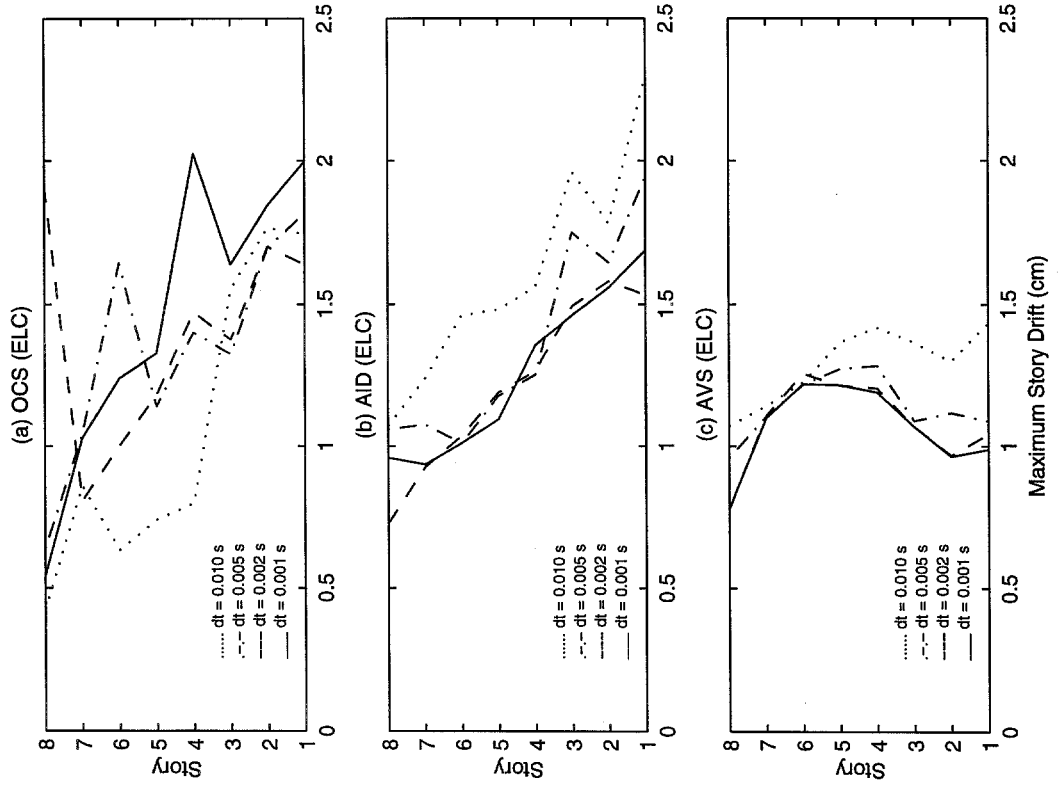

Figure 3.5.1: Maximum story drift distribution of the PS excited by the ELC ground motion controlled by the OCS algorithm in the NC approach (effect of the sampling interval)

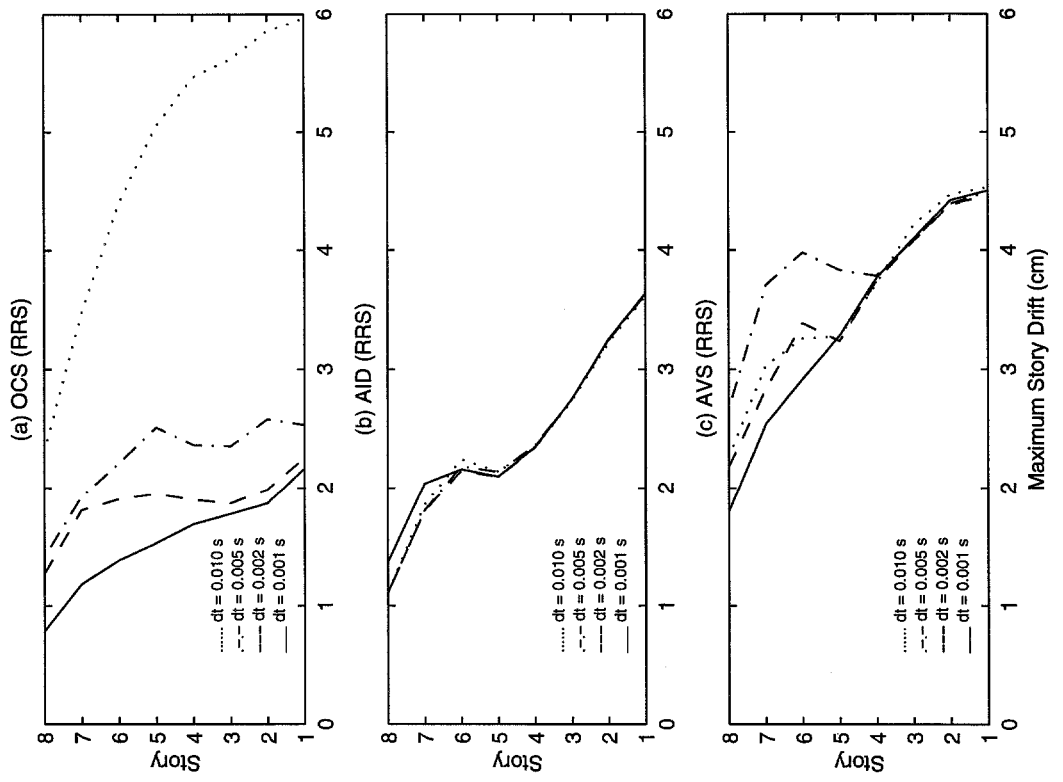

Figure 3.5.4: Maximum story drift distribution of the PS excited by the RRS ground motion controlled by the OCS algorithm in the MC approach (effect of the sampling interval)

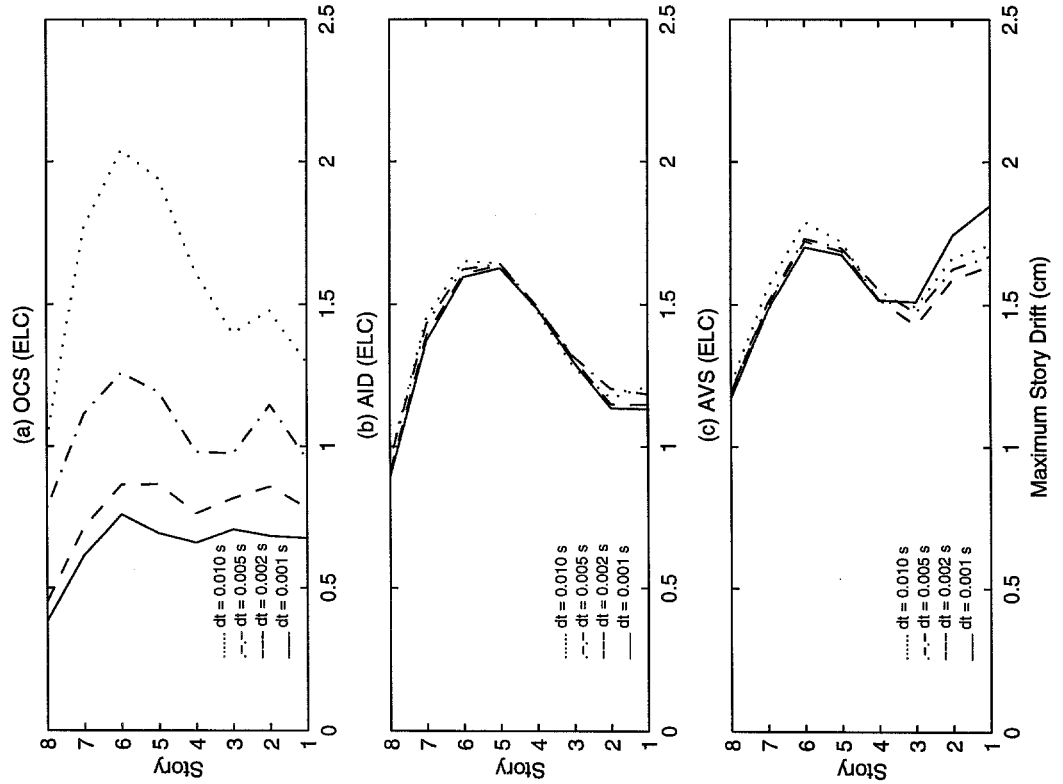

Figure 3.5.3: Maximum story drift distribution of the PS excited by the ELC ground motion controlled by the OCS algorithm in the MC approach (effect of the sampling interval)

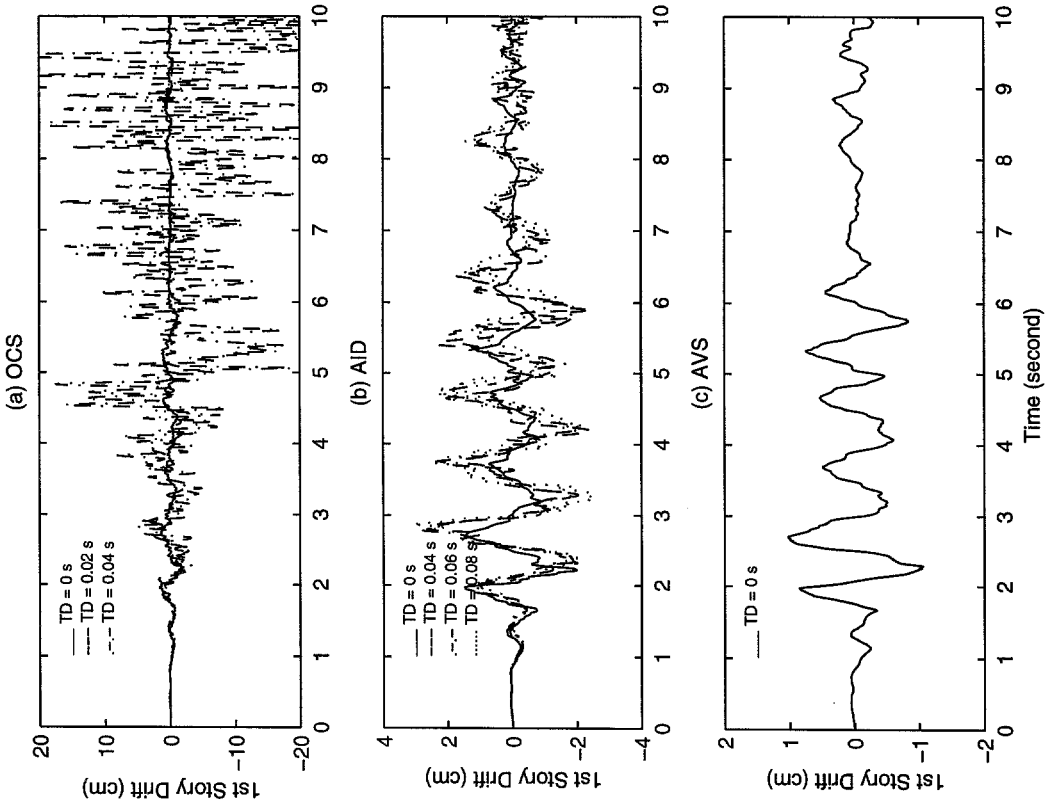

Figure 3.5.5: 1st story drift responses of the PS excited by the ELC ground motion controlled by the OCS, AID, and AVS algorithms in the NC approach (effect of the time delay)

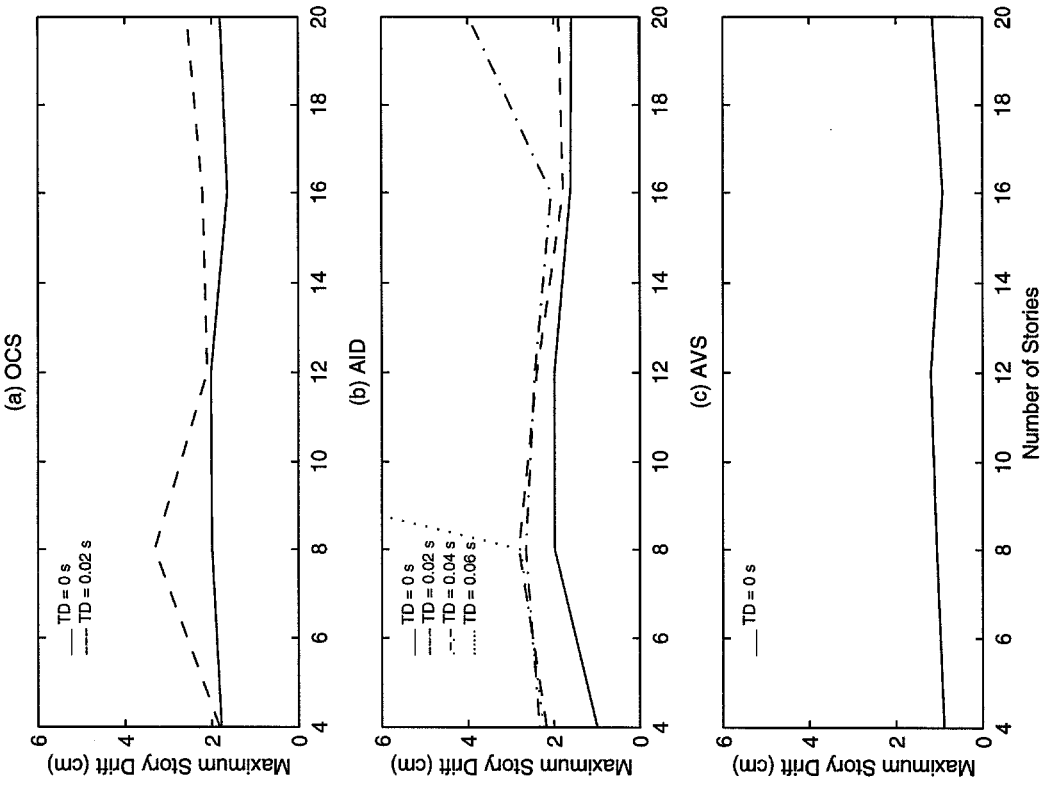

Figure 3.5.6: SDS of the PS excited by the RRS ground motion controlled by the OCS, AID, and AVS algorithms in the NC approach (effect of the time delay)

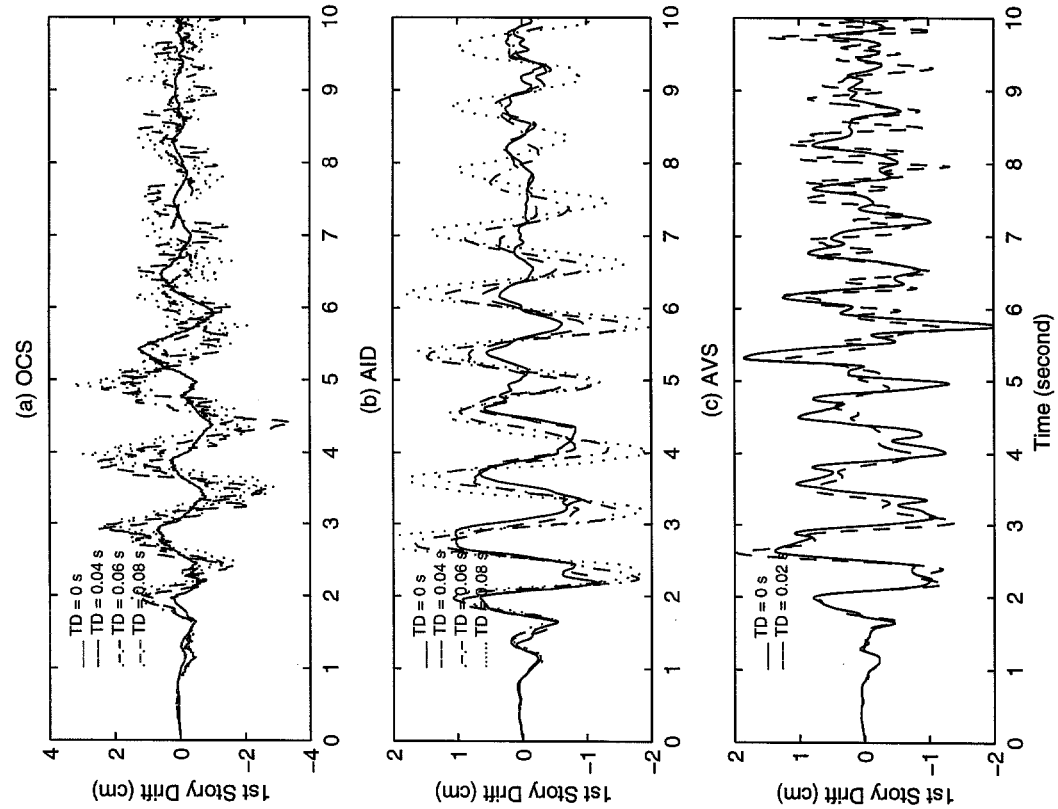

Figure 3.5.7: 1st story drift responses of the PS excited by the ELC ground motion controlled by the OCS, AID, and AVS algorithms in the MC approach (effect of the time delay)

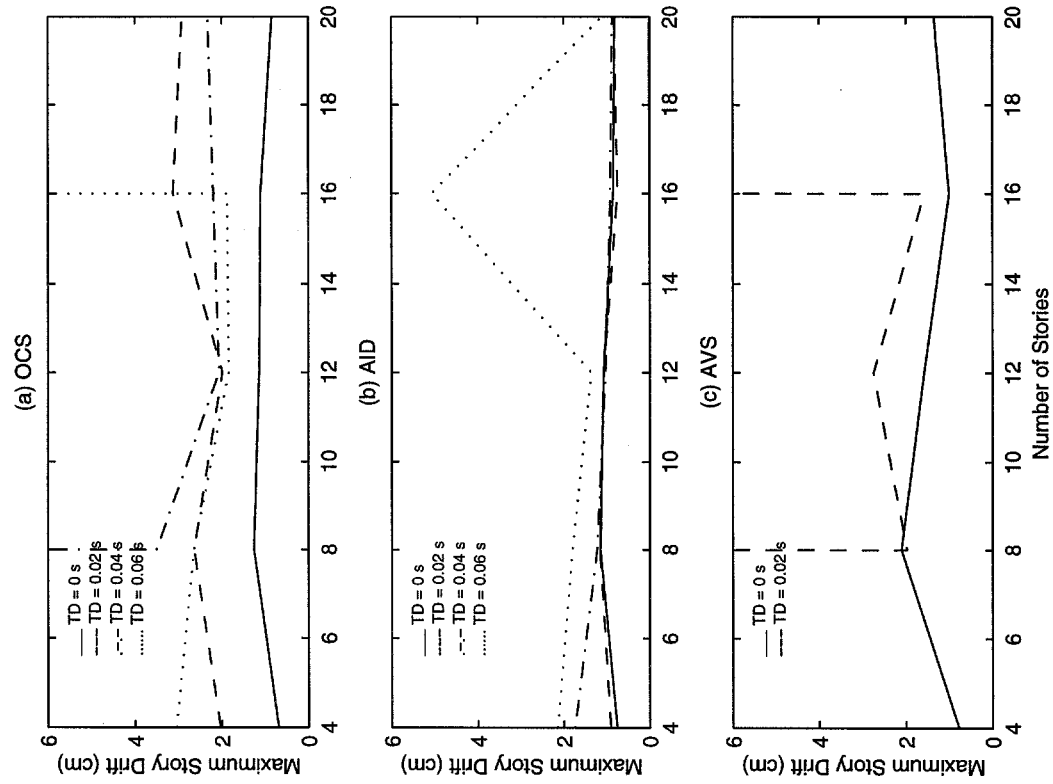

Figure 3.5.8: SDS of the PS excited by the RRS ground motion controlled by the OCS, AID, and AVS algorithms in the MC approach (effect of the time delay)

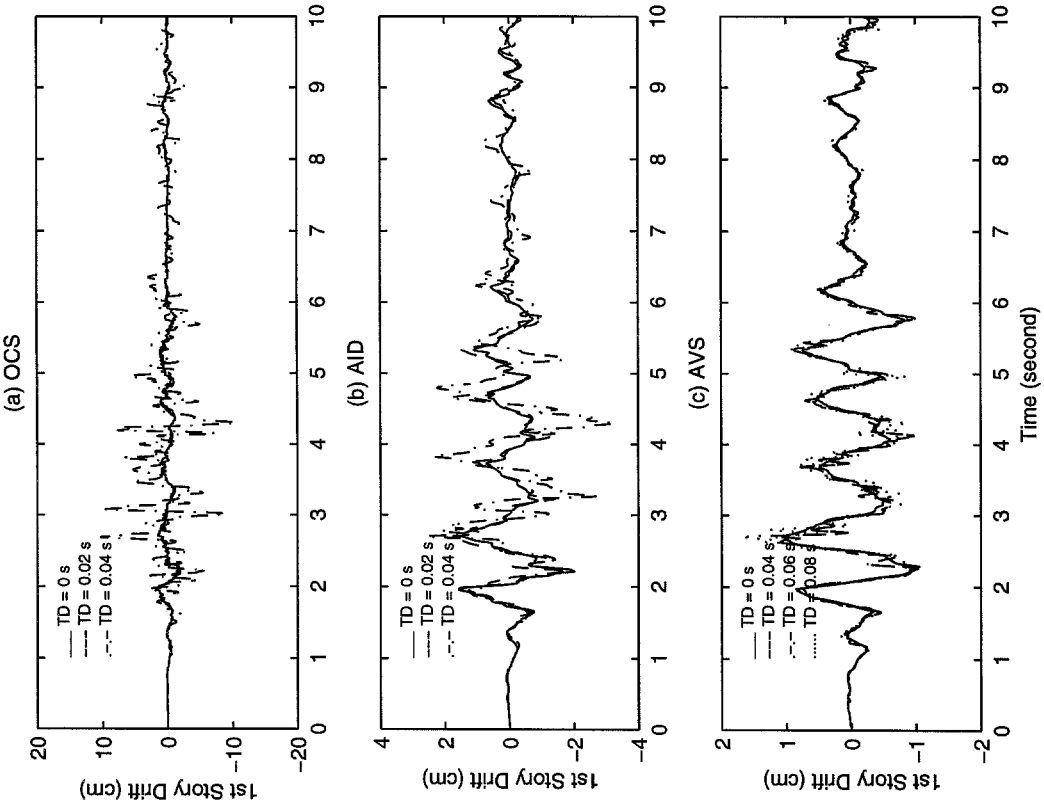

Figure 3.5.9: 1st story drift responses of the PS excited by the ELC ground motion controlled by the OCS, AID, and AVS algorithms in the NC approach with time delay compensation

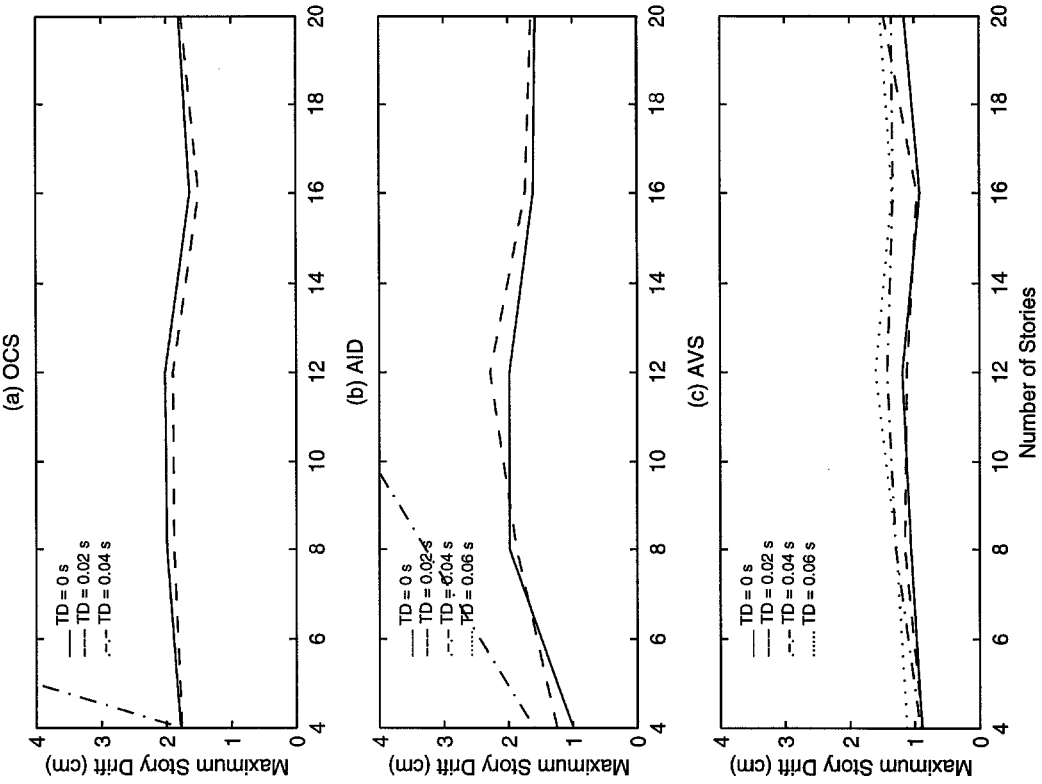

Figure 3.5.10: SDS of the PS excited by the RRS ground motion controlled by the OCS, AID, and AVS algorithms in the NC approach with time delay compensation

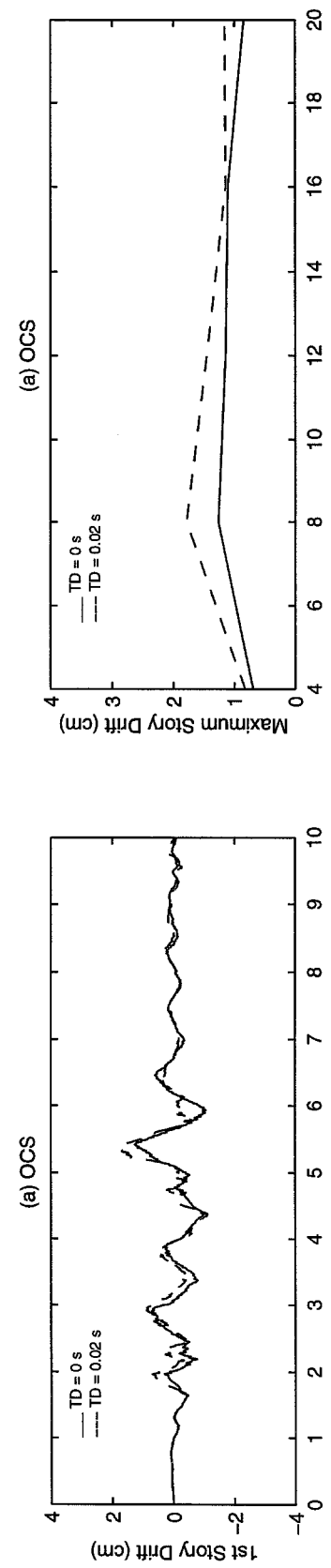

Figure 3.5.11: 1st story drift responses of the PS excited by the ELC ground motion controlled by the OCS, AID, and AVS algorithms in the NC approach with time delay compensation

Figure 3.5.12: SDS of the PS excited by the RRS ground motion controlled by the OCS, AID, and AVS algorithms in the MC approach with time delay compensation

Chapter 4

Summary and Conclusions

4.1 Summary

AIC utilizes dynamic interactions between different structures, or components of the same structure, to reduce the response of the PS under earthquake or wind excitation. The interactions are achieved by means of actively controlled linking devices such as hydraulic valves or friction plates, which can be operated in either a complete free, rigid, or viscous state.

The primary control objective of AIC is to minimize the maximum story drift of the PS. This is accomplished by appropriately timing the controlled interactions between the PS and AS according to an AIC algorithm so as to withdraw the maximum possible vibrational energy from the PS. The energy is transferred to the AS, where it is stored and eventually dissipated as the external excitation decreases. The AS and IE may therefore be regarded as playing the role of an actuator for the PS. One important advantage of this type of control over most prevailing active control approaches is the very low external power required.

This study examines the effectiveness of several existing control algorithms for use in AIC, and presents a new control algorithm, termed the OCS algorithms, that shows promise for application to buildings and other structures subjected to severe dynamic

loads. The motivation behind the OCS algorithm is to maximize the effective hysteretic energy dissipation in the PS by timed interactions with the AS.

In Chapter 2, the seismic response and characteristics of an AIC system are investigated wherein the PS and AS are each modeled by a SDOF system. The control efficiencies of the OCS, AID, and AVS algorithms are demonstrated and compared through time history and Response Spectrum analyses of the AIC system in an idealized forced vibration, an idealized free vibration, and earthquake ground motions. The effects of mass, damping, and stiffness of the AS on the response of the PS are investigated in parametric studies. Practical issues such as the sampling interval and time delay on the system performance are also examined. A simple predictive time delay compensation scheme is developed.

In Chapter 3, the NC and MC approaches are proposed for use in MDOF systems. The effectiveness of the OCS, AID, and AVS algorithms in these control approaches are demonstrated through time history and Response Spectrum analyses of a MDOF AIC system in earthquake ground motions. Parameters and practical issues are likewise studied as in Chapter 2.

4.2 Conclusions

Based on the analytical and numerical results obtained in this study, the following conclusions are drawn:

1. Transferring vibrational energy from the PS to the AS through actively controlled interactions between the PS and AS is a viable way of reducing the response of the PS under earthquake ground motion.
2. Theoretically, the OCS algorithm is more efficient than the AID and AVS algorithms in reducing the maximum story drift and maximum absolute acceleration of the PS while minimizing the dynamic impact between the PS and AS.

3. A smaller mass, smaller damping, and larger stiffness in the AS will improve the control efficiency of an AIC algorithm.
4. Practically, the AID and AVS algorithms are more robust than the OCS algorithm with respect to sampling intervals and limit state information, and the AID algorithm is more robust than the OCS and AVS algorithms with respect to time delays.
5. The predictive time delay compensation scheme is very effective in compensating long time delays in the AVS algorithm, but only short time delays in the OCS and AID algorithms.

4.3 Discussion

The OCS, AID, and AVS algorithms are all highly idealized. The OCS algorithm requires that the AS possess much smaller mass, much higher stiffness, and thus a much higher frequency than the PS. In order to measure the rapid motion of the AS and to avoid timing failure, a very small sampling interval is usually needed in the OCS algorithm. This could place severe requirements on data acquisition systems and computer equipment.

The AID and AVS algorithms completely ignore the dynamics of the AS. The resulting dynamic impact between the PS and AS at attachment may seriously damage the IE in the control process. Additionally, in the AID and AVS algorithms, a device with very high damping is needed to absorb most of the vibrational energy in the AS after a detachment from the PS and before a reattachment to the PS. Whether such a device is available remains to be determined.

In all AIC algorithms considered in this study, the attachments between the PS and AS are assumed to be rigid, i.e., the stiffness of the IE is infinite and no damping exists in the IE. As a mechanical device, however, the IE must have finite stiffness and some inherent damping. These factors should be taken into account in further analysis on actuator dynamics.

The MDOF models investigated in this study are idealized shear buildings. However, the bending deformations of the building may become important for tall buildings. Therefore, further refinement to model the dynamic behavior of tall buildings should be made to verify the results obtained from idealized shear building models.

For the shear buildings considered, the primary control objective is to reduce the maximum story drift in the 1st story. In practice, however, in most cases, plastic deformation and damage may first develop in other stories. Hence, versatility should be added in future AIC algorithms and approaches so that appropriate control decisions can be made to reduce the maximum drift in stories where yielding and plastic deformations in the PS are the most severe.

It should be noted that in order to effectively control the vibration of the PS, the maximum control force the AS has to exert on the PS should roughly be of the same magnitude as that exerted by an actuator in a conventional control approach. Such force is usually very large, as shown in Sections 1.3 and 3.2.3. In the case that the force carried by the AS does exceed its elastic limit, Section 2.4.3 has shown that the yielded AS can still provide approximately the same control efficiency as a purely elastic AS does. This feature greatly relaxes the requirement on the stiffness of AS and enhances the applicability of AIC system in practice. Further studies to validate this conclusion on the inelastic behavior of AIC systems are necessary.

Section 3.3.7 showed that in the MC approach the response of the PS can be degraded by the system uncertainties in the mass and stiffness of the AS, especially when the OCS algorithm is employed as the control algorithm. The deterioration of system response due to system uncertainties may be partially compensated by installing more sensors in the building and attaching and detaching the PS and AS at all story levels according to the consensus control decision for several stories instead of according to the control decision from one story.

Observability and controllability of AIC systems are not considered in this exploratory study on active control for civil structures. Theoretically, such analyses can be done

by testing the ranks of the observability matrix and the controllability matrix. It has been shown that, for structural systems with no duplicated modal frequencies, they can be made both observable and controllable by a single properly located sensor and a single properly located controller [Wu, *et al.*, 1979].

Best location of sensors and controllers is an important practical issue for AIC systems. In the MC approach, simulation results of an 8-story shear building have shown that the best location to place the only sensor is on the 1st floor slab of the building. The issue of best locations for multiple sensors still remains to be investigated. It should be noted that for shear buildings most vibrational energy is contained in the lower stories where large story drifts occur. Therefore, similar control effect may be achieved by simply attaching and detaching the AS to the PS in lower stories.

The length of the sampling interval is also a vital issue for AIC systems, especially when the OCS algorithm is employed as the control algorithm. As mentioned before, a proper sampling interval should be small enough to keep the dynamic impact between the PS and AS at attachment within an admissible level. The proper length of the sampling interval is also limited by the reaction time of the data acquisition and actuation systems.

In this study, the length of the time delay is assumed to be constant. Although this is a reasonable assumption for AIC systems, the length of the time delay in a control system typically varies with the dynamic response of the system during the control process. Further, the current predictive scheme compensates for time delays by posteriorly modifying the control decisions initially made in the absence of time delays. For long time delays, this approach can be problematic. To ultimately solve the problem of time delay in an AIC system, approaches should be pursued to embody the time delay and structural uncertainty in the AIC algorithms.

Finally, it is believed that further collaboration between university researchers and industry, together with full-scale experiments, will enhance the potential for AIC to be a cost effective method of achieving improved structural performance in seismic and wind environments.

Appendices

A.1 Active Interface Damping Control Algorithm

In the Active Interface Damping (AID) control configuration, the PS is a regular structure and the AS is a distinct structure either built in or adjacent to the PS. Three types of IEs have been considered. The first type comprises a member that is capable of providing a rigid connection between the two systems when activated. The second type consists of a member that is capable of providing a viscously-damped reaction force between the two systems when activated. The third type includes a member that is capable of providing a Coulomb-damped reaction force between the two systems when activated. It is the first type of IE that is considered in this study. The dynamics of the AS are neglected. In the case for which the AS is a linear elastic element, it is assumed that, upon deactivation, the IE is instantaneously slipped to reduce the reaction force to zero. The state variables measured in AVS control algorithm are the relative velocity and displacement of the PS.

The control objective of AID algorithm is to reduce the resonance buildup in the response of the PS that is produced by an external excitation. The strategy employed to achieve this objective is to remove vibrational energy associated with relative vibration from the PS through interaction with the AS.

Let the velocity and displacement of the PS be sampled in the time domain with a sampling interval, Δt. Then, the AID control algorithms may be described as follows:

- An attachment between the PS and AS will be initiated at time t and maintained for the sampling interval Δt, or maintained from time t to $t+\Delta t$ if the attachment is already in effect, provided the following condition is satisfied

$$E_A(t+\Delta t) < E_D(t+\Delta t).$$

- In all other cases, the PS and AS will be detached.

$E_A(t+\Delta t)$ and $E_D(t+\Delta t)$ are the relative vibrational energy of the PS at the end of the next sampling interval, i.e., at time $t+\Delta t$, for the cases in which the PS and AS are attached and detached respectively. The relative vibrational energy is defined as

$$E(t+\Delta t) = \frac{1}{2} m_1 \dot{x}_1^2(t+\Delta t) + \frac{1}{2} k_1 x_1^2(t+\Delta t).$$

The AID algorithm assures that the relative vibrational energy increase in the PS in each sampling interval be minimum.

A.2 Active Variable Stiffness Control Algorithm

A special subclass of AIC is the Active Variable Stiffness (AVS) control, which was originally proposed by Kajima Corporation. In this control approach, the PS is a regular structure and the AS is a stiff bracing system. The IE is a linking device which may either rigidly attach (lock) or freely detach (unlock) the PS to AS. The dynamics of the AS and IE are neglected. The state variables measured in AVS control algorithm are the relative velocity and displacement of the PS.

The basic idea behind AVS control approach is to produce a non-stationary non-resonant condition by changing the stiffness of the controlled structure according to the measured earthquake input and structural response. The change in stiffness is achieved by means of fast-response IE which, controlled by a computer system, define different configurations for the stiffness matrix of the structure. Attachment of the AS adds a large stiffness and detachment of the AS offers no additional stiffness to the PS.

Let the velocity and displacement of the PS be sampled in the time domain with a sampling interval, Δt. Then, the AVS control algorithms may be described as follows:

- An attachment between the PS and AS will be initiated at time t and maintained for the sampling interval Δt, or maintained from time t to $t+\Delta t$ if the attachment is already in effect, provided

$$\dot{x}_1(t)\,x_1(t) > 0.$$

- In all other cases, the PS and AS will be detached.

The above condition states that the PS and AS be attached (locked) when the deformation of the PS is 'loading' and detached (unlocked) when the PS is 'unloading.' The 'loading' ('unloading') stage is regarded as the duration when the displacement and velocity of the PS are of the same (opposite) sign, i.e., the absolute value of the displacement of the PS is increasing (decreasing).

A.3 Earthquake Ground Motions

The ground motions to which the AIC system is subjected include the El Centro Station North, denoted by ELC, in the 1940 Imperial Valley earthquake and the Rinaldi Station North, denoted by RRS, in the 1994 Northridge earthquake.

The original sampling interval (time steps) of the ELC record was 0.02 second. To meet the sampling interval required by the AIC system studied, the ELC record is linearly interpolated to a sampling interval of 0.004 second. The original RRS record, sampled at every 0.005 second, is adopted in this study.

Figures A.3.1 to A.3.4 plot the acceleration, velocity, and displacement time histories, Fourier Amplitude Spectra, Pseudo-Velocity Response Spectra, and Story Drift Demand Spectra of the ELC and RRS excitations, respectively. Since the strongest shaking occurs during the initial portion in these records, only the first ten second motion is utilized in

the numerical simulations. Table A.3.1 lists the peak values of the acceleration, velocity, and displacement in these two records.

Table A.3.1: Peak acceleration, velocity, and displacement of the ELC and RRS records

Station	Peak Acceleration (cm/s/s)	Peak Velocity (cm/s)	Peak Displacement (cm)
ELC	342	33	11
RRS	805	159	59

The RRS excitation is the so-called near-field earthquake record. Compared to the ELC excitation, RRS excitation exhibits a pulse-like time history, high peak velocity, and a permanent ground displacement. It places much higher demands on the response and story drift of structures than does the ELC excitation. For instance, as shown in Figures A.3.3 and A.3.4, 500 cm/s pseudo-velocity and 6% story drift are observed for the RRS excitation, while the peak pseudo-velocity and story drift are only 120 cm/s and 4% for the ELC excitation. This suggests that the widely used ELC excitation may be inadequate for some design purposes [Iwan, 1994, 1997; Wang *et al.*, 1996]. The RRS record was specially corrected using a newly developed processing scheme [Iwan *et al.*, 1994; Wang, 1996].

A.4 Constructing System Matrices

This section illustrates the construction of system matrices in Equation (3.1.1) through three simple examples. Outlined in Figure A.4.1 (a) is an AIC system consisting of a three-story shear building (PS) and three resilient frames (AS) constructed inside the building. Note that damping matrix, C, can be derived from the mass and stiffness matrices, M and K in Equation (3.1.13) and is therefore omitted here.

In Figure A.4.1 (a), the AS is detached from the PS at all story levels. The DOF of this AIC system is $2N = 2\times3 = 6$. The corresponding mass and stiffness matrices, displacement vector, and location matrix are

$$M = \text{diag}(m_{11}, m_{12}, m_{13}, m_{21}, m_{22}, m_{23}) \tag{A.4.1}$$

$$K = \begin{bmatrix} k_{11}+k_{12}+k_{22} & -k_{12} & 0 & 0 & -k_{22} & 0 \\ -k_{12} & k_{12}+k_{13}+k_{23} & -k_{13} & 0 & 0 & -k_{23} \\ 0 & -k_{13} & k_{13} & 0 & 0 & 0 \\ 0 & 0 & 0 & k_{21} & 0 & 0 \\ -k_{22} & 0 & 0 & 0 & k_{22} & 0 \\ 0 & -k_{23} & 0 & 0 & 0 & k_{23} \end{bmatrix} \tag{A.4.2}$$

$$X = [x_{11}, x_{12}, x_{13}, x_{21}, x_{22}, x_{23}]^T \tag{A.4.3}$$

$$K_a = \Theta_{6\times6}. \tag{A.4.4}$$

In Figure A.4.1 (c), the AS is attached to the PS at all story levels. The DOF of this AIC system reduces to $N = 3$. The corresponding mass and stiffness matrices, the displacement vector, and location matrix are

$$M = \text{diag}(m_{11}+ m_{21}, m_{12}+ m_{22}, m_{13}+ m_{23}) \tag{A.4.5}$$

$$K = \begin{bmatrix} (k_{11}+k_{21})+(k_{12}+k_{22}) & -(k_{12}+k_{22}) & 0 \\ -(k_{12}+k_{22}) & (k_{12}+k_{22})+(k_{13}+k_{23}) & -(k_{13}+k_{23}) \\ 0 & -(k_{13}+k_{23}) & (k_{13}+k_{23}) \end{bmatrix} \tag{A.4.6}$$

$$X = [x_{11}, x_{12}, x_{13}]^T \tag{A.4.7}$$

$$K_a = \begin{bmatrix} k_{21} & -k_{22} & 0 & -k_{21} & k_{22} & 0 \\ 0 & k_{22} & -k_{23} & 0 & -k_{22} & k_{23} \\ 0 & 0 & k_{23} & 0 & 0 & -k_{23} \end{bmatrix}. \tag{A.4.8}$$

The displacements of the AS on the first, second, and third floors are

$$x_{2i}(t) = x_{1,i}(t) + [x_{2i}(t_i) - x_{1i}(t_i)] \quad i = 1, 2, \text{ and } 3. \tag{A.4.9}$$

In Figure A.4.1 (d), the AS is attached to the PS at the first and third story levels. The DOF of this AIC system is $2N\text{-}M = 2\times3\text{-}2 = 4$. The corresponding mass and stiffness matrices, and displacement vector, and control force are

$$\text{M} = \text{diag}(m_{11}+ m_{21}, m_{12}, m_{13}+ m_{23}, m_{22}), \tag{A.4.10}$$

$$K=\begin{bmatrix} (k_{11}+k_{21})+k_{12}+k_{22} & -k_{12} & 0 & -k_{22} \\ -k_{12} & k_{12}+(k_{11}+k_{23}) & -(k_{13}+k_{23}) & 0 \\ 0 & -(k_{13}+k_{23}) & (k_{13}+k_{23}) & 0 \\ -k_{22} & 0 & 0 & k_{22} \end{bmatrix} \tag{A.4.11}$$

$$X=[x_{11},x_{12},x_{13},x_{22}]^T \tag{A.4.12}$$

$$K_a=\begin{bmatrix} K_{21} & 0 & 0 & -K_{21} & 0 & 0 \\ 0 & 0 & -K_{23} & 0 & 0 & K_{23} \\ 0 & 0 & K_{23} & 0 & 0 & -K_{23} \\ 0 & 0 & 0 & 0 & 0 & 0 \end{bmatrix}. \tag{A.4.13}$$

The displacements of the AS on the first and third floors are

$$x_{2i}(t)=x_{1,i}(t)+[x_{2i}(t_i)-x_{1i}(t_i)], \quad i=1 \text{ and } 3. \tag{A.4.14}$$

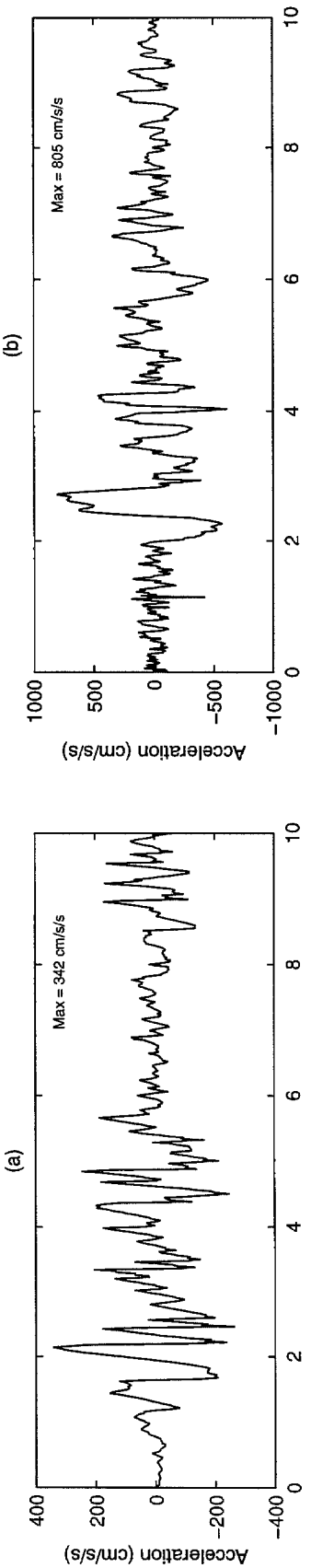

Figure A.3.1: Acceleration, velocity, and displacement time histories of the ELC excitation

Figure A.3.2: Acceleration, velocity, and displacement time histories of the RRS excitation

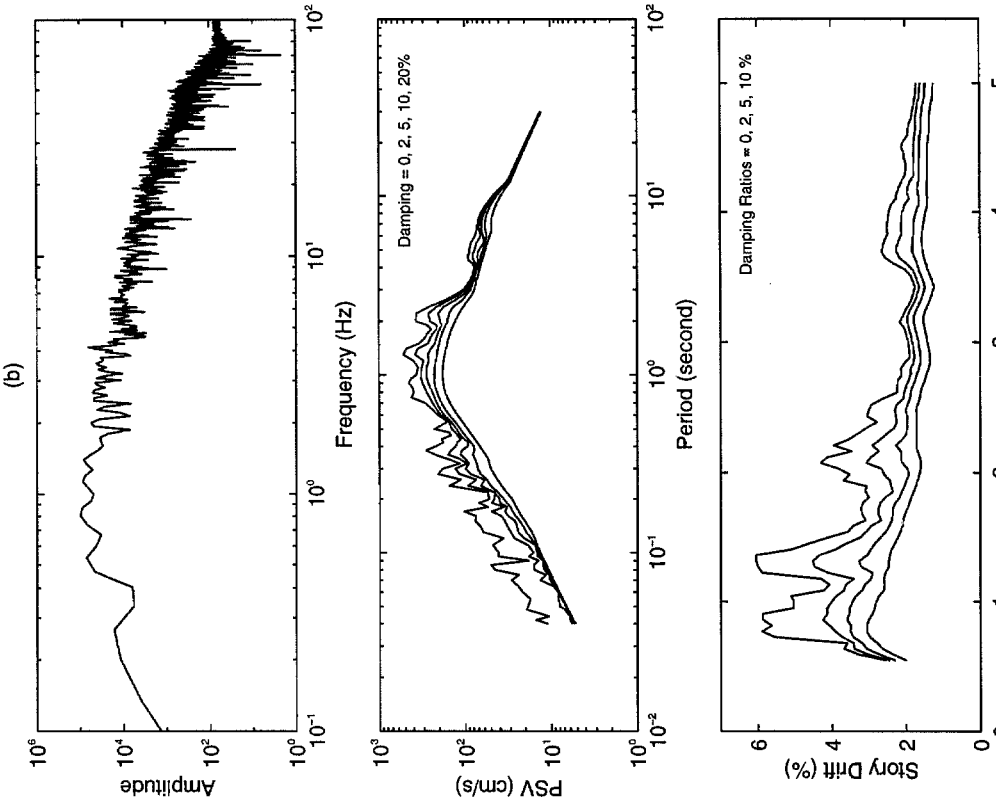

Figure A.3.4: Fourier Amplitude Spectra, Pseudo-Velocity Response Spectra, and Drift Demand Spectra of the RRS excitation

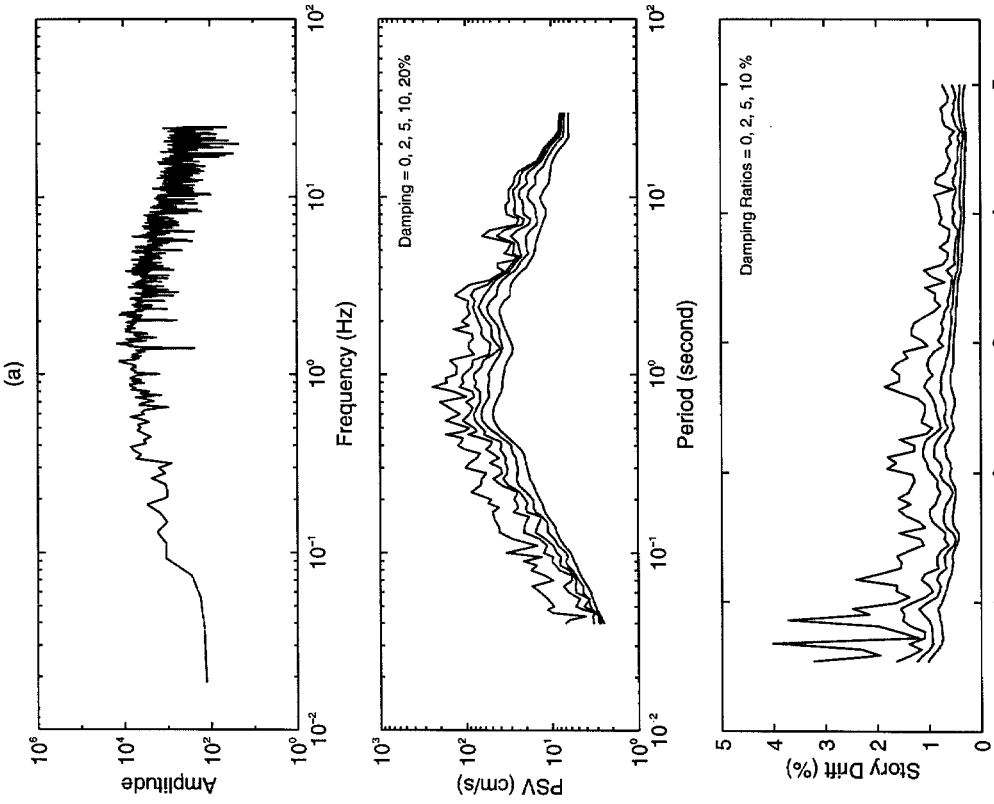

Figure A.3.3: Fourier Amplitude Spectra, Pseudo-Velocity Response Spectra, and Drift Demand Spectra of the ELC excitation

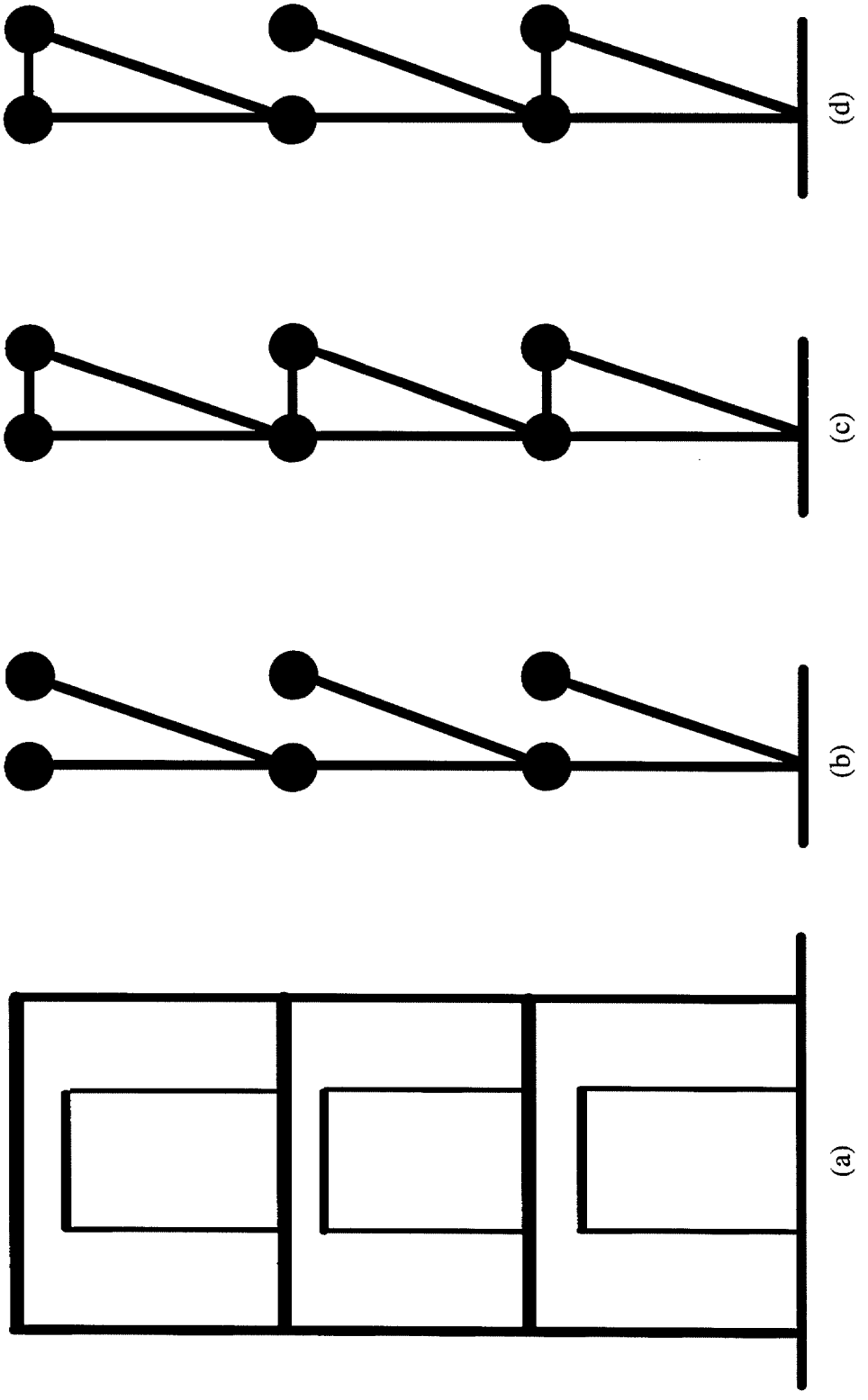

Figure A.4.1: (a) Configuration of the three-story shear building (b) simplified models for the three-story shear buildings corresponding to the PS and AS (b) detached at all stories (c) attached at all stories and (d) attached at the first and third stories

References

Hayen, J.C. and W.D. Iwan, 1994, "Response control of structural systems using active interface damping," *Proceedings of the First World Conference on Structural Control*, Volume 1, Los Angeles, 1994.

Hayen, J.C., 1995, "Response control of structural systems using semi-actively controlled interactions," *Ph.D. Thesis*, EERL 95-03, California Institute of Technology, Pasadena, 1995.

Housner, G.W., 1956, "Limit design of structures to resist earthquakes," *Proceedings of the First World Conference on Earthquake Engineering*, pp. 5:1-11, Berkeley, 1956.

Housner, G.W., T.T. Soong, and S.F. Masri, 1994, "Second generation of active structural control in civil engineering," *Proceedings of the First World Conference on Structural Control*, Volume 1, Los Angeles, 1994.

International Conference of Building Officials (ICBO), 1994, *Uniform Building Code*, Whittier, California, 1994.

Iwan, W.D. and X.D. Chen, 1994, "Important Near-Field ground motion data from the Landers earthquake," *Proceedings of the 10th European Conference on Earthquake Engineering*, Vienna, Austria, 1994.

Iwan, W.D., 1994, "Near-Field considerations in specification of seismic design motions for structures," *Proceedings of the 10th European Conference on Earthquake Engineering*, Vienna, Austria, 1994.

Iwan, W.D. and L.J. Wang, 1996, "New developments in Active Interaction Control," *Proceedings of the Second International Workshop on Structural Control*, Hong Kong, China, December, 1996.

Iwan, W.D., 1997, "The Drift Spectrum: a measure of demand for earthquake ground motion," *Journal of Structural Engineering*, Volume 123, No. 4, April, 1997.

Kobori, T. and S. Kamagata, 1992, "Dynamic intelligent buildings - active seismic response control," *Intelligent Structures - 2*, edited by Y. K. Wen, Elsevier Science Ltd., London, 1992.

Kobori, T., M. Takahashi, T. Nasu, and N. Niwa, 1993, "Seismic response controlled structure with active variable stiffness system," *Earthquake Engineering and Structural Dynamics*, Volume 22, pp. 925-941, 1993.

Wang, L.J., 1996, "Processing of Near-Field earthquake accelerograms," *EERL 96-04*, Earthquake Engineering Research Laboratory, California Institute of Technology, September, 1996.

Wang, L.J., Q. Gu, and W.D. Iwan, 1996, "A collection of processed Near-Field earthquake accelerograms with Response and Drift spectra," *EERL 96-05*, Earthquake Engineering Research Laboratory, California Institute of Technology, November, 1996.

Wu, Y.W., R.B. Rice, and J.N. Juang, 1979, "Sensor and actuator placement for large flexible space structures," *Preprint Joint Automatic Control Conference*, 1979.

Yamada, K. and T. Kobori, 1995, "Control Algorithm for estimating future responses of active variable stiffness structure," *Earthquake Engineering and Structural Dynamics*, Volume 24, No. 8, pp. 1085-1100, 1995.